2020-08-04

Analysis of Inlet Distortion Patterns on Distortion Transfer and Generation Through a Highly Loaded Fan Stage

Andrew Dallin Orme
Brigham Young University

BYU ScholarsArchive Citation

Orme, Andrew Dallin, "Analysis of Inlet Distortion Patterns on Distortion Transfer and Generation Through a Highly Loaded Fan Stage" (2020). *Theses and Dissertations*. 8649.
https://scholarsarchive.byu.edu/etd/8649

Analysis of Inlet Distortion Patterns on Distortion Transfer and Generation Through a Highly Loaded Fan Stage

Andrew Dallin Orme

A thesis submitted to the faculty of
Brigham Young University
in partial fulfillment of the requirements for the degree of

Master of Science

Steven E. Gorrell, Chair
Julie Crockett
Scott L. Thomson

Department of Mechanical Engineering

Brigham Young University

ABSTRACT

Analysis of Inlet Distortion Patterns on Distortion Transfer and Generation Through a Highly Loaded Fan Stage

Andrew Dallin Orme
Department of Mechanical Engineering, BYU
Master of Science

Characterization of distortion transfer and generation through fans with distorted inlet conditions enables progress towards designs with improved distortion tolerance. The abruptness of transition from undistorted to distorted total pressure regions at the inlet impacts the induced swirl profile and therefore the distortion transfer and generation. These impacts are characterized using URANS simulations of PBS Rotor 4 geometry under a variety of inlet distortion profiles. A 90° and a 135° sector, both of 15% total pressure distortion, are considered. Variants of each sector size, with decreasing levels of distortion transition abruptness, are each applied to the fan. Fourier-based distortion descriptors are used to quantify levels of distortion transfer and generation at axial locations through the fan, principally at the stator inlet. It is shown that a gradual transition in distortion at the inlet results in decreased levels of distortion transfer and generation. The flow physics resulting in this reduction are explored.

URANS simulations involving turbomachinery are complex and often require simplifying assumptions to balance computational costs with accuracy. One assumption removes the need for a nozzle to control nozzle operation condition and replaces it with a static pressure boundary condition located at the stator exit. This assumption is challenged by conducting a series of distorted inlet simulations with a nozzle, which are then compared to a corresponding set of simulations conducted using the exit boundary assumption. Performance parameters for each set of simulations are compared. Performance was observed to be within 1% difference between the two methods, supporting the assumption that a static pressure boundary is adequate for controlling inlet distortion simulations.

Finally, full annulus URANS simulations are presented to investigate distortion phase shift in a single stage transonic fan. The fan is subject to a 90° sector inlet total pressure distortion. Simulation results are presented for choke, design, and near-stall operating conditions. Circumferential profiles of swirl, total pressure, total temperature, power, and phase shift are analyzed at 10%, 30%, 50%, 70%, and 90% span. Several metrics for phase shift, which is a measure of the rotational translation of a distortion profile, are presented and compared. Each aims to assist understanding the translational motion of distortion as it passes through the fan. The different metrics used for phase shift are used to analyze distortion phase. Insights from each are presented alongside limitations for each method. A combination of methods is proposed to address their respective limitations.

Keywords: distortion, URANS, nozzle, phase shift, swirl

ACKNOWLEDGMENTS

This thesis would not have been possible without the valuable contributions of a multitude of people.

Dr. Stephen Gorrell served as my graduate advisor and mentor during my time at BYU. His patient guidance, encouragement, and perspective helped me deal with the challenges of a graduate degree. I'm grateful he selected me for his senior design project, which eventually led to me joining the BYU Turbomachinery Research Lab (TRL) as a Master's student.

Alexander Newell was a fellow research assistant in the BYU TRL and my friend throughout the challenges of thesis and coursework. His excitement about learning and commitment to exploration helped me stay motivated when classes and research got hard. I'm grateful for his constant friendship through my time at BYU.

Addison Pulsipher assisted me as an undergraduate assistant during my final year as a Master's student and performed several valuable studies which assisted in the methodology of this thesis. I'm grateful for his patience as we worked together!

Mr. Rory Howard, a supervisor at Hill Air Force Base (AFB), and the Department of Defense SMART Scholarship program made my master's degree possible by making me a SMART Scholar, which provided me funding to cover expenses as a Master's Student. I'm grateful for Mr. Howard's willingness to accept my application and offer me a spot with his team at Hill AFB.

My parents, Cathy and Kenyon Orme, have always encouraged me to go above and beyond. Their moral and emotional support during my graduate degree were invaluable!

The BYU Office of Research Computing (ORC) provided invaluable computational resources which made this work possible. Brennon Brimhall, Levi Morisson, and the rest of the ORC staff were instrumental in keeping our simulations running smoothly when we hit problems.

TABLE OF CONTENTS

LIST OF TABLES

LIST OF FIGURES

NOMENCLATURE

A	Area
AIP	Aerodynamic Interface Plane
c_p	Specific Heat
∇	Gradient Operator
$\frac{\Delta PC}{P}$	Distortion Intensity
$\vec{g}$	Gravity
h	Height
k	Thermal Conductivity
μ	Viscosity
p	Pressure
PD	Percent Distortion
P_t	Total Pressure
$\dot{q}$	Energy Generation
ρ	Density
RI	Rotor Inlet
s	Summation of Fourier Series
SI	Stator Inlet
SO	Stator Outlet
t	Time
θ_i^-	Distortion Extent
T	Temperature
TDC	Top Dead Center
T_t	Total Temperature
U	Blade Speed
$\vec{V}$	Velocity
$\dot{W}$	Power

CHAPTER 1. INTRODUCTION

Jet engines are a marvel of modern engineering. They have changed the way we travel and do business by increasing the speed and efficiency at which we are able to travel. These amazing systems would not be possible without conscious design decisions which seek to progress towards ever improving efficiency and performance. Such advances often come after lengthy studies into areas where designers have identified potential improvement in performance waiting to be discovered. One such area, which has become an established field of research, explores the impacts of inlet distortion on turbomachinery.

Inlet distortion refers to a condition where the airflow entering a jet engine is not uniform. The flow may contain circumferential or radial variations in flow parameters such as pressure, temperature, swirl, or velocity. A sample inlet profile with a total pressure distortion is shown in Figure 1.1. Distortions in the inlet flow field can be caused in a variety of ways. One potential source of distortion occurs in high performance engines, such as those in modern fighter aircraft, which are subjected to extreme flight maneuvers. These maneuvers result in flow separation at the engine inlet which cause pressure distortion at the engine inlet.

Another source of distortion comes from the integrated design approach used in many fighter aircraft, where the engine is embedded deep in the fuselage of the aircraft. In this case, the air to the engine must pass through the inlet duct, which often has aggressive curves. As the flow passes through the inlet duct, pressure and swirl distortions often develop. A third source of flow distortion is wake or exhaust ingestion. Actions such as firing a weapon, following in close formation flight, or performing vertical take off and landing (VTOL) maneuvers can result in temperature and pressure distortions at the engine inlet.

Inlet distortion is known to adversely impact engine performance, often by decreasing the engine pressure ratio, efficiency, or stall margin. All of these impacts are undesirable. In an effort to improve engine designs by making them more tolerant to distortion, the impacts of inlet distortion

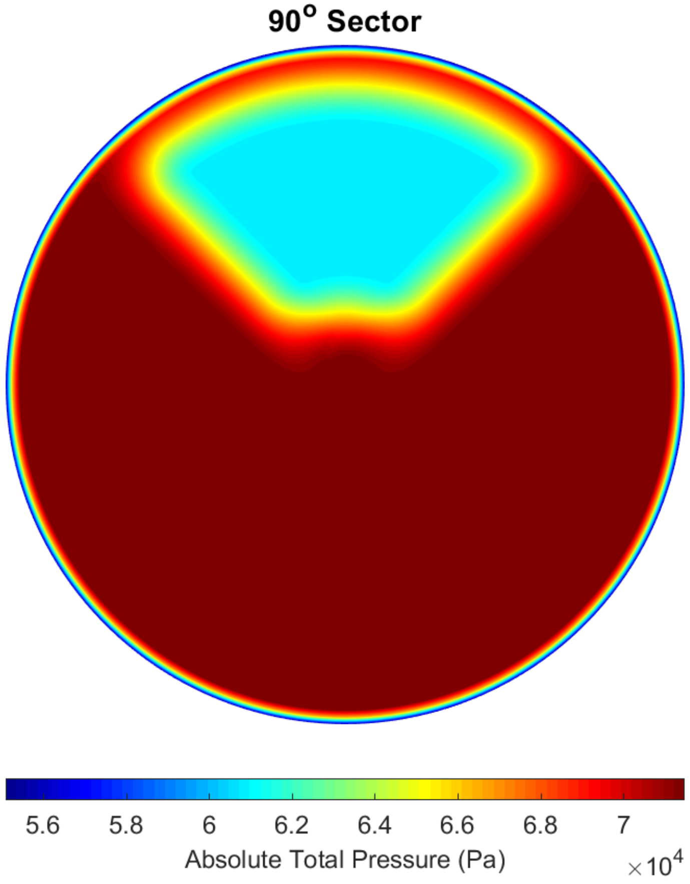

Figure 1.1: Sample inlet distortion profile. The distorted region is indicated in light blue, where the total pressure is less than the rest of the profile.

on engine performance are being closely studied, along with the interactions of distorted flow with turbomachinery geometry. Distortion impacts tend to be strongest on the fan and compressor stages of an engine and are the focus of a large part of the research community. The goal is to improve understanding about the ways inlet distortion interacts with the engine so that these interactions can be accounted for in future designs. This enables more accurate predictions of engine performance.

Several methods exist for investigating inlet distortion impacts on turbomachinery performance. The first is to conduct physical experiments with the turbomachinery subjected to various levels of distortion. Such experiments can provide high accuracy data regarding performance losses because they use real geometry in real flow conditions, provided instrumentation is sufficient. However, experimental setups are expensive to operate and are limited in the distortions that can be generated. They also tend to only provide insights into large scale impacts due to limitations in the number of feasible measurement locations. To address these limitations, computational simulations have started to play a larger role in inlet distortion research.

The impacts of distortion on turbomachinery can be simulated computationally using Unsteady Reynolds Averaged Navier-Stokes (URANS) solvers. These simulations solve for the flow fields with high accuracy, while allowing for near infinite variations in distortion conditions. Results can be obtained with greater resolution at any point in the simulation domain, enabling the investigation of smaller scale impacts on flow. Far from perfect, the major downside to URANS simulations are their computational costs. In most cases, such simulations require use of supercomputing clusters to complete a solution in a reasonable time-frame.

In order to balance computational expenses with simulation fidelity, simplifications are often made during the creation of simulated geometry. Such simplifications can include the use of single passage simulations, where only a single blade passage of the geometry is modeled and flow is solved using periodic boundary conditions to simulate the full geometry. Another common method is to simplify inlet and outlet geometry. Experimental test apparatus often include complex inlet and outlet geometries which are excluded in simulations in favor of basic boundary conditions. The exclusion of these experimental geometries leads to concerns that simulated results may not generalize to physical geometries.

Recent studies have investigated the impacts of distortion on a high performance fan referred to as the Parametric Blade Study (PBS) Rotor 4 [3, 11]. The geometry of Rotor 4 is shown in Figure 1.2. Rotor 4 shares many of the same design characteristics with fans found in advanced jet engines. These studies identified impacts on fan performance due to inlet distortion and how the impacts changed with fan operating condition. The distortion simulated in these works was a 90° distortion sector which is representative of distortion observed in an s-duct diffuser. A major finding from these studies was an observation that the transition region between distorted and undistorted flow played a large role in the distortion behavior and proposed that it be studied in closer detail. To better generalize the impacts of distortion on Rotor 4, additional inlet distortions should be simulated.

The purpose of this thesis is to expand the understanding of the impacts of inlet distortion on fan performance and to further verify the simulation methodology. This is accomplished by completing the following:

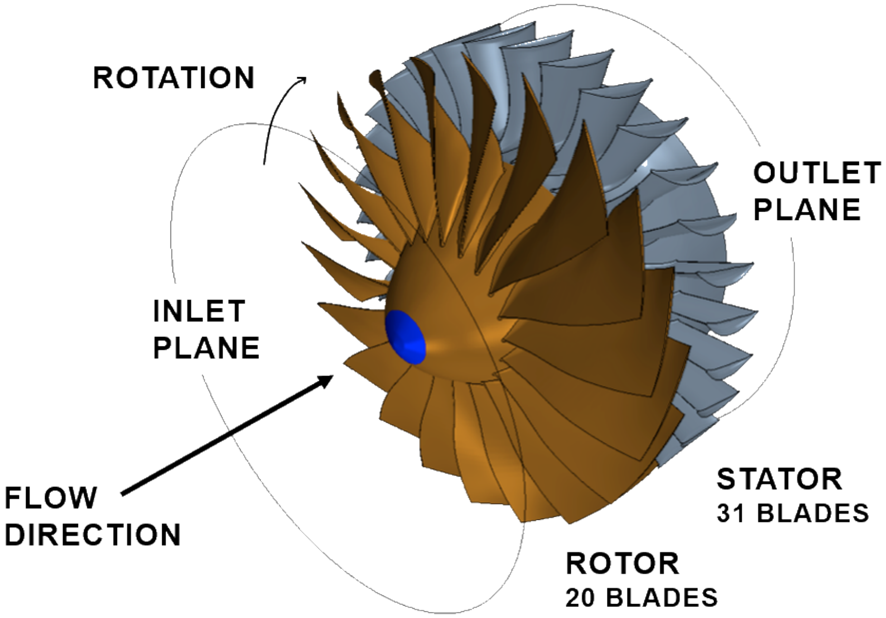

Figure 1.2: Rotor 4 geometry.

- Present and analyze results from distorted Full-Annulus URANS simulations of Rotor 4 under a series of inlet conditions with gradual variations in distortion shape. Variations will consist of alterations to the spatial transition gradient between clean and distorted regions of an inlet profile. The impacts these distortion shape changes have on fan performance will be explored.

- Investigate changes in simulation results with the addition of nozzle geometry, used in place of the conventional exit boundary condition. Simulations for Rotor 4 under distortion will be conducted for a variety of operating conditions using a nozzle. Results from these simulations will be compared to those presented by Soderquist [3], who used a conventional exit condition. The comparisons will be used to propose whether exit condition or nozzle geometry should be used in future simulations.

- Further explore methods used to describe distortion by performing an investigation comparing several descriptors which quantify circumferential migration of distortion effects in Rotor 4, referred to as phase shift. Fourier series based descriptors will be defined and compared with a simplified phase shift descriptor. The benefits and limitations of each parameter will be explored and any insights into phase shift behavior identified.

This thesis will proceed by presenting background information useful for understanding the three above objectives. The methodology for accomplishing each objective will then be outlined. Results for each topic will then be presented and findings will be highlighted. The thesis will then conclude with a review of key results and discussions, as well as proposing future work.

CHAPTER 2. BACKGROUND

Useful background information relevant to the objectives of this thesis will be presented in this chapter. This includes a brief review of sources of inlet distortion, impacts of distortion, experimental methods, computational methods, and description of distortion.

2.1 Sources of Inlet Distortion

Throughout the design process for a turbomachinery component, incoming airflow is assumed to be ideally uniform. This simplification streamlines the design process because it makes analytical analysis and computational simulations easier and faster, which improves the ability to iterate through and evaluate multiple designs. In such undistorted flow conditions, basic turbomachinery performance is fairly well understood and can be readily characterized.

Engineering principles teach us that ideal conditions are often unrealistic representations of real-world conditions. Reality is difficult to precisely account for in a design, resulting in the use of design margins and assumptions. For early jet engines, such margins and assumptions were adequate to account for the real-world conditions the engine operated in. This was primarily due to the simple nature of the engines and their uses.

As jet engines spread in application to a larger variety of systems, unaccounted for losses in performance were observed, which suggested that the ideal uniform inlet condition assumption was no longer adequately representing the operating conditions of some jet engines. In the 1960s, designers started to recognize that variations in total pressure conditions at the inlet of an engine had impacts on performance. Total temperature and swirl distortions were recognized as an issue as engines found their way into new applications. Cousins et al provide an excellent review of early inlet distortion studies in their 2004 work [2]. The realistic operation of modern turbomachinery often includes irregularities in the inlet flow.

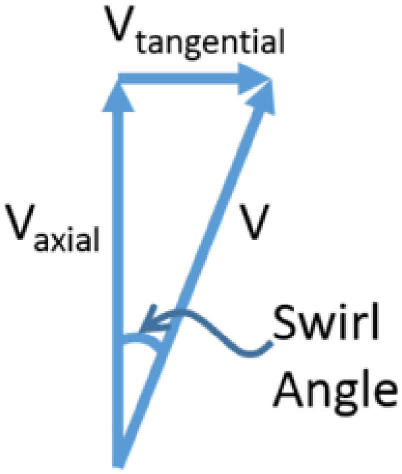

Figure 2.1: Definition of swirl angle.

Inlet distortion is primarily composed of variations in three flow parameters; total pressure (P_t), total temperature (T_t), and swirl. P_t and T_t are measures of total pressure and total temperature respectively that include a measure of fluid velocity. Swirl is a measure of tangential flow angle and helps quantify rotational motion within a flow. This is illustrated in Figure 2.1 which shows that swirl is defined as the angle between the primary flow vector and the axial flow component.

In a uniform, or undistorted inlet condition, each of these parameters is a constant value at all points at the inlet of the geometry. Any variations in these values is referred to as a distortion and results in a distorted inlet condition. A sample of a uniform and distorted inlet condition for P_t is shown in Figure 2.2. A distortion of this type would likely be generated by a duct, such as the one seen in Figure 2.3. It should be noted that these profiles both include a boundary layer at the outer radius, indicated by the ring of lower pressure. For the purposes of this research, the boundary layer is not considered as inlet distortion.

Variations in inlet flow can be caused in a wide variety of ways. Only a few sources will be briefly presented here. While not essential to understanding the work of this thesis, knowing a few of the sources can help develop a more complete picture of inlet distortion. The first source, which can primarily cause T_t distortions, is ingestion of exhaust from weapons, wakes from leading aircraft, or during vertical take off and landing operations (like those performed by the F-35B). As a weapon is fired from close to the aircraft, the hot exhaust from its propulsion source can be sucked into the engine, resulting in a region of higher relative temperature. Following closely to an-

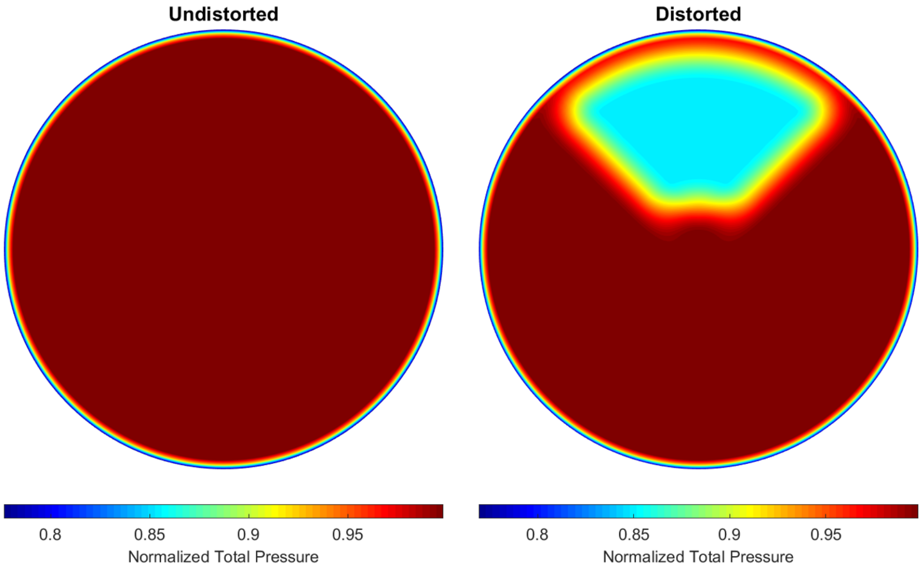

Figure 2.2: Sample inlet profiles with boundary layers. Left profile is undistorted, right profile has a 15% distortion sector.

other aircraft or ingesting engine exhaust reflected from the ground can cause similar temperature distortions.

An additional source of distortion comes from embedded engine integration, which requires the use of ducts to direct incoming flow to the engine [7]. As air-frames become smaller and seek for low profiles, embedded engines have become more common. A sample configuration showing an embedded engine with s-duct inlet diffuser is shown in Figure 2.3. As flow moves through an inlet duct to the embedded engine, changes in area or shape can result in P_t distortions at the engine inlet. The sharp bends in the duct can cause adverse pressure gradients which in turn can cause boundary layer separation. The separated regions will have lower total pressures relative to the rest of the flow, and will propagate downstream as distortions. An illustration of the development of pressure distortion is provided in Figure 2.4. This figure shows the development of a pressure distortion located at the bottom of a duct.

Distortion may also be generated from upstream geometry, such as support struts or inlet vanes. Required for structure or to control flow, these can introduce swirl or pressure distortions on the flow before it reaches the engine. A final source of distortion can come from extreme flight maneuvers, which can cause flow separation in the diffuser upstream of an engine. Such maneuvers

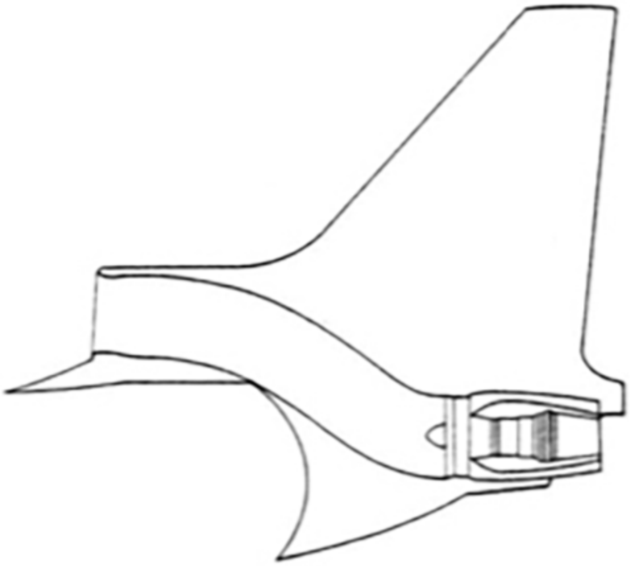

Figure 2.3: Embedded engine with s-duct inlet diffuser. This configuration is from the Lockheed Martin L-1011 aircraft [1].

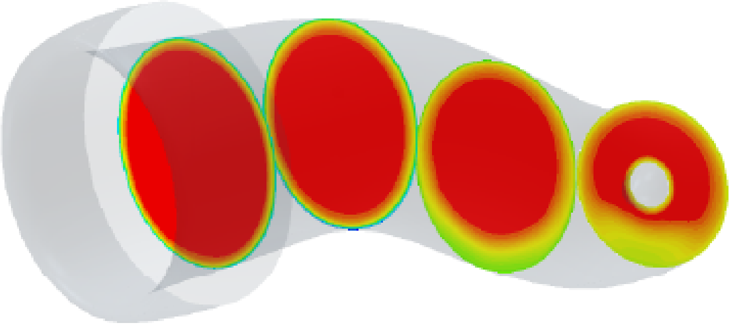

Figure 2.4: Representation of inlet duct distortion source. Flow moves from left to right, with a region of low pressure forming at the bottom of the duct as it reaches the engine.

include high angle of attack take-off or high-G turns. The resulting flow separation can result in a low pressure region and swirl. Figure 2.5 shows an illustration of flow separation due to a high angle-of-attack.

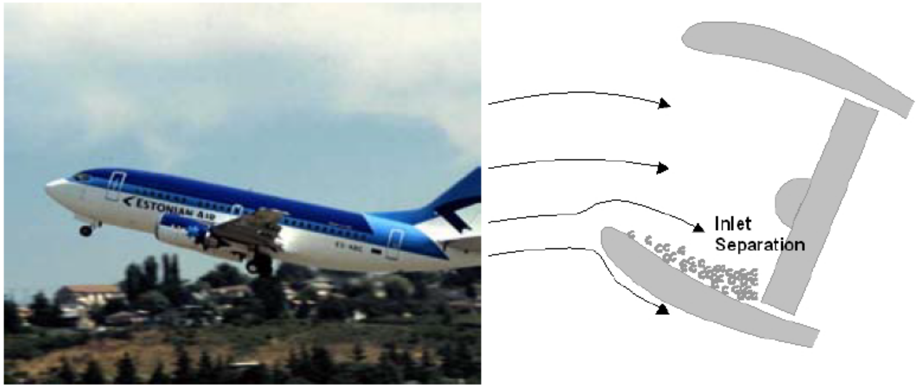

Figure 2.5: Illustration of flow separation due to high angle-of-attack take-off maneuver, which would result in a distorted inlet flow [2].

2.2 Impacts of Inlet Distortion

In any of its forms, inlet distortion has been observed to have a negative impact on turbomachinery. This section will explore some of these impacts to add context to the importance of inlet distortion research.

As with many engineered systems, engine efficiency is an important parameter used to quantify performance. The mass flow where peak efficiency occurs is referred to as the design operating point and is where it is designed to operate for the majority of the time. Inlet distortion decreases the overall efficiency of the turbomachinery at all points in its operation and shifts the peak efficiency to a higher mass flow. Figure 2.6 shows the efficiency of Rotor 4 under clean inlet conditions recorded experimentally and the efficiency of Rotor 4 under simulated distorted inlet conditions. The distorted condition results in lower overall efficiencies throughout its operating mass flows compared to the clean condition. The peak efficiency is also observed to shift to a higher mass flow rate.

Figure 2.7 shows typical operating curves for a high performance fan. At high mass flows, the fan reaches a state referred to as choke, where pressure ratio rapidly drops as mass flow reaches a maximum value. Choke corresponds to sharp decreases in efficiency. At the other end of the operating spectrum, the fan enters a state called stall. At stall, pressure ratio levels off and the fan is unable to perform additional work on the flow. Stall is dangerous for turbomachinery because it can cause sudden losses in pressure across key engine components, causing the system to stop

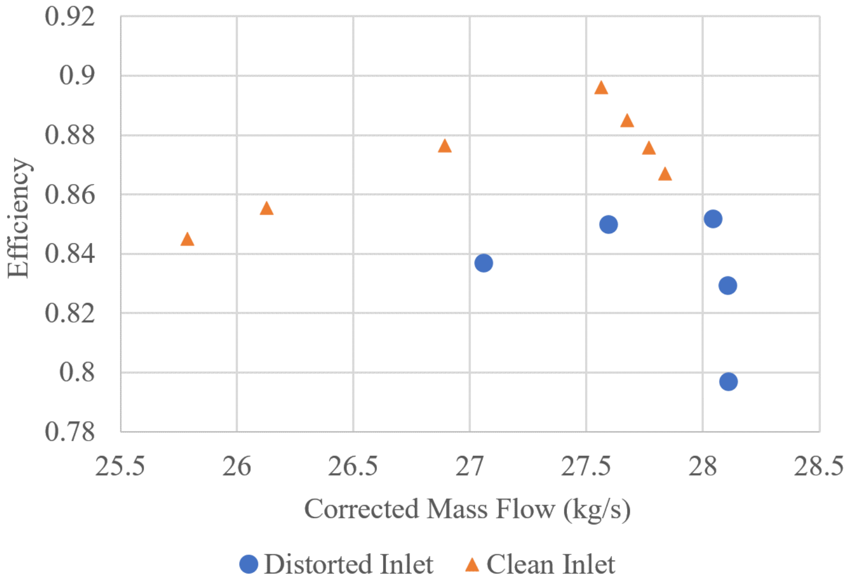

Figure 2.6: Efficiency curves for Rotor 4 under distorted (simulations) and clean inlet conditions (experimental). Distorted efficiency data is from [3] and clean data is from [4]. Stall occurs at the far left (low mass flow) and choke occurs at the far right (high mass flow).

functioning properly. This phenomena is referred to as engine surge. To avoid surge, a stall margin is specified which serves as a buffer between normal operating ranges and surge. Under distortion, stall has been observed to occur at higher mass flow rates, which effectively decreases the stall margin. This could result in the unanticipated formation of stall cells and result in surge outside of the design stall margin, resulting in surge at higher mass flow rates. The works referenced here each investigated quantifying stall under various inlet distortions [12, 13]. A good review of stall and surge can be found in the work by Day [14].

Inlet distortions often contain non-uniform circumferential and radial distributions of distortion, such as the one in Figure 2.2. That is, distortion can be concentrated around circumferential spans and radii, rather than being distributed evenly. This directly results in rotor blades experiencing different flow conditions as they rotate through the clean and distorted regions. As blades enter and exit distorted flow, they can be subjected to rapid changes in blade loading due to variations in pressures, flow angles, and mass flow. Over time, this can cause premature blade failure, due to the cyclic nature of the loading changes.

These large scale impacts in performance are often linked to changes in the flow physics within the rotor itself. Two of these flow physics phenomena will be outlined here and they are

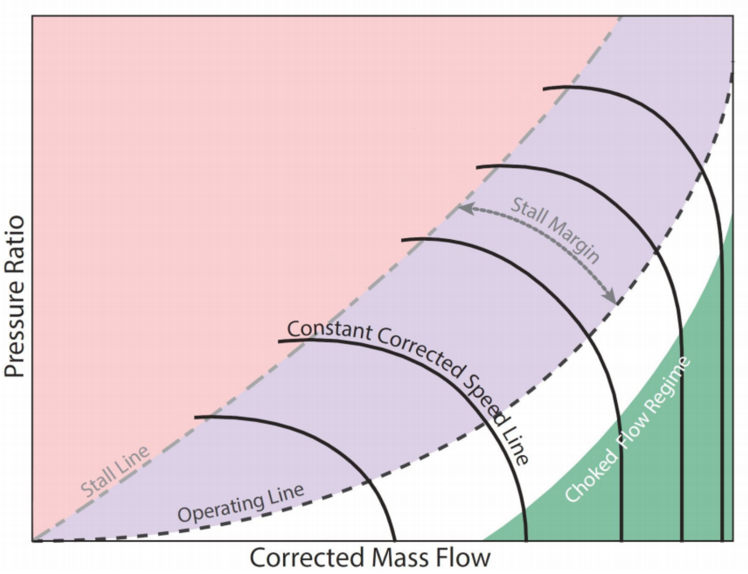

Figure 2.7: Illustration of engine speed lines and stall margins.

further investigated in this thesis. The phenomena that will be reviewed are generation of additional distortion and changes in blade shock waves.

If a single type of distortion, such as P_t, is applied to a system, other forms of distortion will be naturally induced in the flow as a result [10, 11, 15–17]. One common combination which plays a large role in the results of this thesis is referred to as pressure induced swirl. This occurs when a P_t gradient is applied as inlet distortion. As the flow field adjusts to the distortion upstream of the rotor geometry, regions of swirl are generated. These regions of swirl alter flow angles and cause variations in blade performance.

In some cases, P_t distortions can also result in the induction of T_t distortion. These temperature variations impact rotor efficiency. The combined impacts of induced distortions and pressure distortions can cause additional impacts to the system than would be observed with an isolated distortion type.

Weston et al observed swirl formation as a result of P_t distortion and gave a brief explanation of the underlying flow physics as illustrated in Figure 2.8 [10]. A static pressure gradient forms as a result of the applied P_t distortion at the inlet. This creates a force imbalance on the fluid, causing bulk fluid motion in both circumferential and radial directions. This bulk movement causes the induction of swirl distortion.

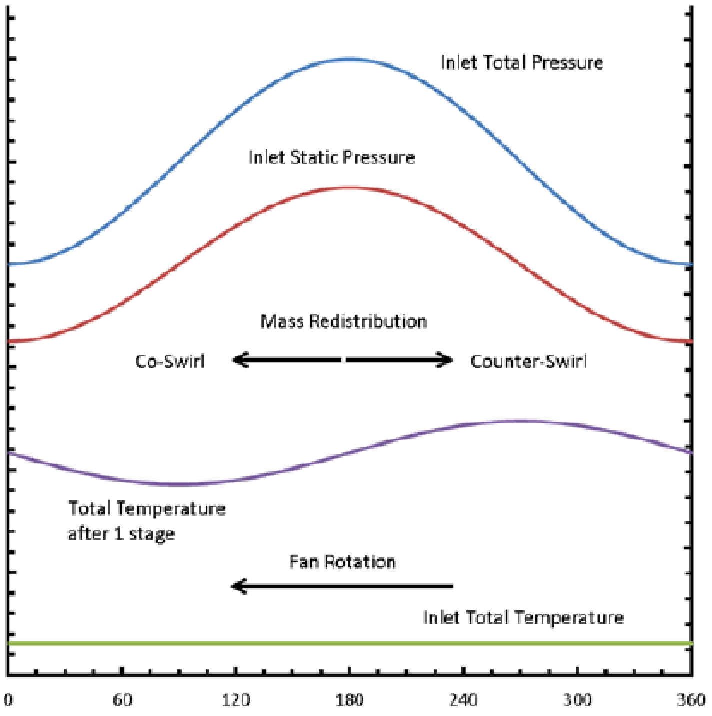

Figure 2.8: Development of Swirl from Inlet Total Pressure Distortion.

Swirl distortions alter the flow angle at the leading edge of the rotor. This is referred to as incidence angle. It is similar in concept to angle of attack for an aircraft. At the nominal incidence the relative velocities around a rotor blade should look something like Figure 2.9a which plots relative surface velocity V_s to free stream velocity V_{fs}. On the suction surface, flow accelerates until a peak, after which it decelerates. The pressure surface flow slows before reaching a minimum, and then accelerates. The accelerated flow over the suction surface results in decreased pressure while the slowed flow on the pressure surface results in increased pressure. The net force between these pressures is the work done on the blade by the flow, and is referred to as blade loading. When flow incidence is increased, the pressure differences between the pressure and suction surfaces of the blade are made larger, due to increased velocity on the suction surface and decreased velocity on the pressure surface. This results in increased levels of blade loading. Alternatively, when blade incidence is lowered, velocity is decreased on the suction surface and increased on the pressure surface. This results in a decrease in blade loading. The variations in surface velocities are shown

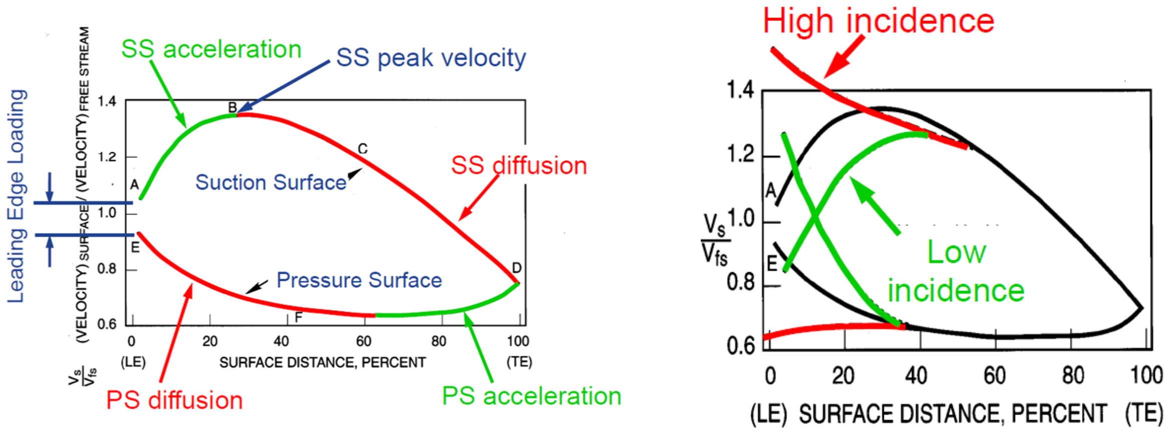

(a) Nominal incidence.

(b) High and low incidence.

Figure 2.9: Surface velocities for a rotor blade with varying incidence [5]

in Figure 2.9b. Variations in blade loading caused by incidence can result in the generation of T_t distortions as a result of the changes in work performed by the blades.

In addition to induction, new distortions can be generated as applied distortion passes through geometry. Generated or induced distortion can cause additional impacts on performance when combined with applied distortion. This thesis uses the following convention to differentiate between applied distortion and generated distortion. We refer to measures of how an applied distortion moves and interacts with geometry as distortion transfer and refer to how induced or generated distortion changes as distortion generation. In the case of pressure induced swirl, changes in pressure distortions through a rotor would be described using as distortion transfer. Induction and changes in properties such as swirl or T_t would be described using as distortion generation.

Work by Soderquist in 2018 and 2019 explored inlet distortion transfer and generation for Rotor 4 under various operating conditions [3, 11]. While exploring radial variations in distortion transfer and generation from choke to near-stall operating conditions, it was observed that the circumferential locations of the maximum and minimum induced swirl corresponded to the circumferential locations of the edges of the inlet distortion. In essence, the induced swirl is largest where the P_t distortion transitions from clean to distorted.

This is illustrated in Figure 2.10 which was obtained from simulating a distorted inlet flow through the rotor 4 geometry. Soderquist utilized the distortion pattern shown in Figure 1.1, which is represented as traverses at several blade spans in Figure 2.10a. The edges of this distortion occur

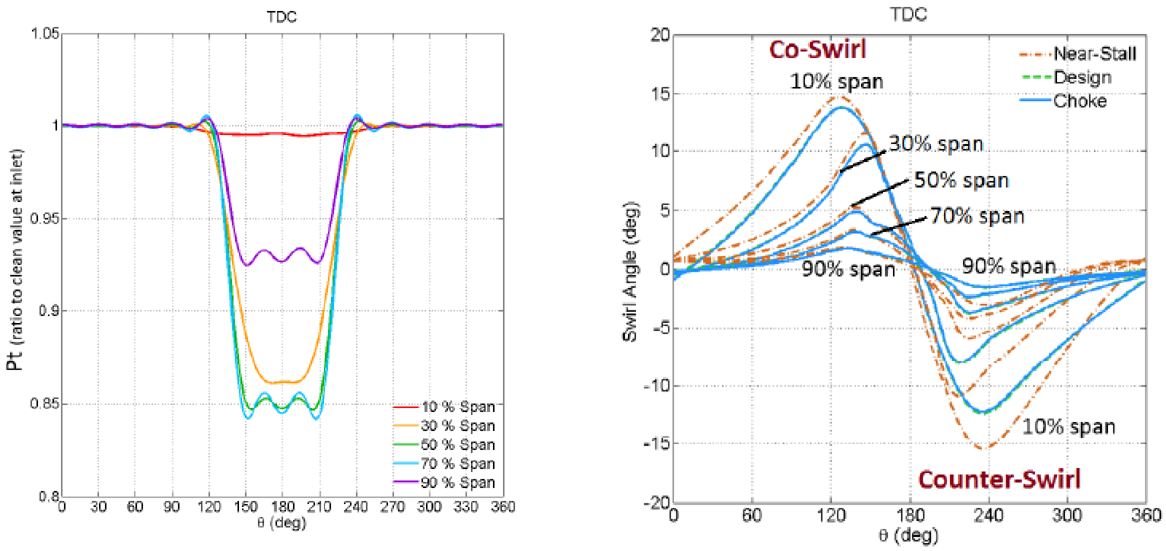

(a) Fourier-reconstructed traverses of P_t at rotor inlet.
(b) Induced swirl traverses at the rotor inlet.

Figure 2.10: Illustration of the connection between maxima of induced swirl to edges of P_t distortion from [3].

at approximately 135° and 225°. The induced swirl is shown in Figure 2.10b, with the maximum labeled as co-swirl and the minimum labeled as counter-swirl. Co-swirl occurs around 135° and counter-swirl occurs around 225°, with some spanwise variation. These circumferential locations which correspond to the edge of the distortion pattern were additionally observed to coincide with the maximum and minimum magnitudes of P_t, T_t, and blade power profiles after passing through the rotor. It was concluded that the abruptness or smoothness of the transition from undistorted to distorted flow in a sector was important and affects the amount of induced swirl, power variation, and generated T_t distortion.

Flow features such as shockwaves are often connected to observations in distortion transfer and generation. In 2015, Spencer et al conducted a study using proper orthogonal decomposition to streamline simulation of a rotor under distorted flow [6] and a sample of their data which shows shockwaves is shown in Figure 2.11. Using their decomposition methods, they observed that shockwaves in distorted regions moved upstream and downstream by as much as 40% of the chord in response to the pressure distortions. These shockwaves are believed to impact levels of distortion transfer and generation across a rotor. This exploration was continued in 2016 by investigating changes in shock movement in near-stall operating conditions [18]. This study found that in near-

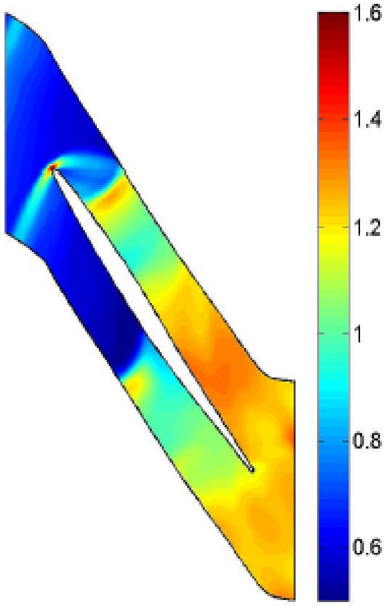

Figure 2.11: Sample of a blade passage used to study shockwaves using partial orthogonal decomposition [6].

stall operating conditions shock motion through a distorted region was decreased relative to the motion observed in near-design.

2.3 Experimental Methods

In order to understand the need for CFD simulations in studying inlet distortion, it is helpful to have a basic understanding of experimental methods for studying inlet distortion. This section will briefly explain the methodology common in experimental inlet distortion studies. For a more detailed explanation of experimental inlet distortion work, the reader is referred to sources [7, 12, 19].

Traditionally, experimental methods made up the entirety of research into inlet distortion. They offer the most realistic data about impacts of inlet distortion since they use real flows through real geometry and remain the authoritative standard for inlet distortion work. However, experimental methods come with limitations and downsides.

First and foremost, an experimental study of inlet distortion requires the creation of the turbomachinery and use of test facilities capable of running the turbomachinery in simulated environments. Manufacturing the test geometry and the operation of test facilities is expensive, making a small scale test difficult to justify. The need for physical components means adjustments to blade shape or fan design are not rapidly possible. A sample experimental setup is shown in Figure 2.12.

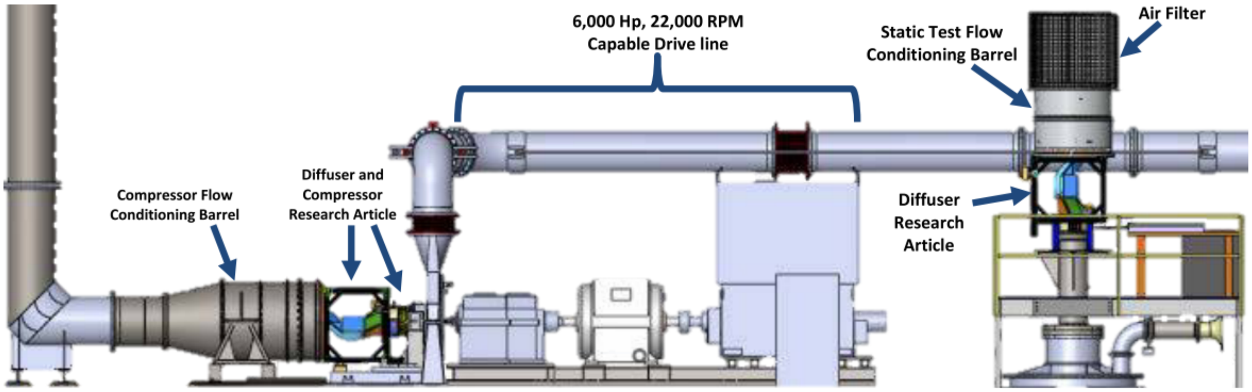

Figure 2.12: Experimental setup used for inlet distortion research [7].

In order to measure flow parameters, rakes of sensors are inserted into the flow. Due to practical limitations, the number of sensors and their location are often restricted to prevent severe disturbances to the airflow. A sample inlet rake with pressure taps is shown in Figure 2.13. This means data is only collected at a few discrete locations at any given time during a test. Moving rakes and averaging techniques can often be used to overcome this limitation to study a full-annulus flow field. Additionally, airflow at the blade surface, where shocks or boundary layers may be impacting distortion is difficult to observe in an experimental setup. Data obtained in experiments also depends on the fidelity of the sensors used and that they have been properly configured for the experiment.

In order to generate the inlet distortions in an experimental setup, an upstream screen similar to one shown in Figure 2.14 may be used. The patterns generated by these screens are difficult to precisely control, which in turn makes it challenging to conduct as study on small scale elements of the distortion pattern. In and of themselves, these screens are a challenge to design and manufacture to produce the desired pattern.

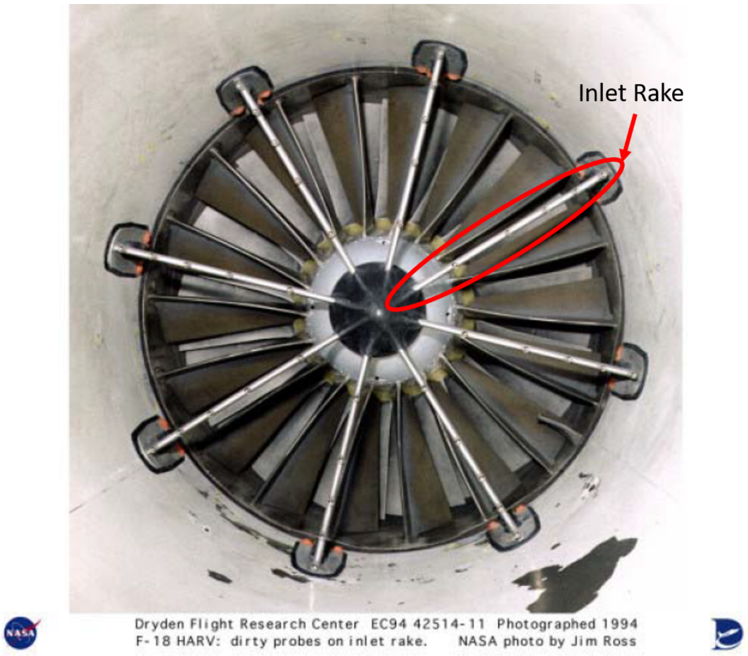

Dryden Flight Research Center EC94 42514-11 Photographed 1994
F-18 HARV: dirty probes on inlet rake. NASA photo by Jim Ross

Figure 2.13: Experimental inlet rake used by NASA for testing [2].

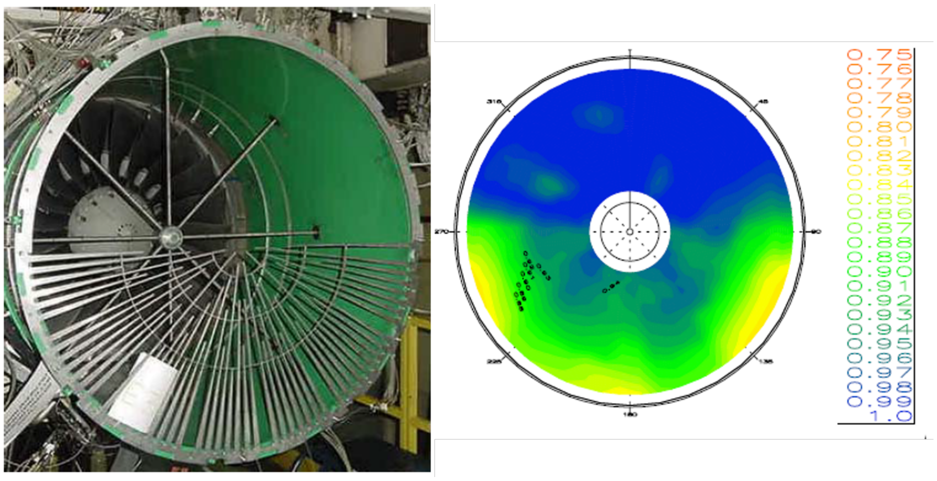

Figure 2.14: Example of inlet distortion generation screen used in experimental tests [2].

Combined, these limitations present challenges which limit the types of studies which can be performed using experimental methods. Computational simulations, which are reviewed in the following section, can be used to overcome some of these limitations, but come with their own downsides. The results from computational studies can ideally be used to better design experimental studies.

2.4 Computational Methods

Fluid dynamics problems, such as inlet distortion simulations, can be solved using the Navier-Stokes equations. Developed in the 1800's, these equations describe in great detail how pressure, temperature, and density of a fluid are related. The Navier-Stokes equations consist of three equations. Equation 2.1 represents conservation of mass, Equation 2.2 conserves momentum, and Equation 2.3 conserves energy. Together, they form a complete representation of fluid flows.

$$\frac{\partial \rho}{\partial t} + \nabla(\rho \vec{V}) = 0 \tag{2.1}$$

$$\rho \frac{\partial \vec{V}}{\partial t} + \rho \vec{V} \cdot \nabla \vec{V} = -\nabla p + \vec{g} + \mu \nabla^2 \vec{V} + (Other\ Forces) \tag{2.2}$$

$$\frac{\partial(\rho T)}{\partial t} + \nabla \cdot (\rho T \vec{V}) = \nabla \cdot (\frac{k}{c_p} \nabla T) + \frac{\dot{q}}{c_p} \tag{2.3}$$

Due to interdependencies between the three Navier-Stokes equations, analytically solutions without simplifying assumptions are often difficult to work out. For the case of studying inlet distortion, the required simplifying assumptions remove significant aspects of the flow which we aim to study, such as compressibility effects and full three dimensional flow. Turbulence, which is present in distorted flows, adds additional stress terms to the Navier-Stokes equations which must be considered.

To address these issues, the Navier-Stokes equations can be discretized allowing for simpler, but still accurate, solutions over small volumes which make up a larger fluid domain. Turbulence can be accounted for by Reynolds-Averaging the base Navier-Stokes equations. This solution method is often solved using computers and is packaged into what is called a computational fluids dynamics (CFD) solver. CFD software is able to take a fluid region, break it into small solvable chunks, or cells, and solve the Reynolds-Averaged Navier-Stokes equations for each cell. The common form of the Navier-Stokes used in these solvers includes unsteady effects and is called the Unsteady Reynolds-Averaged Navier-Stokes (URANS) equations. These powerful CFD codes have enabled designers and researchers to simulate complex fluids dynamics problems accurately on a computer.

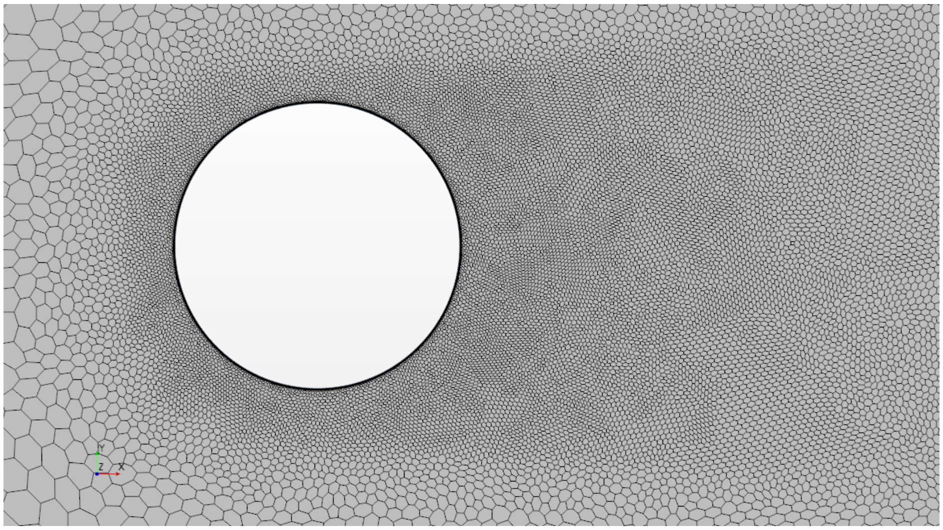

Figure 2.15: Sample CFD mesh of a cylinder in cross flow. Flow is from left to right.

This thesis uses a CFD Package called STAR-CCM+, which is a commercially available URANS solver with a wide assortment of powerful tools. To help those unfamiliar with CFD workflow, the basic setup of a CFD solver will be reviewed here. Details regarding the simulation setups for this thesis will be presented in Chapter 3.

To create a CFD simulation, we start with a geometric model, such as the rotor geometry shown in Figure 1.2. Once the CAD geometry is loaded into the CFD solver, the three-dimensional fluid region surrounding the geometry is broken up in to cells in a process called mesh generation. There are many techniques and best practices to ensure that the mesh will accurately capture the fluid flow. Figure 2.15 shows a sample mesh generated using STAR-CCM+ for a cylinder in cross flow from left to right. Note that the cell size is smaller near the surface of the cylinder as well as to the right of the cylinder. This ensures that flow features such as boundary layers and wakes are accurately captured.

With a sufficient mesh generated, boundary conditions are then imposed at the domain boundaries, such as the inlet, outlet, and any surfaces. Such boundary conditions might include an inlet distortion, initial velocity, rotation specification, pressure conditions, or no-slip wall conditions. Fluid models are selected, which specify what assumptions to use when solving the flow. This might include specification of a specific model to capture turbulence, steady vs time-dependent flows, as well as fluid type.

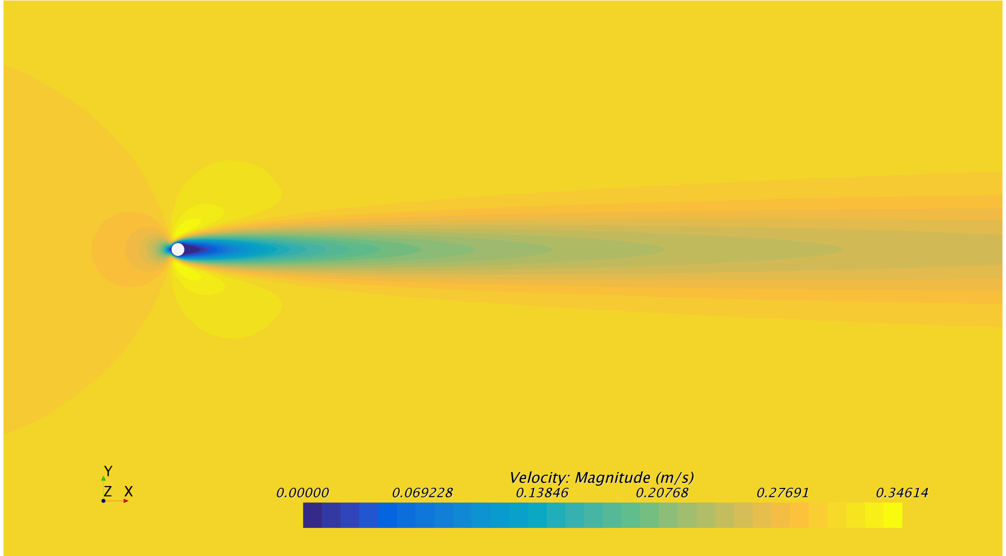

Figure 2.16: Sample output from STAR-CCM+ showing velocity magnitude contours for a simulation of a cylinder in cross flow. Flow is from left to right.

Once all the needed boundary conditions and models are selected, an initial solution is applied to the domain. The initial solution can either be specified by the user, or defined automatically by the solver. The goal of the initialization process is to apply a reasonable value for fluid properties to each cell, which will improve the simulated solution. Once the flow field is initialized, the solver can begin to iterate to a converged solution. Due to the discretized nature of the underlying equations, the solver must run many times to obtain a converged solution which accurately represents the flow. Metrics within the solver are used to determine when a simulation is converged. Once converged, the solution data can be represented and post-processed. A wide variety of results can be obtained during post-processing. A sample output showing velocity from a simulation of a cylinder in cross flow is shown in Figure 2.16.

As mentioned in the previous section, experimental methods were the traditional method for researching inlet distortion. However, advances in simulation methods and computing technology have made computational methods a viable method for conducting inlet distortion research. Computational simulations can be used to investigate a wider variety of inlet distortions with better control over distortion shape, can observe results at any location within the computational domain, and do not require the use of expensive test facilities. A major concern however, is how accurate simulations are compared to experimental data. Poor mesh quality, inaccurate model selection, incorrect boundary specification, and inherent numerical limitations can all compromise the validity of a simulation, resulting in results which are not representative of physical flows.

In 2010 Yao et al conducted a series of investigations which demonstrated the capability of computational methods to accurately investigate distortion [15, 20]. Flow was simulated through two multi-stage fan geometries under pressure and temperature distortions. They concluded that results obtained with CFD agreed well with experimental data, suggesting that CFD could be successfully used to investigate inlet distortion. Computational methods have since grown to make up a strong component of inlet distortion research, with many studies being conducted using CFD methods [3, 10, 11, 17, 21, 22]. CFD has enabled the investigation of a wide variety of flow phenomena associated with inlet distortion at levels of detail previously impossible with experimental tests.

As evidenced by concerns about the accuracy of CFD, there are limitations to using CFD to simulate the impacts of inlet distortion. The simulations can become immensely complex as research attempts to better reflect reality, requiring close attention to simulation setup and parameters. In addition, with a complex and high-speed geometry such as a fan or compressor the mesh quickly becomes enormous, consisting of hundreds of millions of cells. This makes the simulation files extremely large and difficult to work with on a conventional computer, instead requiring the use of a supercomputer cluster to open, adjust, and solve. Even with supercomputing capabilities, these simulations can take days to weeks to reach a converged solution. The need for supercomputing introduces additional complexities and costs with conducting a URANS simulation of inlet distortion, but tends to still be less than those required to conduct an experiment.

One particular challenge which faces those conducting CFD simulations is the level of detail to include in a simulation. In an ideal situation, every geometry element, every physics model, and the best mesh possible would be included in a simulation. This comes at enormous computational cost, resulting in simulations near impossible for even a supercomputer to solve. To address this, simulations are often created to balance computational costs with simulation detail. However, due to the circumferential variations which comprise most inlet distortions, a full-annulus (360° domain) must be simulated to accurately investigate inlet distortion, as opposed to using a simpler blade-passage only method.

The balancing act between cost and detail usually means that results from simulations do not directly correlate to physical flows and rather present trends that should be observed in a similarly set up experiment. One common way of balancing cost with accuracy is a conscious effort to reduce the number of cells in a mesh where possible, while still capturing essential flow features. One method for doing this is by excluding nozzle geometry downstream of the turbomachinery geometry. Nozzle geometry is generally used to control the operating point of the fan, and allows for flow redistribution downstream of the stator. Instead, a special non-reflective pressure boundary condition is used to simulate back pressure. This effectively reduces the number of cells and helps the simulation converge faster. As CFD continues to grow in application in inlet distortion research, it is important to ensure such simplifications are not altering the trends observed in any significant way.

2.5 Description of Distortion

The ability to simulate a wide variety of inlet distortion situations with CFD and experimental methods has resulted in a tremendous amount of data to help inform future turbomachinery designs. Describing the results from such studies in a way that give quantitative information is a challenge. Many results are presented qualitatively, which makes comparisons of results between studies challenging. In particular, quantifying levels of distortion transfer and distortion generation are of interest. As mentioned in Section 2.2, distortion transfer refers to how applied distortions interact with turbomachinery and distortion generation refers to distortion generated as the P_t distortion goes through the fan or compressor. Having a quantitative measure for describing these helps improve comparisons of results between studies.

In early distortion research, each research group used their own quantitative descriptors to describe their results. To attempt to unify research results, particularly when describing inlet distortion patterns generated in experimental tests, the Society of Automotive Engineers (SAE) created a committee to create a unified distortion description standard. The resulting aerospace recommended practice (ARP) document was published as ARP 1420, which has since undergone several updates and modifications, with ARP 1420-C being the latest release [8, 23].

The purpose of ARP 1420, as stated in the document, is to quantify the effects of P_t inlet distortion on turbine engines by providing a standard for distortion description, stability assessment,

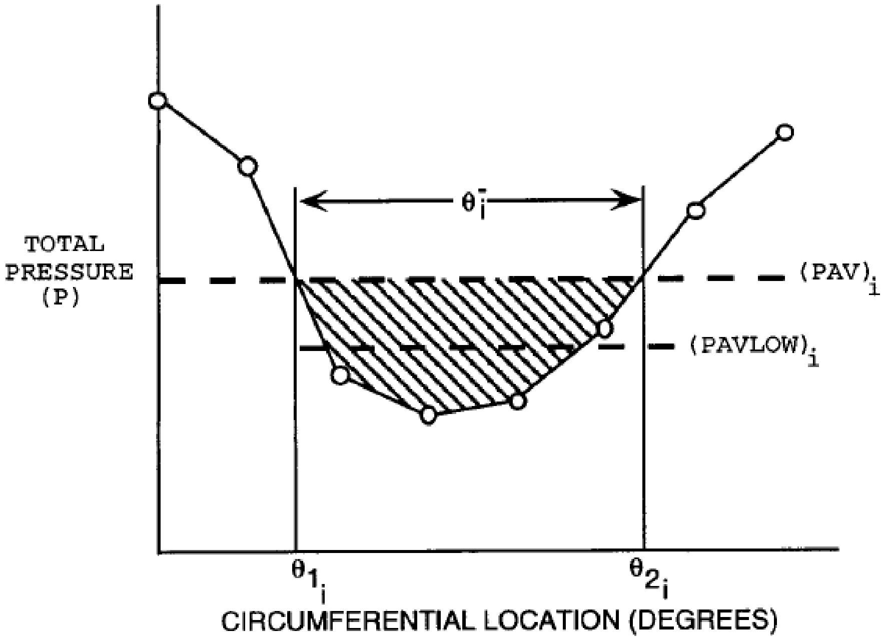

Figure 2.17: ARP 1420 circumferential distortion description [8].

and testing. Distortion description is achieved by presenting a series of standard distortion descriptor elements, which together form a distortion descriptor system. The distortion elements outlined in ARP 1420 include circumferential distortion intensity, extent, and multiple-per-revolution (MPR) accompanied by a radial distortion element. Circumferential intensity ($(\frac{\Delta PC}{P})_i$) describes the magnitude of the pressure defect as defined in Figure 2.17 and equation 2.4 where PAV defines the average total pressure and PAVLOW described average total pressure of the low pressure region. The extent (θ_i^-) is the angular region in degrees of the distortion and is calculated using equation 2.5. MPR describes the number of low pressure regions around the circumference. Radial distortion compares the average pressure of a constant radius ring to the average of the full face. ARP 1420 then provides a methodology for using these elements to describe an inlet distortion and perform a stability and performance assessment.

$$(\frac{\Delta PC}{P})_i = (\frac{PAV - PAVLOW}{PAV})_i \tag{2.4}$$

$$\theta_i^- = \theta_{2_i} - \theta_{1_i} \tag{2.5}$$

A limitation of ARP 1420 is its intent to only describe distortion at the aerodynamic interface plane, or AIP. The AIP is located just upstream of a turbine engine and is where inlet distortion in generally defined. While APR 1420 provides clear guidance for quantifying distortion levels at the AIP, it does not offer extensions to defining distortion levels downstream at different stations throughout the engine. This is likely due to the fact that ARP 1420 is primarily intended for distortion description in experimental testing, where detailed information regarding distortion is not readily available at different planes throughout the engine. In addition, ARP 1420 was developed with distortion profile modeling in mind, rather than the complex task of describing distortion patterns with both high and low distortion components.

To address the need for a more powerful set of descriptors capable of describing distortion at any point in a fan or compressor, Peterson proposed a series of Fourier Series based descriptors in 2017 [9]. These descriptors use a Fourier series reconstruction of a radial slice of raw data from a URANS simulation to calculate a series of descriptors which have proven useful for quantifying distortion. As a review, a Fourier series uses a series of sinusoidal waves of varying phases and amplitudes to represent a function.

Equation 2.6 shows the basic formulation of the Fourier series, where A_n represents the modal amplitude of mode n and ϕ_n the modal phase of mode n.

$$s_N(x) = \frac{A_0}{2} + \sum_{n=1}^{N} A_n \cdot \sin\left(\frac{2\pi n x}{p} + \phi_n\right) \tag{2.6}$$

Peterson used information made available in the Fourier reconstruction of raw simulation data to produce four distortion descriptors. Magnitude of the distortion is calculated using the amplitudes of the individual terms of the Fourier series. These can be evaluated on a modal basis and are called modal amplitude distortion descriptors. An additional amplitude descriptor is generated by summing the modal amplitudes together (ΣA) to form the total amplitude distortion descriptor. A similar descriptor for phase shift is calculated by comparing the modal phase between axial locations in the engine. For example, one could calculate the phase shift in P_t between the AIP and the axial plane immediately following the rotor by subtracting the first modal phase of the Fourier reconstruction at each plane. This helps identify any circumferential movements in distortion and can assist in quantifying the observed phase lag between P_t and T_t distortion [10, 15, 20].

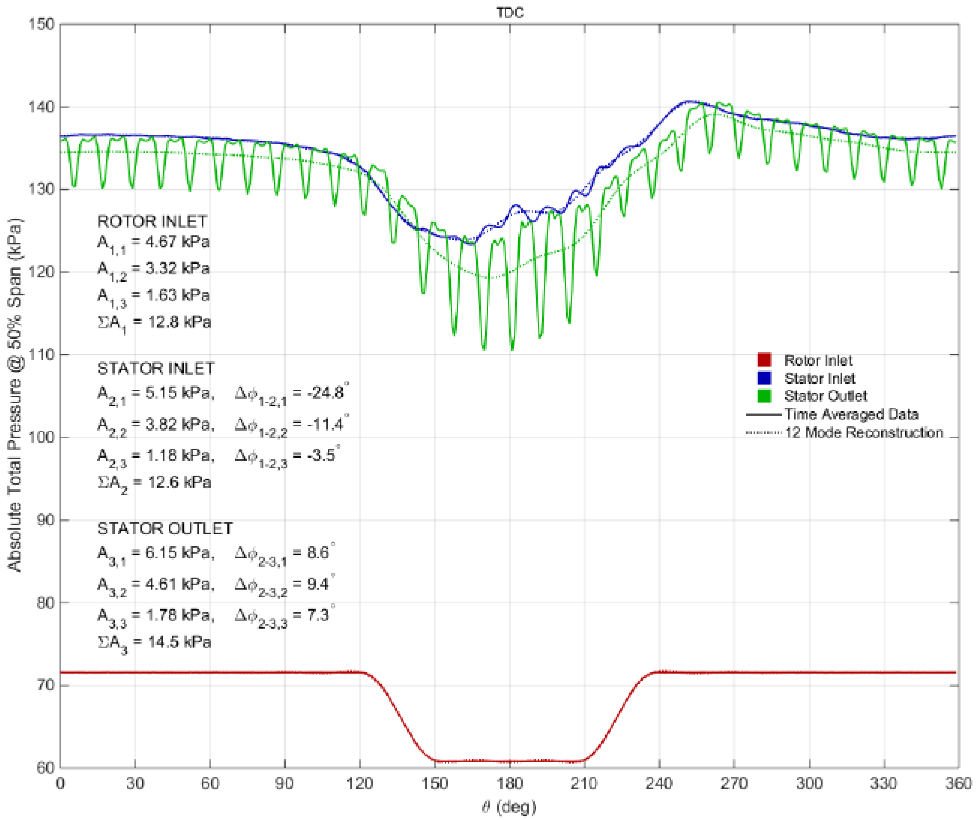

Figure 2.18: Example of distortion results obtained using Fourier based methods. Shows P_t distortion transfer for a URANS simulation of rotor 4 at 50% span [9].

These descriptors allow for quantification of distortion at any given plane and radius within a piece of turbomachinery. The amplitude descriptors help describe the magnitude of distortion at any given point, and comparisons between the amplitude descriptors at the AIP and a downstream plane can give insight into levels of distortion generation. The phase shift descriptor helps quantify circumferential movements and shape of the distortion. A sample of some results using Fourier based descriptors is shown in Figure 2.18 and shows modal amplitudes, total amplitudes, and phase calculated at various stages in rotor 4. These Fourier based descriptors have been used in several works to quantify and compare distortion [3, 9, 11].

CHAPTER 3. METHODOLOGY

This chapter will review details regarding the methods used to obtain the results presented in this thesis. Methods for each of the three studies comprising this thesis will be presented separately.

3.1 Inlet Distortion Variation Study

This section presents details for the methodology used to complete the inlet distortion variation study using Rotor 4. The objective of this study was to simulate a series of varying inlet distortion patterns in Rotor 4 and to explore differences in levels of distortion transfer and generation observed as a result of the pattern variations.

3.1.1 Geometry

The geometry used in this study was the Parametric Blade Study (PBS) Rotor 4 fan [4]. Rotor 4 was designed to be a state-of-the-art fan with high through flow, high aerodynamic loading, and a low hub/tip ratio. At design conditions, the rotor tip speed is 457 m/s. At this speed, 60% of blade height experiences supersonic relative Mach numbers. Rotor 4 was also designed with a small throat area and low suction surface curvature for the purpose of investigating the ability to control shock strength. The design of rotor 4 is similar to that of many fans in operation today making it a relevant design for distortion research. The performance of rotor 4 was quantified and discussed at length by Law and Puterbaugh [4].

The rotor 4 geometry is shown in Figure 3.1. The rotor, indicated in orange, rotates clockwise at 20,200 RPM, while the stator shown in grey remains stationary. The rotor has 20 blades and the stator has 31 blades. Table 3.1 contains additional design parameters for rotor 4. The flow rate, pressure ratio, and efficiency specified in the table are from undistorted experimental testing.

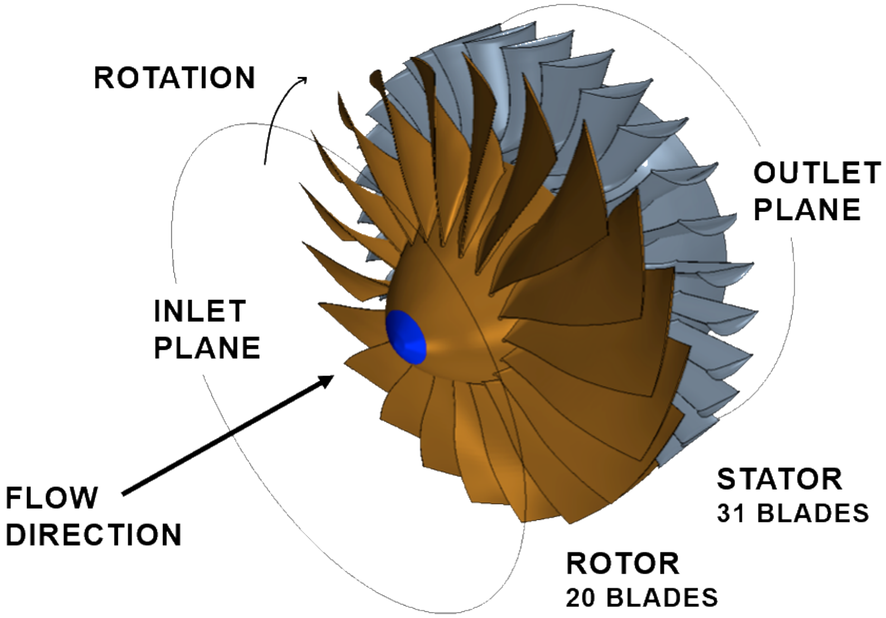

Figure 3.1: Rotor 4 geometry.

Table 3.1: Rotor 4 Design Parameters.

Design Parameter	Value
Number of Blades (Rotor)	20
Number of Blades (Stator)	31
Outer Diameter (Tip)	0.4318 m
Running Tip Clearance	0.508–0.635 mm
Flow Rate	27.56 kg/s
Pressure Ratio	2.057
Rotor Efficiency	94.60%
Rotation Speed	20,200 RPM

Several key locations in the geometry are indicated in Figure 3.2, which shows a meridional view of rotor 4. The AIP refers to the aerodynamic interface plane and is where inlet conditions, such as inlet distortion profiles, are applied. The rotor inlet (RI) is a plane preceding the rotor, where induced distortion can be observed. The majority of the data in this thesis is extracted at the stator inlet (SI), as the stationary stator tends to have little impact in distortion generation or transfer compared to the rotor. The stator inlet is also one of the few locations where properties can be collected experimentally, meaning any comparisons to experimental data would likely be made at this location. Exit boundary conditions are applied at the stator outlet (SO). Performance

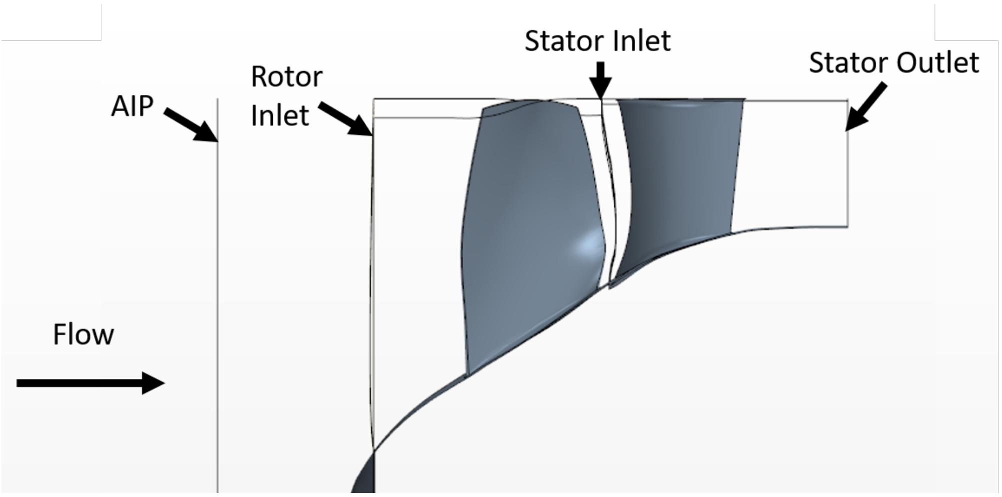

Figure 3.2: Rotor 4 plane identification.

metrics for the rotor are calculated using values between the AIP and the stator inlet, while full stage performance metrics are calculated using values between the AIP and the stator outlet.

3.1.2 Mesh

The mesh for Rotor 4 was generated using the recommendations for turbomachinery meshes developed by Marshall Peterson [24]. These practices are reviewed in detail in section 4.1 of his Master's Thesis. They combine best practices from the STAR-CCM+ manual, recommendations from specialists at CD-Adapco, and considerations from Nessler [7] and Sanders [25]. These best practices balance mesh quality with simulation size and computational cost. Some of these details will be reviewed here, but the reader is referred to the work by Peterson for a full review of the mesh [24].

The mesh is generated using the built in STAR-CCM+ polyhedral mesher. Three regions were defined, corresponding to the spinner region (between the AIP and RI), rotor region (between RI and SI), and stator region (between the SI and SO). Structured prism layers were generated near walls within each region to properly resolve boundary layers. These prism layer cells assist in capturing the high shear flows near the walls within the simulation. Cells within a prism layer are long in the streamwise direction and thin perpendicular to the wall. This unique geometry enables the solver to resolve the viscous effects caused by boundary layers near walls. An unstructured polyhedral grid was used away from the walls. The number of prism layers varied from 8 to 12 cells depending on the wall type (casing, hub, or blade surface). The mesh has an average y+ of 10.

The cell counts in the spinner, rotor and stator regions are 14.9M, 92.3M and 185.9M for the full annulus, respectively. The total cell count of the computational domain was 293.1M. The mesh has been used successfully in previous studies [3, 9, 11] simulating distortion transfer and generation.

3.1.3 Boundary Conditions

In order to study the impacts of changes to inlet distortion pattern, several inlet distortion patterns were generated. The inlet distortion profiles are comprised of two series: one with a 90° distortion sector and the second with a 135° distortion sector. The two series of profiles are shown in Fig. 3.3. The percent distortion in each sector is 15% as defined in Equation 3.1 where $P_{t,max}$ is the maximum P_t and $P_{t,min}$ is the minimum P_t in the sector. This distortion is centered around top dead center (TDC), which corresponds to 180° . Each profile has a parabolic boundary layer profile applied at the casing. The boundary between distorted and undistorted regions in the inlet profile is based on the circumferential distance it takes to transition from clean (high) P_t to distorted (low) P_t.

$$PD = \frac{P_{t,max} - P_{t,min}}{P_{t,max}} \cdot 100\% \tag{3.1}$$

The transition between distorted and undistorted flow in each sector was modeled using a half-cosine wave. Each inlet profile series includes one base profile and two profiles where the cosine wave representing the circumferential distortion transition was modified. Each modification increased the wavelength of the cosine wave, which is equivalent to a less-abrupt or more gradual transition in distortion. The initial and unmodified profile is labeled as the “base” profile in Fig. 3.3. The “base” profiles have a transition wavelength equal to approximately 4.5% of the casing circumference. “Shape 2” profiles have the least abrupt transition for each series, and “shape 1” profiles have a transition abruptness halfway between that of the “base” and “shape 2” profiles. The “shape 2” profiles have a transition wavelength of approximately 10% of the casing circumference.

The 90° sector was chosen through evaluation of canonical patterns in the literature [23] and the circumferential extent of patterns such as those shown in [26, 27]. The 90° sector profile was chosen to mimic profile shapes observed at the exit of aggressive S-duct diffusers. As the flow passes through the S-duct, counter rotating swirl regions, known as twin swirl, form along the symmetric axis of the diffuser. The twin swirl generates counter rotating vortices (vortex swirl) that form at top dead center (TDC). This swirl causes a velocity driven 90° low P_t distortion region to form at TDC. Further details are provided in [9]. The 135° sector was selected to evaluate the impact of the circumferential extent of the inlet distortion on distortion transfer and generation and sits halfway between the 90° sector size and 180° distortion size.

The inlet boundary condition for each simulation was one of the P_t profiles shown in Fig. 3.3. A constant inlet T_t of 288K was specified and no swirl was explicitly set at the AIP. The inlet plane was selected based on future availability of experimental data (P_t and flow angles) at the axial location. At the time of the simulation no experimental data was available.

The static pressure exit boundary condition was chosen to result in an operating point near design. The exit boundary condition was applied at approximately 0.85 stator chord downstream of the stator trailing edge. The exit boundary location was selected based on the location of facility adaptive hardware in the experimental setup. Although the interaction of the boundary condition at this distance does negatively influence the back pressuring of the stator row, the simulation does provide a meaningful demonstration of T_t distortion generation in the rotor. For simplicity and comparison to harmonic balance simulations [28], the facility adaptive hardware and other downstream components were not incorporated.

3.1.4 Models and Simulation Parameters

STAR-CCM+ version 13.02 was used to conduct full annulus simulations of PBS Rotor 4 with each inlet distortion pattern. Initial velocities in the computational domain were provided using the solution of a steady-state clean inlet (uniform inlet P_t) simulation provided by a previous graduate student. Through experience, this practice has proved to improve stability of the simulation and expedites convergence. The coupled implicit unsteady solver in STAR-CCM+ was used to simulate the distortion patterns over the full-annulus of rotor 4. Exact wall distance, ideal gas, and fully turbulent flow was specified. The implicit unsteady solver was selected. A coarse time step

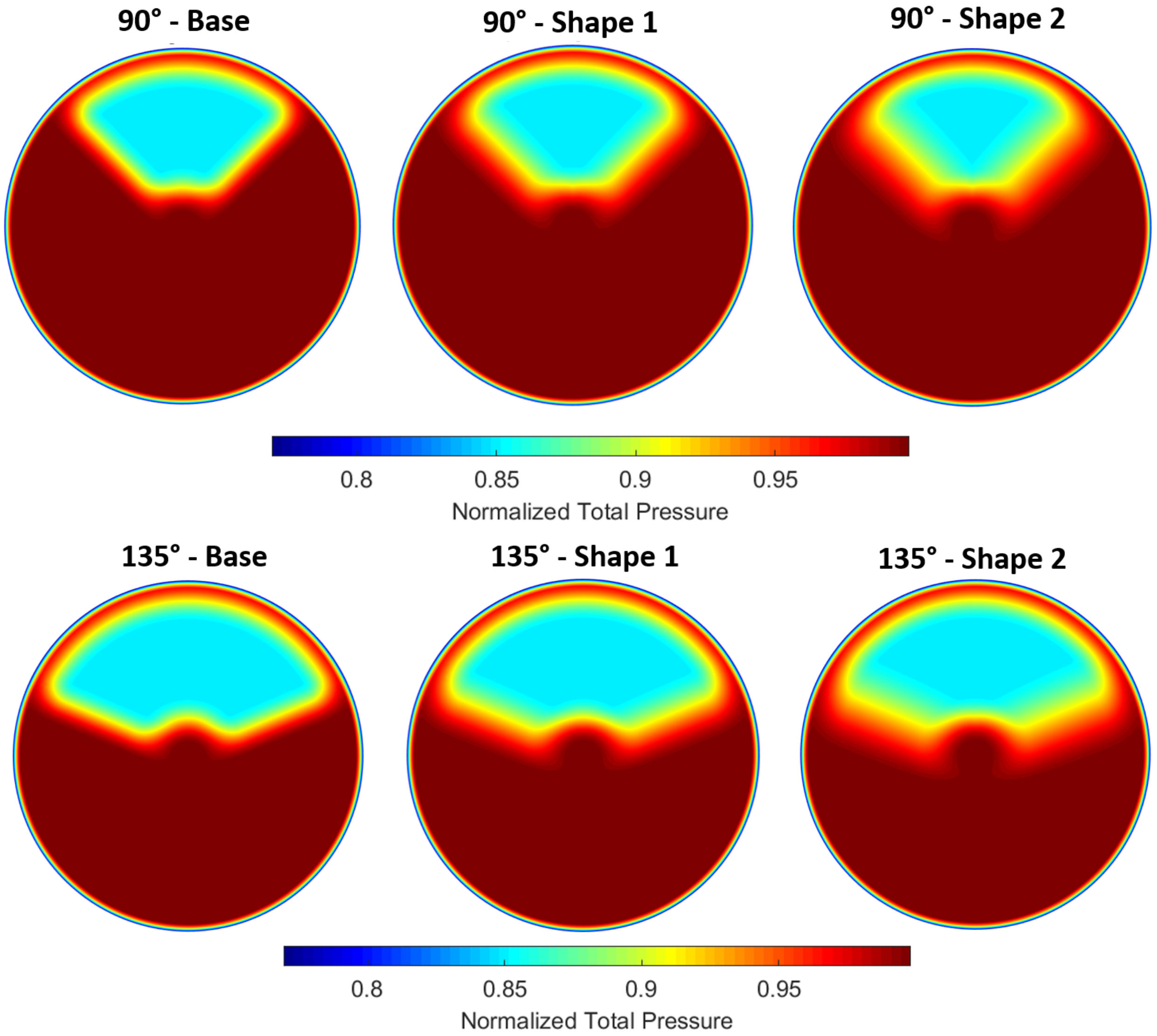

Figure 3.3: Top: Normalized inlet distortion profiles for 90° sector (top) and 135° sector (bottom). View is forward looking aft. Sectors are normalized relative to the maximum P_t at the AIP. Rotor rotation is clockwise in this view.

equivalent to 2° per step was initially used to resolve large scale flow features, after which a smaller step equivalent to 1/4° per step was used to resolve small scale flow physics. The coarse time step used 40 inner-iterations per time step, and the fine step used 10 inner-iterations. The SST K-omega turbulence closure model was used, which is recommended for turbomachinery simulations.

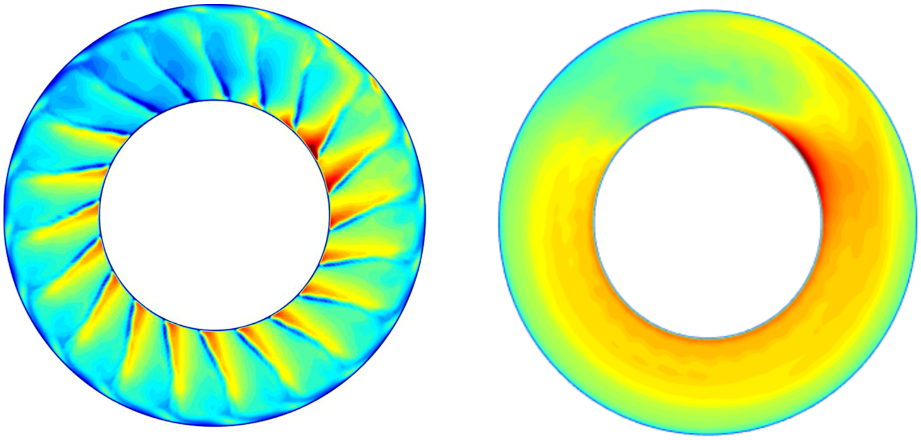

Time Accurate

Time Averaged

Figure 3.4: Comparison of time-accurate (left) and time averaged (right) data at the stator inlet. Contours shown are of total pressure at the stator inlet.

3.1.5 Time Averaging

Results from the simulation are initially time-accurate, meaning they represent a single instance in time. In order to eliminate the regularly occurring rotor and stator wakes, all outputs were time-averaged. This is accomplished by taking a series of regularly spaced snapshots of results at sequential time steps. These snapshots are then averaged together. An illustration of the difference between time-accurate and time-averaged contours is shown in Figure 3.4. Note how in the time-accurate contour, the dominant feature are the blade wakes. This makes flow features, such as the high pressure region at the hub seen in the time-averaged contour, more difficult to discern. Time-accurate data has its own place however and identifies other important flow features such as shock waves.

Time averaging is considered most accurate when completed over a full rotor revolution. This requires large amounts of data and results in long post-processing times. An investigation made in connection with this research explored whether time averaging could be completed over smaller circumferential segments, such as one blade passage, or 18° for the rotor 4 geometry. The study compared time averaged flow fields after averaging over one blade passage, two blade passages, five blade passages, and 10 blade passages against the standard full rotation time average. It was found that the one blade passage results were minimally different (less than 0.01%) from the full rotation time average. This suggests that time averaging over a single blade passage is sufficient for time averaging.

For this thesis, all time averaging was completed after the simulation was deemed to be sufficiently converged. The aforementioned time averaging study was completed as results for this thesis were obtained, meaning that some early data was time averaged over a full rotor rotation of 360 degrees was completed with data extracted at time steps equivalent to 1° increments. Later data was time averaged over a single blade passage, or 18° with data extracted at time steps equivalent to 1° increments.

3.1.6 Blade Loading

Blade loading helps describe the design and performance of the fan stage. A blade loading analysis was performed to determine how each inlet distortion profile produced radial and circumferential variations in power through the rotor blade row. This was done by extracting static pressure data at an instant in time on each blade at 10%, 30%, 50%, 70%, and 90% spans. The static pressures on the suction side and the pressure side were then integrated from leading edge to trailing edge to determine the power at each of the five radial locations on each blade. Equations 3.2 and 3.3 were used for this integration:

$$\dot{W}_{pressure} = \int P_{pressure} \cdot U(r) \cdot dA \tag{3.2}$$

$$\dot{W}_{suction} = \int P_{suction} \cdot U(r) \cdot dA \tag{3.3}$$

$U(r)$ is the blade speed as calculated by $U(r) = N_1 \cdot r$ where N_1 is the rotational speed in radians per second, and r is the radial location on the blade. The last terms in the integrals are defined by $dA = h \cdot dz$, where dz is a differential length element in the axial direction, and h is the approximate height of the differential region for which power is being calculated. This height term for each area was calculated as 1/5 the distance from hub to tip because five uniformly-spaced spans were used. These terms are portrayed in Fig. 3.5.

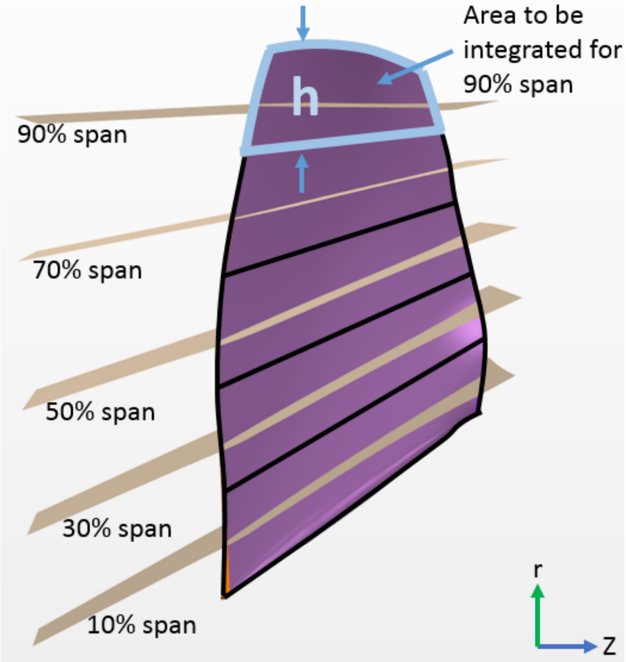

Figure 3.5: Blade loading parameters visualization.

3.2 Nozzle Study

This section presents details for the methodology used to complete investigation of the impact of adding nozzle geometry to an inlet distortion simulation. The objective of this study was to determine if the addition of a nozzle significantly impacted the results of an inlet distortion simulation. The simulations completed for this study will be compared to work by Soderquist which did not use a nozzle and instead used the simpler exit pressure boundary condition [3]. It is important to note that with inlet distortion simulations, emphasis is placed on revealed trends, rather than magnitudes. As such, comparisons between simulations with and without a nozzle will focus on comparing trends rather than magnitude.

3.2.1 Geometry

PBS rotor 4 geometry was used as the turbomachinery geometry for this study, as simulations have already been completed using this rotor without a nozzle by previous students. Details for this geometry are available in Section 3.1.1. Nozzle geometry was added to the rotor 4 geometry

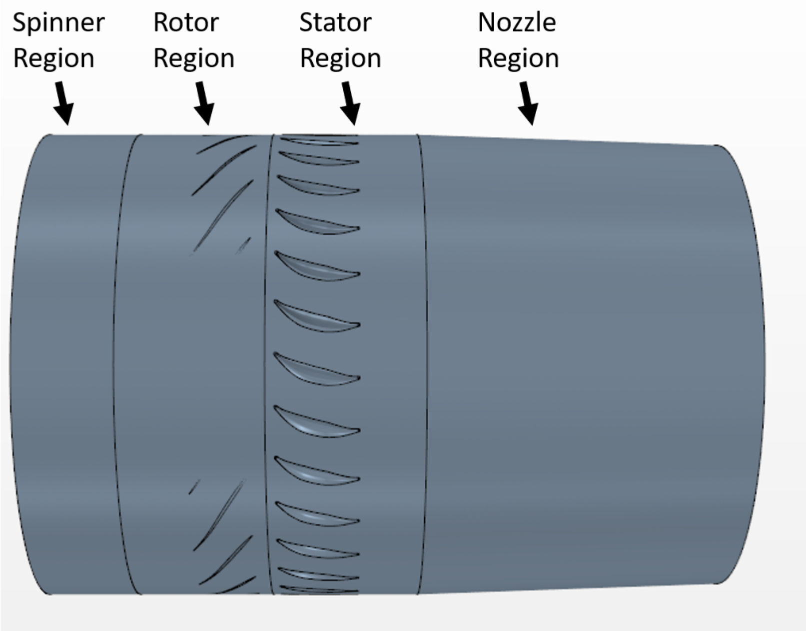

Figure 3.6: Nozzle geometry.

immediately downstream of the stator outlet. This was accomplished by using the STAR-CCM+ provided modeling tools. This extended geometry is shown in Figure 3.6.

The nozzle extends approximately 0.28m downstream from the stator exit, which corresponds to approximately 5 stator chords. This length should allow for adequate flow adjustments without impacting the flow from the stator. The nozzle features a variable exit area, which enables control over fan operating condition. Different fan operating conditions are obtained by changing the nozzle exit area. This area is controlled by altering the angle of the nozzle, with the angles used for control indicated in Figure 3.7. This nozzle geometry addresses the concern that having an exit boundary close to the stator impacts the simulation by moving the exit boundary further downstream.

A series of exit areas were simulated to attempt to match the near-stall, near-design, and choked simulations presented by Soderquist [3]. Operating points near stall were achieved by restricting the nozzle exit area. Operating points near choke were achieved by lowering the nozzle back pressure with the nozzle area set to a constant area.

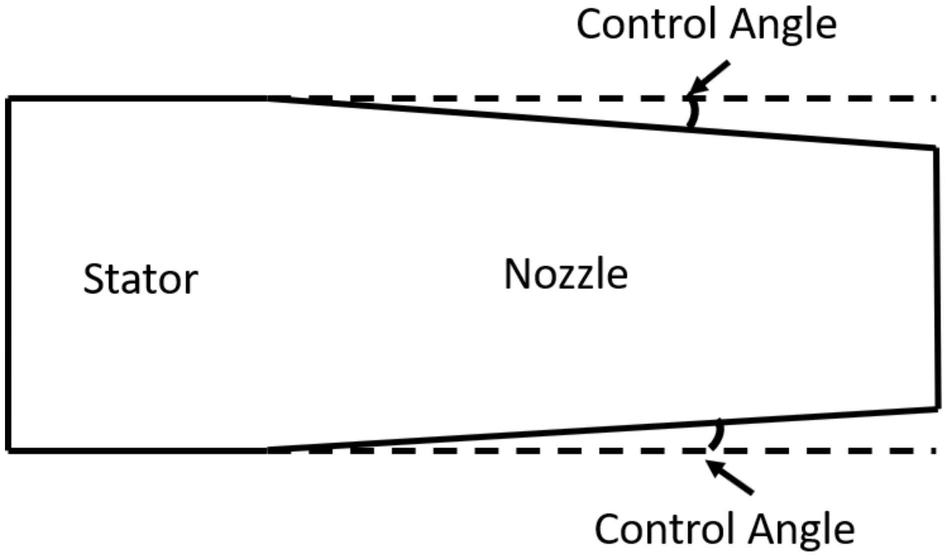

Figure 3.7: Angles used for nozzle area control.

3.2.2 Mesh

A new region was defined for the nozzle in addition to the spinner, rotor, and stator regions of the rotor 4 geometry. The mesh of the nozzle region was matched as closely as possible to the stator region mesh. This was accomplished using the STAR-CCM+ polyhedral mesher. Base cell size away from walls was matched with the value from the stator region mesh. The number of prism layers and total height were additionally matched, at 8 layers and a height of 12% the mesh base size. A mesh interface was specified between the stator and nozzle to enable transfer of flow data from the stator to the nozzle. A snapshot of the mesh at this interface is shown in Figure 3.8, which shows the matching cell size and prism layers. The nozzle mesh added approximately 3M cells to the simulation, bringing the total cell count to 296M cells for the full-annulus domain.

3.2.3 Boundary Conditions

A simple 15% 90° distortion pattern was used as the inlet P_t distortion condition for this simulation. This distortion pattern is shown in Figure 3.9 and is the same as the one used by Soderquist in his work which will allow a direct comparison in results [3]. A constant inlet T_t of 288K was specified and no swirl was explicitly set at the AIP.

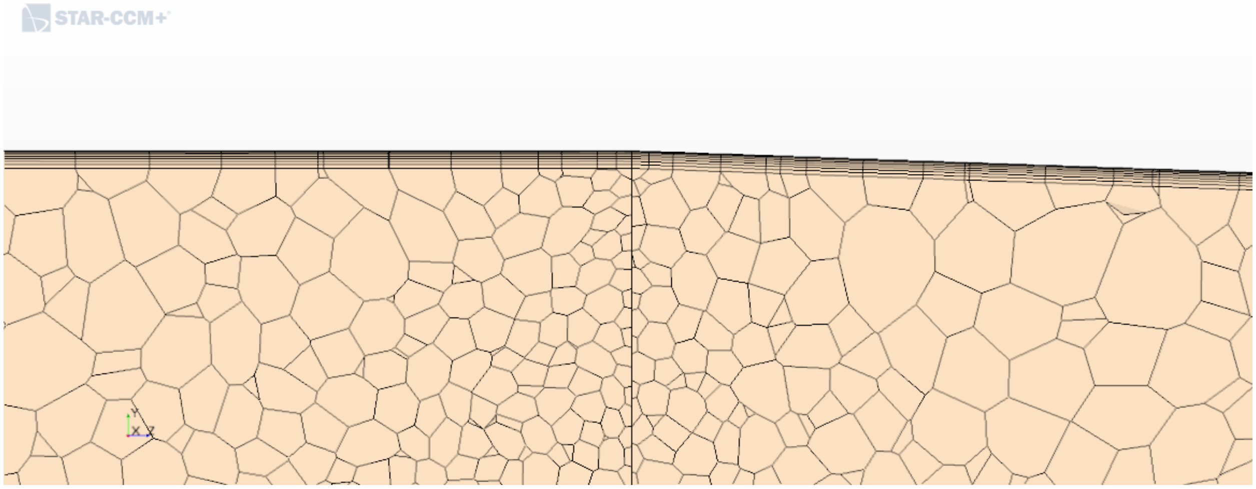

Figure 3.8: Boundary layer transition from stator region to nozzle region.

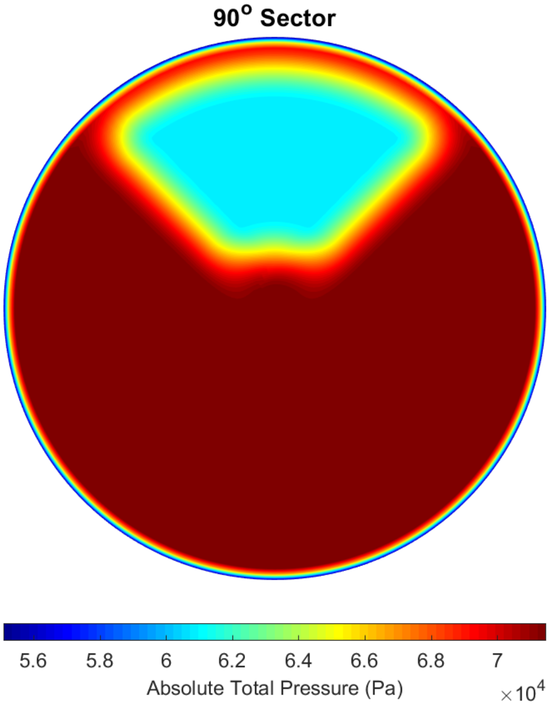

Figure 3.9: 90° distortion sector used for nozzle simulations.

The exit boundary condition was located at the end of the extended nozzle domain. The static pressure at the exit of the nozzle is specified as a constant static pressure boundary condition and is set to ambient conditions at sea level (14.69 psi). This was configured using methodology demonstrated by Vahdati in his study of variable area nozzles [29]. The exit condition specified chokes the nozzle at mass flow rates away from stall. At lower flow rates, the nozzle does not choke, and rather adjusts so that the static pressure drop through the nozzle matches the exit static pressure specified. This allows the exit area to determine the flow rate through the stage regardless of whether the nozzle is choked or not.

3.2.4 Models and Simulation Parameters

STAR-CCM+ version 13.02 was used to conduct a series of simulations at various operating conditions with rotor 4 with added nozzle geometry. URANS solver configuration and model selection matched the configuration for the inlet distortion variation study outlined in Section 3.1.4.

3.3 Phase Shift Study

This section presents details for the methodology used to evaluate and compare descriptors used to quantify phase shift. For our purposes, a good phase shift descriptor should help quantify circumferential changes in distortion as it passes through a blade row. Simulations completed by Soderquist as part of his thesis were used in this analysis, along with a simplified phase shift parameter he proposed [30]. His results are expanded by a more thorough investigation into the mechanics resulting in the observed phase shift behavior as well as a comparison to several Fourier based phase shift metrics.

3.3.1 Simulation

The simulations for this study were completed previously by Soderquist and are detailed in section 3.1 of his thesis [30]. They consist of URANS simulations of rotor 4 under the distortion pattern shown in Figure 3.9 at near-stall, near-design, and choked operating conditions.

3.3.2 Phase Shift Descriptors

Several methods are used in this study to attempt to quantify circumferential shifts in distortion. The merits and limitations of each will be explored as results are presented.

Descriptors which are based off of a Fourier reconstruction of data as defined in Equation 3.4 were introduced by Peterson [9]. The term of interest in the equation is ϕ_n, which is the phase of each mode of the Fourier transform.

The first method used to describe phase is referred to as the Modal Fourier Phase Shift. This descriptor compares ϕ_n for each mode between axial locations. For example, $\phi_{1,SI}$ (mode 1 phase at the SI) is subtracted from $\phi_{1,RI}$ (mode 1 phase at the RI) with the result being presented as the Modal Fourier Phase Shift $\phi_{1,SI-RI}$ This phase descriptor was used by Peterson [9] to describe changes in distortion shape and distortion translation. If all the modal phases shift a similar amount in either a positive or negative direction, it can be concluded that the distortion has shifted uniformly. However, if some of the modes have increased or decreased more than others, the distortion has changed shapes.

$$s_N(x) = \frac{A_0}{2} + \sum_{n=1}^{N} A_n \cdot \sin\left(\frac{2\pi nx}{p} + \phi_n\right) \tag{3.4}$$

In an attempt to combine modal information to obtain a single parameter for phase shift, a variation on the Modal Fourier Phase Shift is now defined. The Total Fourier Phase Shift descriptor is defined as ϕ_T and sums the modal phases at a given axial location. These sums are then compared between axial locations, such as between the SI and RI, resulting in $\phi_{T,SI-RI}$. This is defined in Equation 3.5. The goal of this descriptor is to define a total phase parameter in a similar manner to the total amplitude distortion descriptor.

$$\phi_{T,SI-RI} = \sum_{n=1}^{N} \phi_{n,SI} - \sum_{n=1}^{N} \phi_{n,RI} \tag{3.5}$$

Modal phase shifts can be either positive or negative, which in some cases results in cancellation of important modal phase information when performing the summation which is key to the Total Fourier Phase Shift. To address this limitation a third Fourier based descriptor is now defined. This new descriptor uses a root-sum-square (RSS) method to average the modal differences between axial locations. This method, referred to as the RSS Modal Phase, takes the RSS of the modal phases between axial locations, as shown in Equation 3.6. This method captures an average magnitude of modal phase shift, which should provide useful information regarding circumferential shifts in distortion.

$$\phi_{RSS} = \sqrt{\sum_{n=1}^{N} \phi_{n,SI-RI}^{2}} \tag{3.6}$$

In 2019, Soderquist proposed a simplified phase shift descriptor and briefly explored results with this parameter [30]. This descriptor does not rely on the modes of a Fourier reconstruction, but uses the peaks and valleys of property traverses to quantify phase shift. The method is illustrated in Fig. 3.10 for a traverse of P_t. Phase shift is defined as the difference between the centers of the distorted regions at two axial locations. At the rotor inlet, the center of the distorted region is at 180°, as defined by the inlet distortion profile. After passing through the rotor, the distortion pattern changes. The center of the distorted region after passing through a blade row is found by calculating the average of the locations of the minimum and maximum values of P_t. This descriptor results in a single value at each location in contrast to the Fourier based phase descriptors. This makes this simplified phase shift more physically intuitive for direct comparison with what can be observed in contour plots of physical properties.

Defining the center of the distorted region in this manner relies on the assumption that the pattern has a clear minimum near the location of the leading edge of the applied sector and a clear maximum near the location of the trailing edge of the applied sector. If the distortion shape differs significantly from this expected pattern, then the phase shift calculated by this simplified method becomes less representative of the true flow field. For this thesis, when multiple local maximums or minimums exist, the extrema closest to the leading and trailing edges of the distorted sector will be used in the calculations.

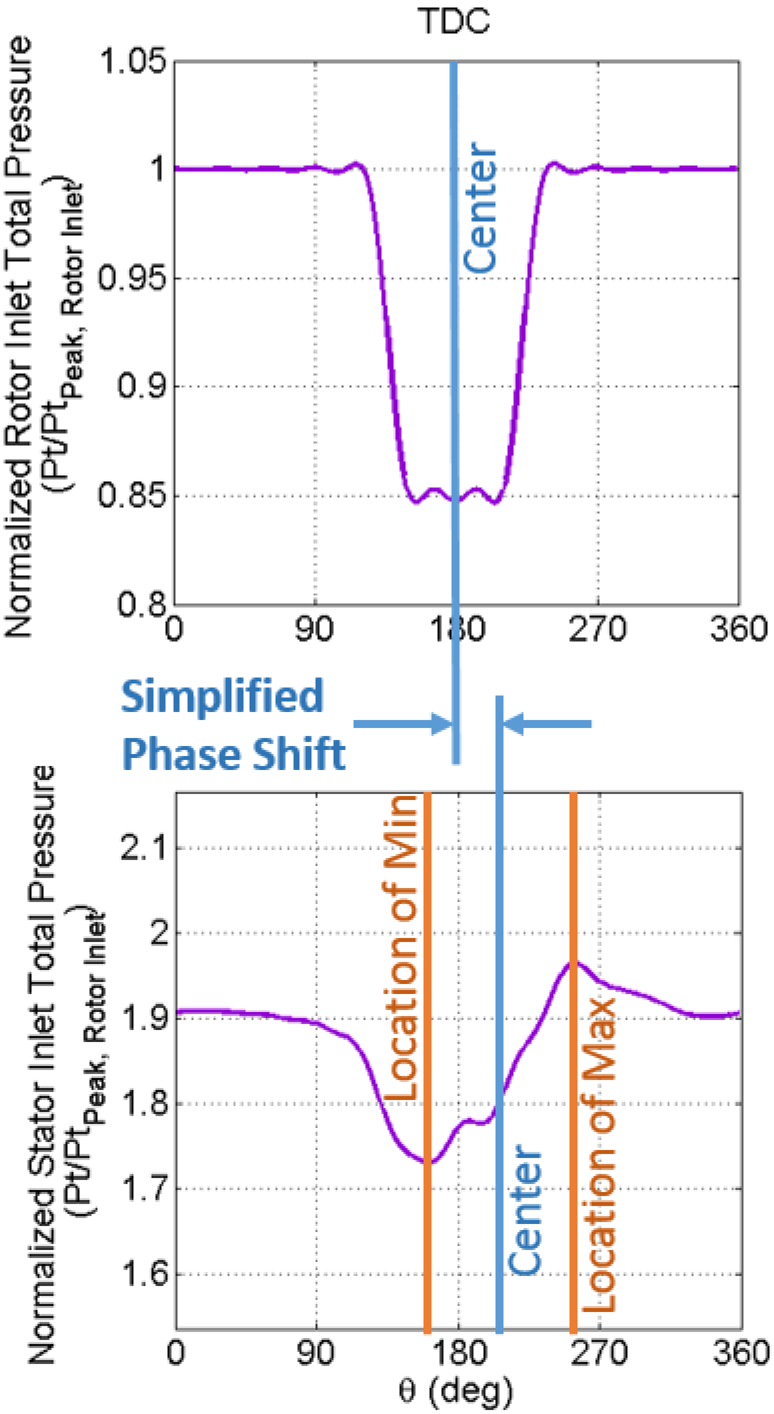

Figure 3.10: Definition of simplified phase shift descriptor.

CHAPTER 4. RESULTS: INLET DISTORTION VARIATION STUDY

This chapter will present results from the study into the impacts gradual changes in inlet distortion shape have on distortion transfer and generation, as overviewed in section 3.1. More specifically, the changes studied are variations in the transition from the distorted sector to the undistorted sector. Results will include an overview of performance parameters, review of pressure and temperature contour plots at the stator inlet, pressure induced swirl comparisons, P_t distortion results, T_t distortion results, and blade loading analysis.

4.1 Overall Performance Measures

To quantify overall performance measures of the fan under each inlet distortion profile, P_t ratio and efficiency were calculated. P_t ratio was calculated between the spinner inlet and the stator outlet, referred to as stations 2 and 3 respectively using equation 4.1. $P_{t,3}$ and $P_{t,2}$ were calculated as a mass flow average at the given station and operating point. Efficiency for the fan was calculated using equation 4.2 with γ calculated at the average temperature across the stage. $T_{t,3}$ and $T_{t,2}$ were also calculated as a mass flow average at the given stations and operating point.

$$PR = P_{t,3}/P_{t,2} \tag{4.1}$$

$$\eta_f = \frac{{\frac{p_{t,3}}{p_{t,2}}}^{\frac{\gamma-1}{\gamma}} - 1}{\frac{T_{t,3}}{T_{t,2}} - 1} \tag{4.2}$$

Values were averaged over an entire blade passage, or 18°, in 1/4° increments to obtain the corrected mass flow, fan pressure ratio and efficiency for 100% corrected speed. Performance measures for each simulation are presented in Table 4.1. The experimental data for Rotor 4 with a clean inlet profile produces a peak efficiency of 89.6% at a mass flow of 27.6 $\frac{kg}{s}$ [4]. Generally, distortion reduces the peak efficiency of the rotor and moves the peak efficiency to a slightly higher mass flow rate, as mentioned in Section 2.2 of this thesis.

The mass flow rate and pressure ratio for the 90 and 135° sectors remained constant for each profile shape. Decreasing the distortion transition abruptness steadily increased the efficiency of the stage by 0.06% for the 90° sectors and 0.08% for the 135° sectors. Therefore we conclude that the abruptness of the distortion transition did not affect the mass flow rate and pressure ratio and had minimal impact on efficiency. The 135° sector operated at a slightly lower mass flow rate with higher pressure ratio suggesting the operating point was a little closer to stall. Simulations of rotor 4 under a similar distortion showed a near-design mass flow of 28.0 $\frac{kg}{s}$ and peak efficiency of 85.2% [3]. The performance parameters in Table 4.1 occur at similar mass flows, pressure ratios, and efficiencies to the near-design performance parameters observed by Soderquist, suggesting that the simulations presented in this thesis are in a near-design operating condition.

Table 4.1: Performance parameters for Rotor 4 under distortion.

	Corrected Mass Flow [kg/s]	Pressure Ratio	Efficiency [%]
90 Base	27.89	1.872	84.64
90 Shape 1	27.89	1.872	84.70
90 Shape 2	27.89	1.872	84.76
135 Base	27.43	1.883	84.58
135 Shape 1	27.44	1.884	84.66
135 Shape 2	27.44	1.884	84.74

4.2 Total Pressure and Total Temperature Contours

To qualitatively investigate the impacts of changes to inlet distortion transition abruptness, contour plots for P_t and T_t were generated at the stator inlet. These contour plots were time-averaged over one complete rotation of the rotor in 1° increments per time step. This time averaging was completed before the study referenced in Section 3.1.5 comparing time averaging intervals was completed and used the full rotation standard as opposed to blade passage time averaging.

To provide a clear comparison between the two variations of the inlet profile and the base profile, the contours for shape 1 and shape 2 profiles are presented as a difference from the base profile. At each location in the contour, the value shown is the result of subtracting the shape 1 or 2 profile from the base profile. In these contours, positive values indicate an increase in value relative to the base profile, while a negative value indicates a decrease relative to the base profile. Contours for P_t are included in Figure 4.1 and contours for T_t are included in Figure 4.2. The rotor was rotating in the clockwise direction when viewed from forward looking aft.

For the 90° base sector in Figure 4.1, several strong circumferential variations in P_t are observed. A region of increased pressure is seen near the hub at approximately 225°. Another region of low pressure is observed at approximately 170°. These regions represent transferred inlet distortion through the rotor and correspond with the edges of the 90° inlet distortion sector. For the 135° base sectors, similar circumferential variations are observed, but at different circumferential extents. The high pressure region near the hub occurs at 270° and the low pressure occurs at 150°. These correspond with the edges of the 135° inlet distortion sector. The circumferential differences observed are a direct result of the difference in distortion extent between the two sector sizes. Other than these circumferential variations, the 90° and 135° sectors do not differ greatly.

For both sectors, the contours for shape 1 and shape 2 vary mostly in magnitude while having a consistent contour shape. The contours for shape 2 show the largest differences relative to the base contour, seen by the darker coloring. Impacts due to inlet distortion transition abruptness, though similar between shape 1 and 2, are most pronounced at shape 2. Therefore, focus is placed on comparisons between the shape 2 and base profile.

Both regions show a reduction in the strength of the pressure variations observed in the base profile. This suggests that a more gradual distortion transition results in pressure distribution that trends towards a uniform distribution. This is clearly observed in the contours for shape 2 P_t at the locations of the regions of high and low pressure. At these locations, strong regions of difference from the base profile are observed in both sectors. At the high pressure region near the hub at 225° observed in the 90° base profile, the shape 2 profile has a region where pressure is decreased relative to the base contour, with a maximum decrease of approximately 2%. Similarly at the low pressure region located at 170° in the 90° base profile, the shape 2 profile has a region where pressure is greater than the base contour by approximately 8%. Similar differences are observed in the 135° sector at the corresponding circumferential locations.

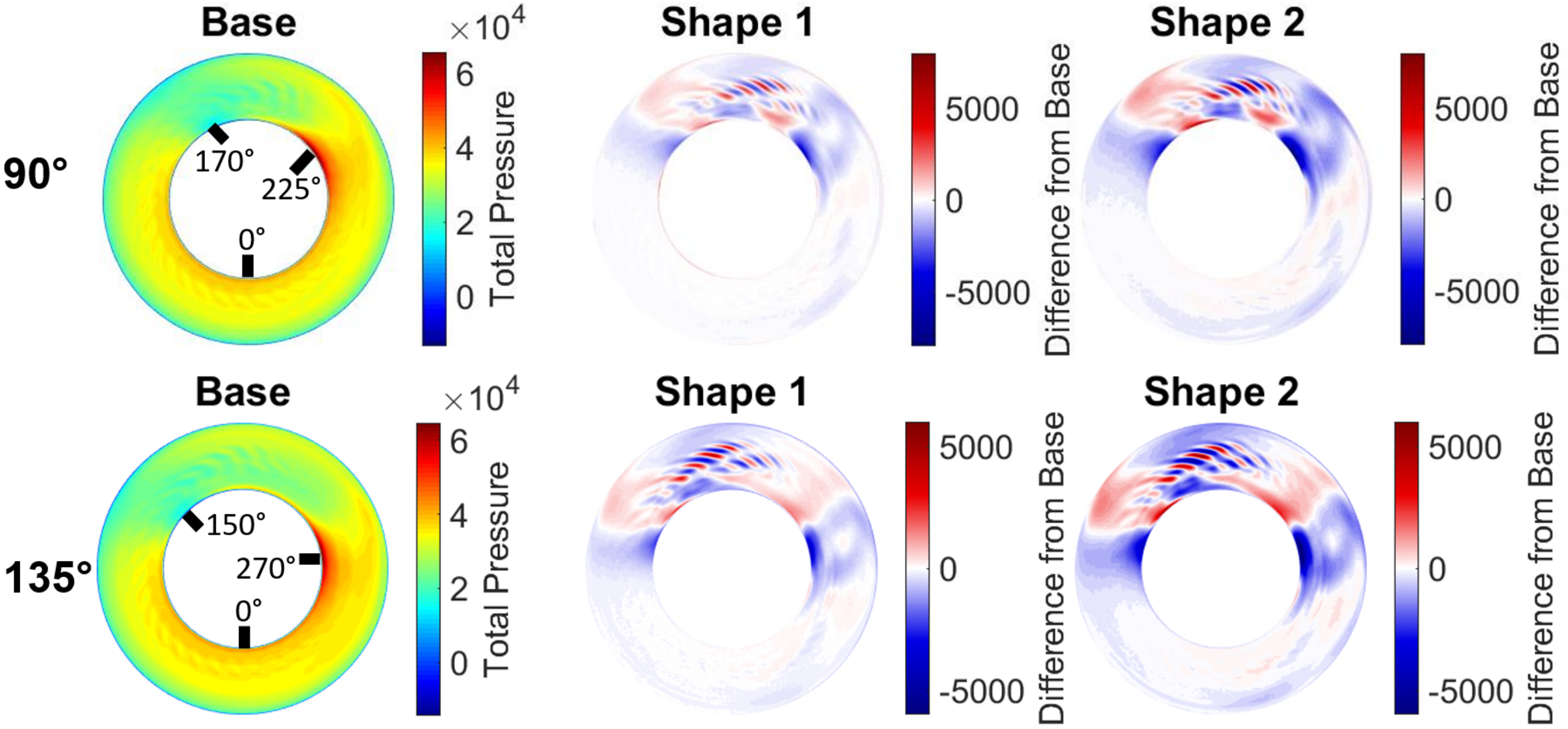

Figure 4.1: P_t at stator inlet (Pa). Shape contours represent the difference from the base contour. View is forward looking aft. Top: 90 ° sector. Bottom: 135 ° sector.

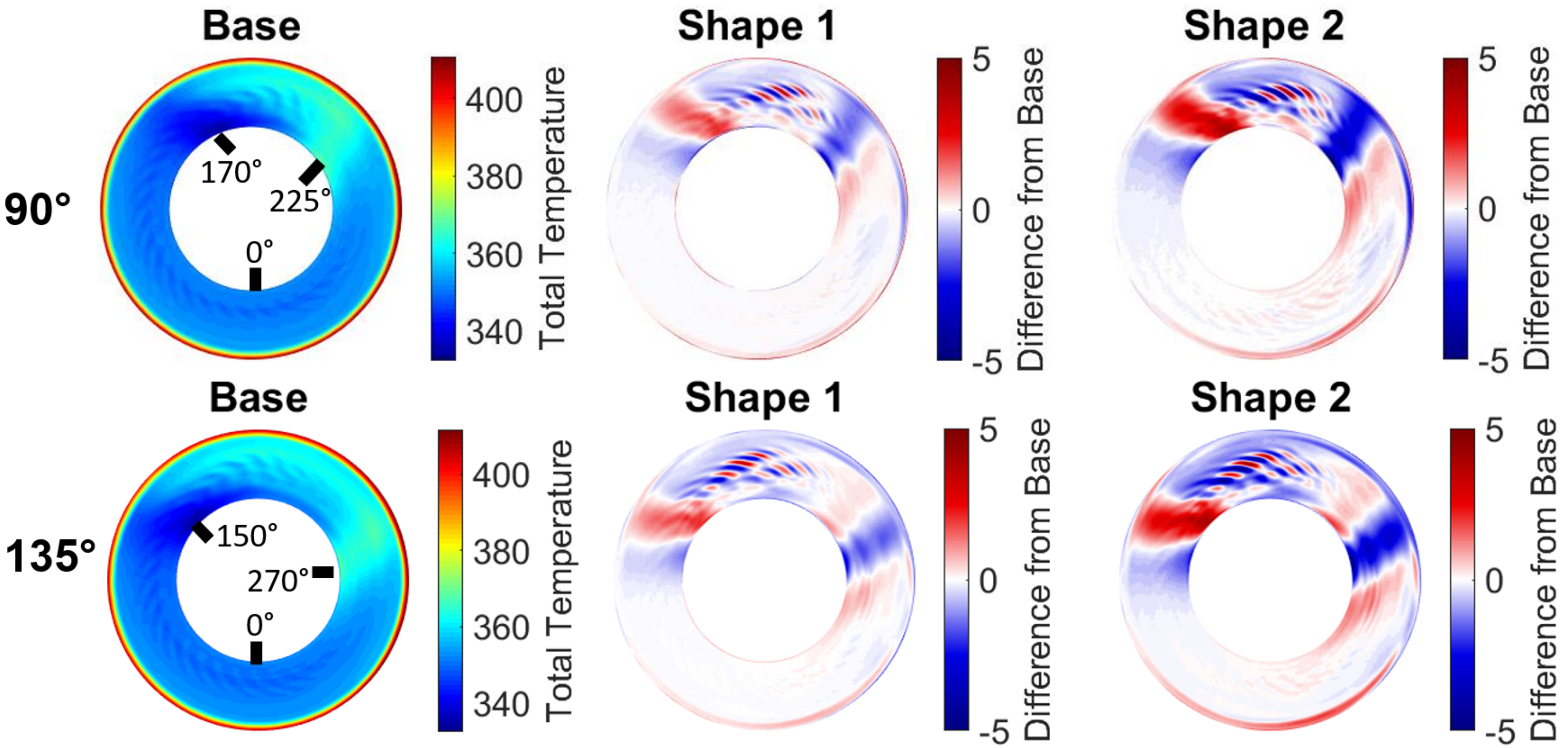

Figure 4.2: T_t at stator inlet (K). Shape contours represent the difference from the base contour. View is forward looking aft. Top: 90 ° sector. Bottom: 135 ° sector.

The 90° base T_t sector in Figure 4.2 shows regions of high and low temperature formed. A high temperature region forms at 225° and a low temperature region forms at 170°. Both are concentrated near the hub but continue radially towards the casing. These regions represent distortion generated as a result of the P_t distortion. The 135° sector shows similar behavior, but with the high temperature regions located at 270° and the low temperature region located at 150°. The differences in circumferential location of these regions is due to the difference in distortion extent between the 90° and 135° sectors.

Compared to the base contour the shape 2 profile shows a decrease relative to the base in regions where T_t is elevated in the base profile and increases in regions where T_t is reduced in the base profile. As with the observations for the P_t contours, this suggests the gradual transition of shape 2 results in a more uniform temperature distribution at the stator inlet. For the 90° shape 2 sector the high temperature region at 225° decreases by approximately 1.5% relative to the base and the low temperature region at 170° increases by 1.2% relative to base.

4.3 Pressure Induced Swirl

Induced swirl is key to understanding distortion transfer and generation, and is defined in Figure 2.1 as a measure of tangential flow angle. Induced swirl at the rotor inlet for the 90° distortion sector is plotted in Figure 4.3 and similar plots for the 135° sector are shown in Figure 4.4. A traverse for swirl is shown at each of the 5 radial locations used in this study. Understanding the impacts of inlet distortion transition abruptness on induced swirl can help predict the impacts on other properties, since induced swirl is closely connected to local power variations, as observed by Soderquist [3].

At the location where the blades enter the distorted sector, the swirl is in the same direction as the blade rotation (co-swirl). At the location where the blades exit the distorted sector, there is counter-swirl. Regions of co- and counter-swirl develop at 135° and 225° in the 90° sector. These regions correspond to the edges of the inlet distortion profiles, where pressure transitions from low to high pressure (Fig. 3.3). Similar co- and counter-swirl develops in the 135° sector as well, at approximately 120° and 270°. Since the variations made to the inlet pressure profiles were in these transition regions, we expect changes in induced swirl to occur at similar circumferential locations. Counter-swirl increases the rotor incidence angle and co-swirl decreases the rotor incidence angle.

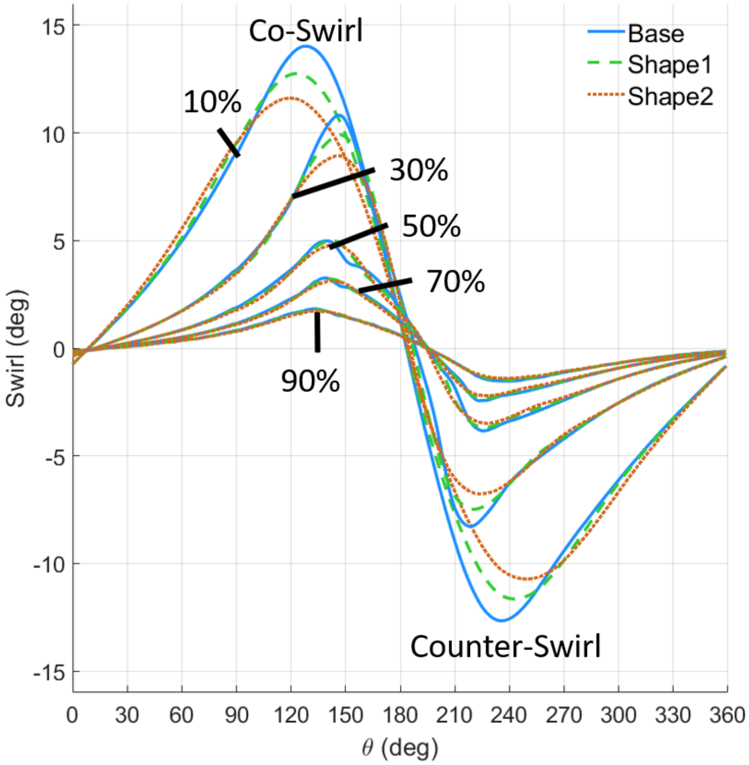

Figure 4.3: Induced swirl at the rotor inlet for 5 radial locations for the 90° sector.

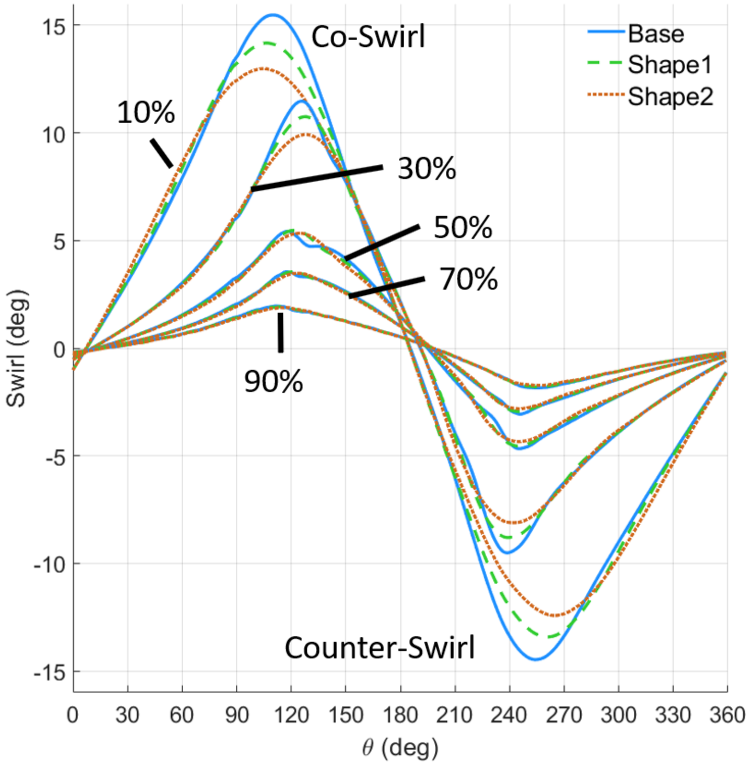

Figure 4.4: Induced swirl at the rotor inlet for 5 radial locations for the 135° sector.

Increased incidence corresponds to higher blade loading and decreased incidence corresponds to lower blade loading.

Several differences are observed when comparing the 90° and 135° sector base swirl. The first is the difference in location of co- and counter-swirl mentioned in the previous paragraph. Co- and counter-swirl occur at 135° and 225° respectively for the 90° sector. Similar regions occur at 120° and 270 ° for the 135° sector. However, the magnitude of these regions are greater than those observed for the 90° sector by approximately 1° (7%) at the maximum co-swirl and 2° (16%) at the maximum counter-swirl. This would suggest that although the percent distortion is the same for both sectors, the 135° sector will likely experience increased power variations and slightly elevated levels of distortion transfer and generation. This increase in distortion content is confirmed by the data presented in Section 4.5. For both sectors, swirl decreases as span increases.

Several observations are made by comparing the swirl at the base profile to the swirl at shapes 1 and 2. As the inlet distortion transition becomes more gradual moving toward shape 2, a decrease in the magnitude of co- and counter-swirl is observed. For the 90° sector at 10% span in the co-swirl region, the swirl is approximately 3° less in shape 2 than the base. This difference decreases moving towards larger spans, becoming near zero at spans above 50%. A similar difference is observed in the counter-swirl region. This suggests that by making the inlet distortion transition less abrupt, less swirl is induced near the hub, with little change in induced swirl at higher spans. Since co- and counter- swirl are primarily responsible for local power variations in the rotor, decreasing their magnitude should result in lower power variations and thus less distortion transfer and generation. This will be further explored in Section 4.5. At 50%, 70%, and 90% span the swirl profiles are nearly identical suggesting induced swirl at those spans was not affected by the inlet profile shape.

4.4 Entropy

Evaluating entropy helps identify and describe loss in a flow field. High entropy equates to higher levels of loss, as found in boundary layers, shocks, separation, and turbulence. Lower entropy is associated with higher efficiencies. Entropy is plotted for each distortion profile to explore differences between the three profiles. Time accurate data in this section was calculated over one blade passage, or 18° , in time steps equal to 1° per time step. Thus far, entropy data is only available for the 90° sector but work is being done to obtain the entropy data for the 135° sector.

To better compare the impacts caused by the variations in the inlet profile, the contours for shape 1 and shape 2 are presented as a difference from the base profile. Positive values indicate an increase in entropy relative to the base profile, and a negative value indicates a decrease in entropy relative to the base profile.

Entropy at the rotor inlet is shown in Figure 4.5. The base entropy contour reveals that the applied distortion results in a corresponding region of increased entropy centered at top dead center. The adjustments made to the distortion transition abruptness in shape 1 and 2 modify this high entropy region, as seen in the shape 1 and shape 2 contours. Both exhibit a decrease in entropy inside the distortion and an increase in entropy outside the distortion as distortion transition abruptness becomes more gradual. The shape 2 contour shows the stronger increases and decreases in entropy relative to shape 1.

This behavior appears to be closely connected to the changes made to the total pressure profile transition abruptness, which were presented in Figure 3.3. When transitioning from the undistorted region into the distorted sector, the beginning of the transition is characterized by a region where total pressure is decreased for shape 1 and 2 relative to base. This corresponds with the increases in entropy observed at the beginning of the transition in Figure 4.5. At the end of the transition, total pressure is increased in shape 1 and 2 relative to base. This corresponds to a decrease in entropy observed in Figure 4.5. The redistribution of total pressure which occurs as the transition is made less abrupt corresponds to a similar redistribution in entropy.

Total entropy was calculated by integrating the entropy over the radius and circumference of the contour. At the rotor inlet, the shape 1 contour increases in entropy by 0.07% relative to base, while the shape 2 total entropy increased by 0.19%. Shape 2's increase is almost 3 times that of shape 1. These increases in entropy are minimal and do not have a significant impact on performance, but show that entropy is increased as the distortion transition abruptness is made less gradual. Intuitively, we expect higher entropy flows to result in lower efficiencies. In the case of the shape 2 flow however, we observe a slight increase in entropy along side an increase in efficiency as observed in Section 4.1. This discrepancy could be the result of the shape 2 distortion having a

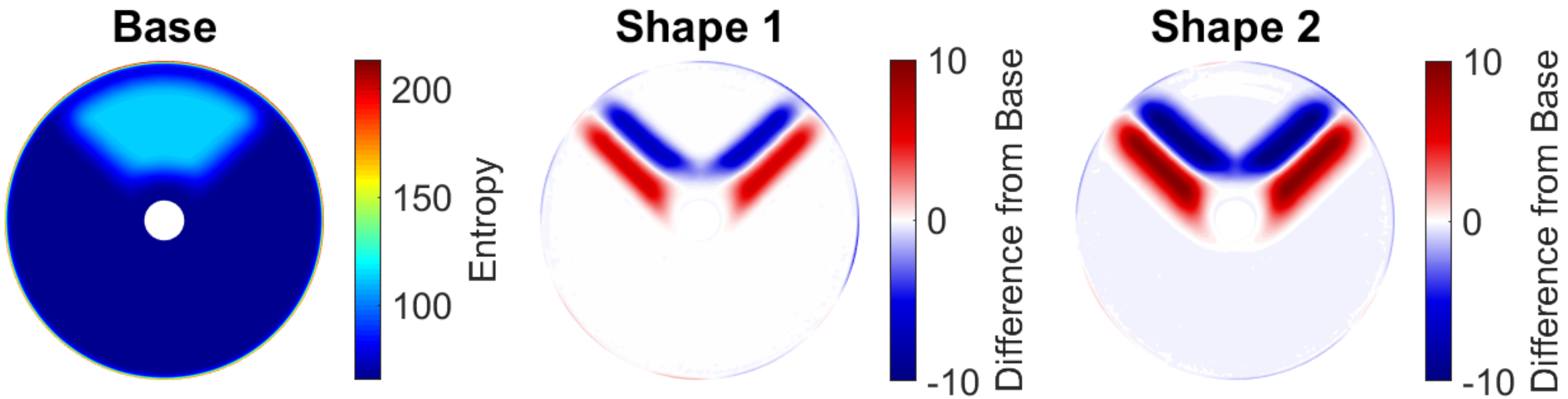

Figure 4.5: Entropy at the rotor inlet. Shape contours represent the difference relative from base contour. View is forward looking aft.

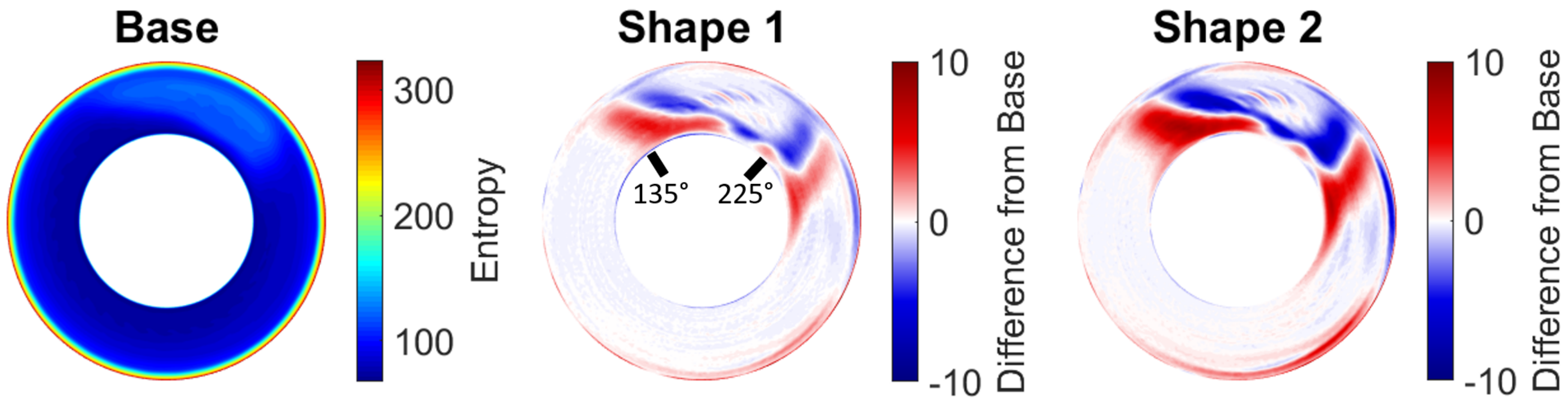

Figure 4.6: Entropy at the stator inlet. Shape contours represent the difference relative from base contour. View is forward looking aft.

slightly higher average total pressure relative to the base distortion, which would result in a slight increase in efficiency.

Entropy at the stator inlet is shown in Figure 4.6. The base entropy contour shows that the high entropy region observed at the rotor inlet has transferred downstream and has shifted clockwise circumferentially. A similar circumferential shift was observed in the pressure contours for P_t in Figure 4.1. Shape 1 and shape 2 still exhibit lower entropy regions relative to the base profile on the inside of the distortion sector and increased entropy relative to the base profile at the outside edges of the distortion sector. The contours for shape 1 and 2 are similar in shape, with shape 2 having larger magnitudes of difference relative to the base contour.

The contour shape observed in the shape 1 and shape 2 contours reflects how the distortion has changed while passing through the rotor. The white region separating the high and low entropy regions represents the center of the distortion transition region, and could in a future work be used to help describe how a distortion profile changes shape and translates through a rotor. It's clear presence in both the rotor inlet and stator inlet contours would make such a study possible.

Total entropy at the stator inlet was also calculated for each profile and compared. The shape 2 entropy increased by 0.20% relative to the base entropy, while the shape 2 entropy increased by 0.40% relative to the base entropy. Shape 2 entropy increase is double that of shape 1. This relative difference is less that was observed at the rotor inlet, where shape 2 has 3 times the entropy difference of shape 1. This could be interpreted in two ways. One would be that shape 1 experiences increased loss relative to shape 2 thus closing the relative difference in total entropy from 3 times to 2 times. The other potential interpretation is that the shape 2 profile results in less loss across the rotor relative to shape 1, again resulting in a decrease in relative difference in total entropy from 3 times to 2 times.

While time averaged contours are useful in visualizing the constant flow field elements, time accurate data can reveal insights into where flow elements such as shocks, boundary layers, or flow separation impact the flow. As such, comparing time accurate flow fields is beneficial. Time accurate contours of entropy at the stator inlet for the three inlet profiles are shown in Figure 4.7. These time accurate contours were recorded at a single instance in time when the rotor position was the same between all three simulations. Future work could expand this study by considering additional instances in time and explore variations in flow with respect to time.

The same regions of increased and decreased entropy at the edges of the distortion profile are seen in the time accurate contours. However, blade wakes are now visible, and these help identify some unique differences in flow. Two blades in particular are highlighted in Figure 4.7, one circled in green and one in red. The same blade is circled in both the shape 1 and shape 2 contours for comparison.

Overall, the shape 2 contour is the same as the shape 1 contour, but with increased magnitude. Differences relative to base are exaggerated in the shape 2 contour with a few exceptions which will be explored in detail. One key flow feature to note are the blade wakes, which are represented as high entropy regions spanning from hub to tip in the base contour. In the shape 1 and 2 contours, variations in the wake are observed as repeating red and blue regions which span from hub to tip at regular intervals around the circumference. These regular variations may suggest that the wakes have moved relative to the base contour. Further investigation is needed to confirm this observation. This thesis will proceed by exploring some variations noted in the blade wakes, though after future investigation, these may be shown to be connected to blade wake movement rather than changes due to distortion.

The blade wake circled in green is located at the region of counter-swirl indicated in Figure 4.3. Shape 1 has a region of higher relative entropy to base in this region, observed as a red stripe spanning from the hub to the tip. This corresponds to the pressure side of the blade where pressure is increased. In the same location in the shape 2 profile, this higher entropy region is not observed.

At the blade location circled in red, similar behavior is observed, but with the suction surface of the blade, indicated by the blue region of decreased entropy. In the shape 1 contour, the wake off the suction surface of the blade is clearly seen, observed as a blue line spanning from the hub to casing. This blue region of decreased entropy is less prominent in the shape 2 contour, suggesting an increase in entropy over the suction surface between shape 1 and 2 in this region. This occurs when the blade is in the co-swirl region indicated in Figure 4.3.

Combined, these observations suggest that in the regions of co- and counter-swirl, flow over the suction and pressure surfaces of the blade are altered as the inlet distortion transition abruptness changes. To better evaluate how this flow might be changing, time accurate entropy

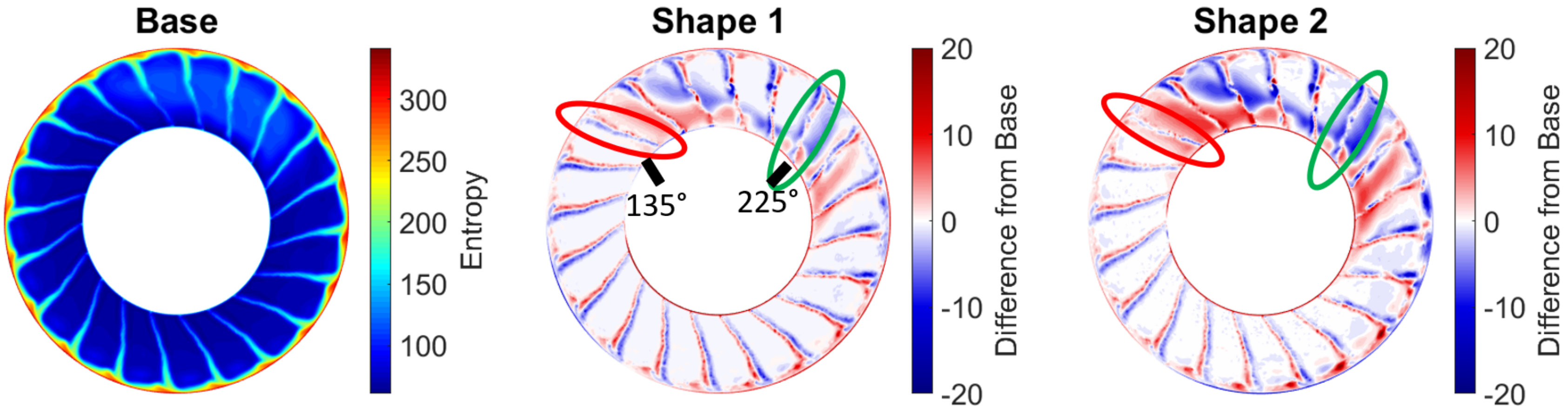

Figure 4.7: Instantaneous snapshot of entropy at the stator inlet with several blade locations identified for comparison. View is forward looking aft.

through blade passages at 50% span are presented at each location for the base and shape 2 inlet cases.

These blade passage views are provided in Figure 4.8 for the region of counter-swirl and in Figure 4.9 for the region of co-swirl. Contours are provided in both figures for the base inlet case and the shape 2 inlet case. These contours reveal bow shocks at the leading edge of the blades, passage shocks in the blade passages, and show boundary layer growth along the blades.

A close comparison of Figure 4.8a and Figure 4.8b reveals some slight variations in the region of counter-swirl near 225°. The most prominent is circled in red, and highlights a difference in bow shocks between the two inlet cases. The bow shock in the shape 2 contour has a lower entropy behind the shock. Lower entropy behind a shock is an indicator of a weaker shock wave. This suggests that as the blade enters the region of counter swirl at the edge of the distorted region at approximately 200° in the shape 2 case, the bow shock is weaker than in the base case. A weaker shock would result in lower P_t behind the shock, which is observed at 225° in the contours shown in Figure 4.1.

The bow shock strength was calculated at this location to confirm this observation and used Equation 4.3 which compares static pressure before (P_1) and after (P_2) a shockwave. The bow shock observed in the base simulation was calculated to have a strength of 0.742 and the bow shock at the same location in the shape 2 simulation was found to have a strength of 0.700, putting the shape 2 bow shock at approximately 5% weaker relative to the base bow shock.

$$ShockStrength = \frac{P_2 - P_1}{P_1} \tag{4.3}$$

Comparing the blade passage contours shown in Figure 4.9a and Figure 4.9b highlight several variations in the region of co-swirl around 135°. Two variations are circled, one in red and the other in black. Variations in bow shocks are observed in the regions circled in red. The shape 2 bow shock is less prominent than the shock observed in the base contour. This suggests that the shape 2 shock in this location is weaker than the corresponding shock in the base contour. This observation was confirmed by comparing bow shock strength using Equation 4.3. The bow shock of the base simulation was found to have shock strength of 0.461 and the bow shock of the shape 2 simulation was found to have a shock strength of 0.427, which is 7% weaker than the

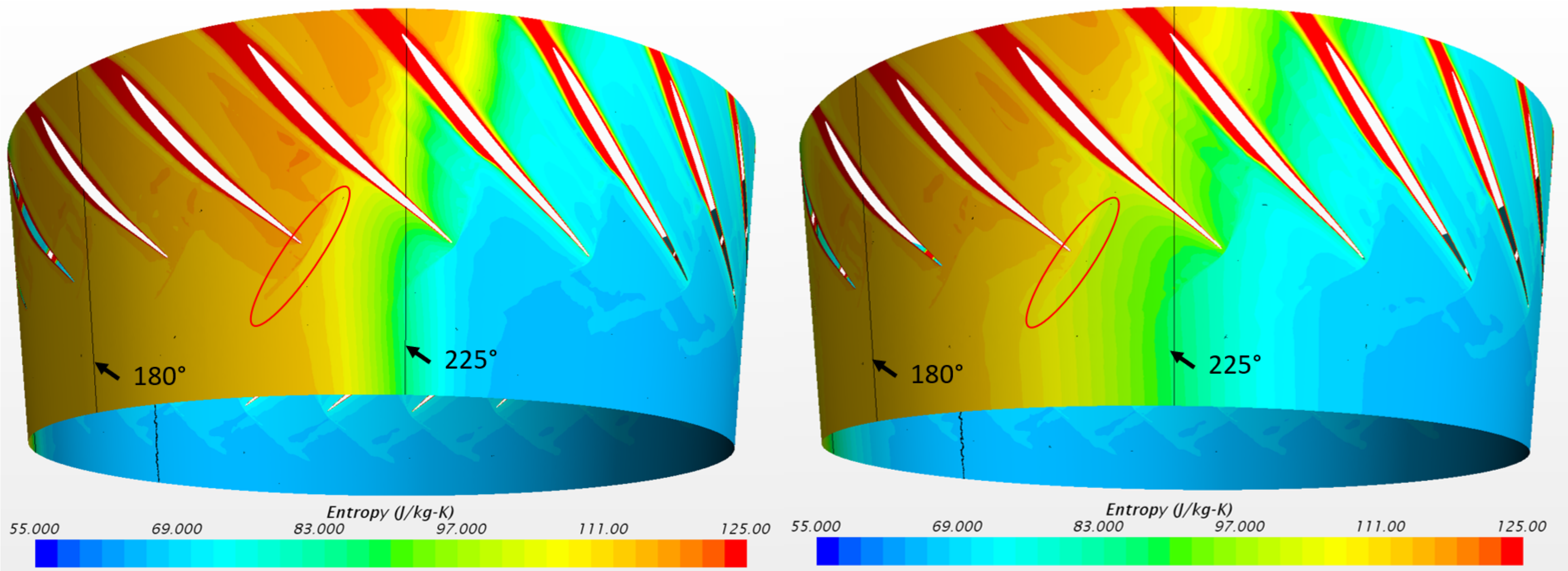

(a) Base

(b) Shape 2

Figure 4.8: Entropy through blade passages in region of counter-swirl at 50% span. Rotor moves from left to right in this view with flow direction being from bottom of the figure to the top.

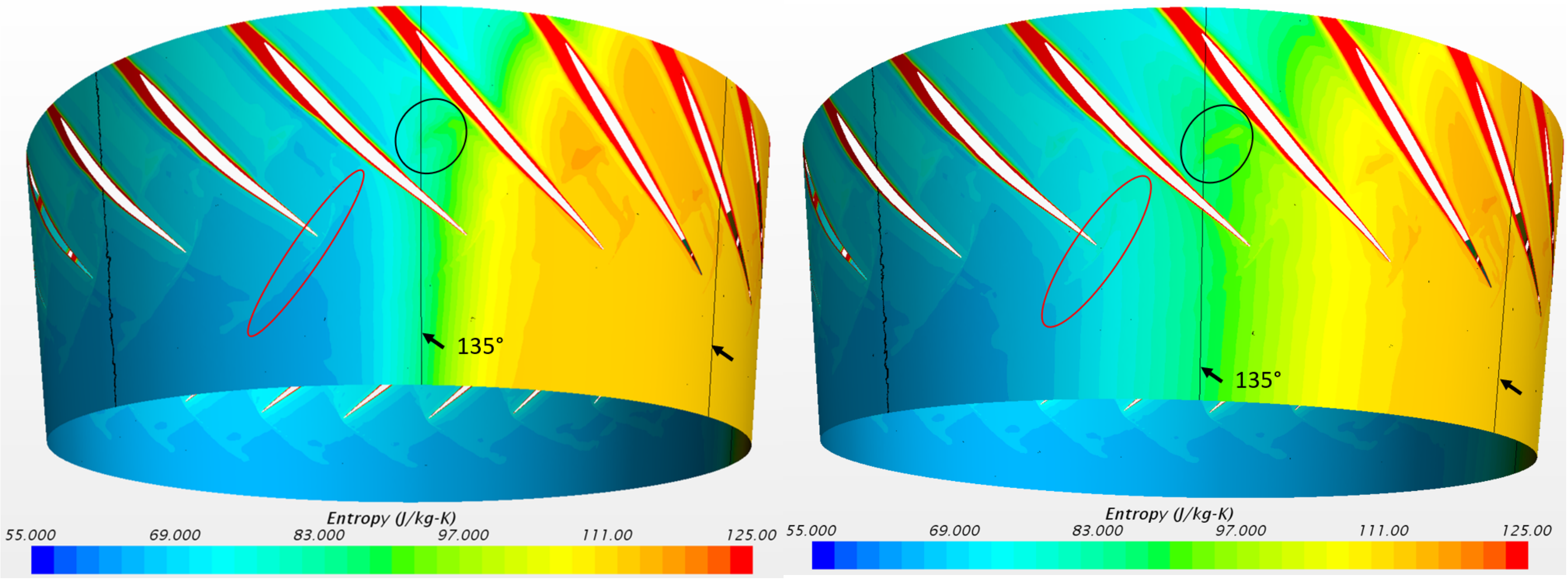

(a) Base

(b) Shape 2

Figure 4.9: Entropy through blade passages in region of co-swirl at 50% span. Rotor moves from left to right in this view with flow direction being from bottom of the figure to the top.

shock in the base simulation. Similar changes in bow shock were observed in a work by Weston when comparing flow through a multi-stage fan in the distorted flow region to undistorted flow region [10].

The second variation in this region is circled in black and is a variation in a passage shock between the two contours. In the region circled, the shape 2 profile has higher levels of entropy, which indicate a stronger shock relative to the base contour. This suggests that pressure behind the shape 2 shock would be higher, which is confirmed by the high pressure region observed near 170° in Figure 4.1.

The variations revealed by the entropy through the blade passages suggest that varying the inlet distortion transition abruptness has an impact on the blade shockwaves as they enter and exit the distorted region. Changes in shock strength were related to corresponding rises and decreases in P_t. A deeper investigation into the shockwaves in these regions, including further quantification of shockwave movements and changes in shockwave strength would reveal additional insights which would help explain the changes observed between the inlet cases.

4.5 Total Pressure Distortion

Circumferential traverses of time-averaged P_t at the stator inlet for the five radial locations are shown in Figure 4.10 for the 90° sector and Figure 4.11 for the 135° sector. These traverses are reconstructions of the simulated pressure data using 12 modes of a Fourier transform on the raw data. Using a 12 mode Fourier reconstruction was shown by Peterson [9] to accurately match the distortion profile and also filter out blade row perturbations.

The two sectors exhibit similar pressure traverse shape at spans below 50%, though with the 135° sector profiles having more circumferential span between low and high pressures due to the larger distortion extent of the 135° sector. At spans above 50%, the 135° traverses show a brief plateau in pressure around 180°, which corresponds to the center of the distortion sector. This plateau is not observed in the corresponding 90° sector traverses. This plateau is likely a result of the larger circumferential extent of the 135° sector and represents a region where flow has equalized at the lower distorted pressure.

In the 90° sector, the largest variations between traverses for different distortion shapes are observed at 10% span at approximately 230° and 155°. These locations correspond to the minimum

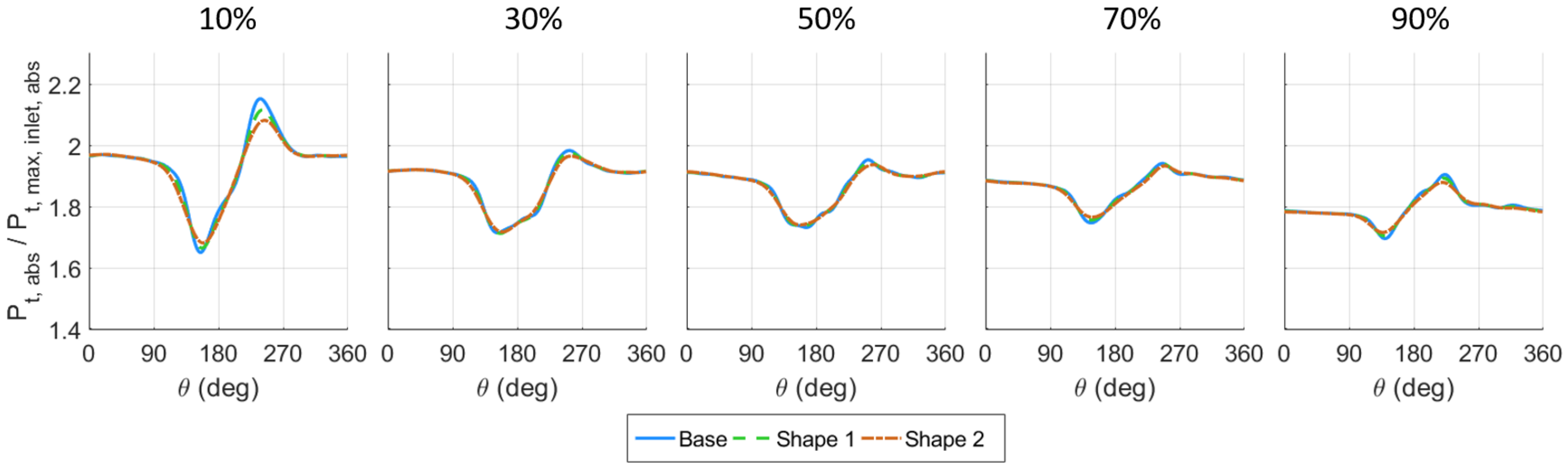

Figure 4.10: Fourier-reconstructed traverses for P_t at stator inlet for the 90° sector.

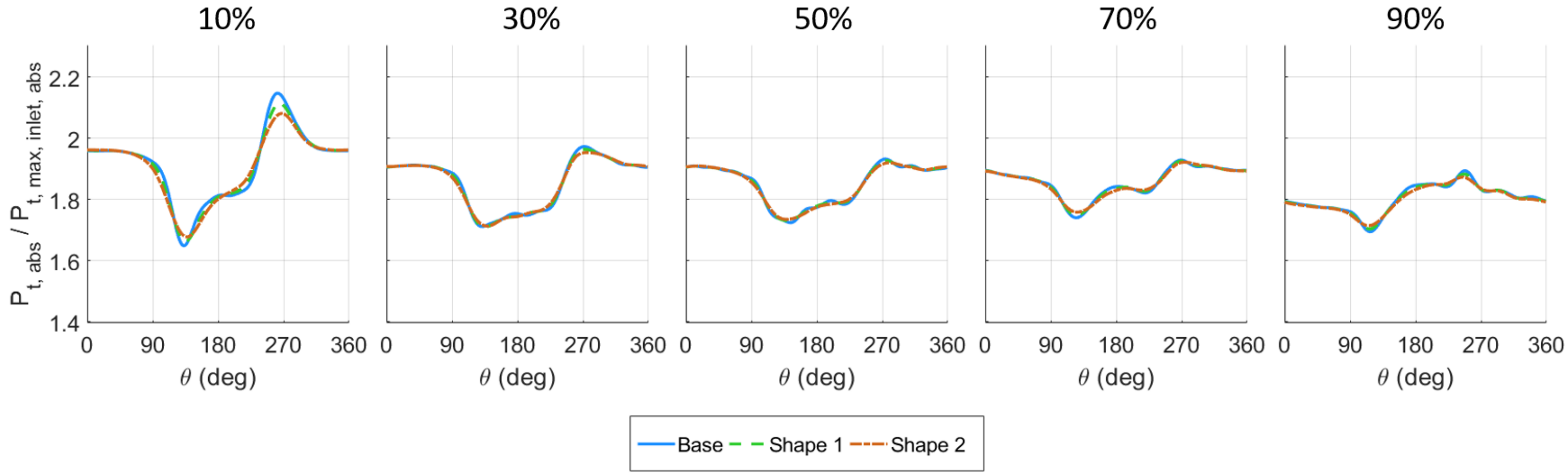

Figure 4.11: Fourier-reconstructed traverses for P_t at stator inlet for the 135° sector.

and maximum P_t associated with the transition in the distortion sector from high to low P_t and low to high P_t. At the location of maximum pressure, the difference between base and shape 2 is approximately 3%. A 2% difference is observed at the location of minimum pressure. Variations at the peak decrease from 1% at 30% span to 0.4% at 70% span. The difference increases to 1% again at 90% span. At the minimum pressure, pressure increases start at 0.5% at 30% span and climb to 1% at 90% span. At other circumferential locations for each span, the traverses for each inlet case generally differ by less than 0.5%. Similar behavior is observed in the 135° sector and differences between base and shape 2 have similar percentages. The circumferential location of the peaks and valleys changes for the 135° sector to 260° and 130°.

The circumferential locations of the peaks and valleys in traverses corresponds to the location of the co- and counter-swirl identified in Figures 4.3, 4.4 and the locations where variations were made to the inlet distortion transition abruptness. As the largest variations in P_t traverses were observed when comparing the shape 2 results with the base results near the hub, it can be concluded that by making the inlet distortion transition less abrupt, less pressure variation will exist after passing through the rotor. This suggests that distortion levels will be lower in the shape 2 simulations than in the base simulations.

In order to further validate the conclusion that making the inlet distortion transition less abrupt will result in lower levels of pressure distortion after passing through the rotor, the P_t amplitudes were calculated at the stator inlet and are shown in Figure 4.12 for the 90° sector and Figure 4.13 for the 135° sector. These amplitudes are an overall distortion metric which measure the P_t distortion at the stator inlet, and give insight into the distortion transfer which occurs through the rotor. Higher amplitudes represent high distortion levels and low amplitudes correspond to lower distortion levels. The amplitudes are normalized by the maximum P_t at the inlet.

Comparing the total amplitude between each sector's base case, we observe that the 135° sector has slightly larger total amplitude at 10% and 30% span. Overall however, there is little difference between the magnitudes of distortion amplitude for the 90° and 135° sectors. In both cases, total amplitude decreases at similar rates moving towards 70% span, with 90% span having slightly elevated levels of total amplitude than 70% span. This is likely a result of the tip clearance flow, which is known to be highly turbulent and introduces additional distortion into the flow.

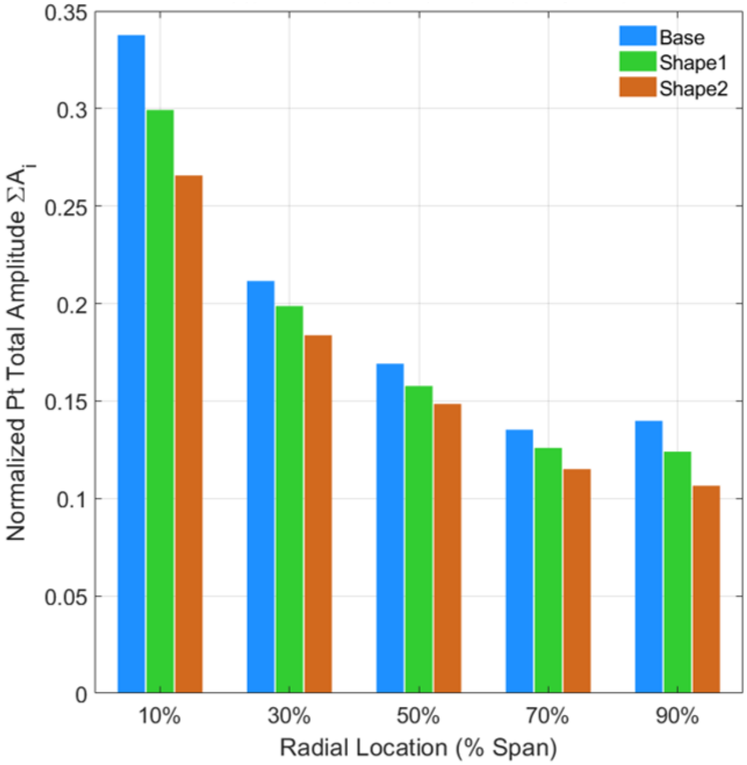

Figure 4.12: P_t Fourier total amplitudes at stator inlet for 90° sector.

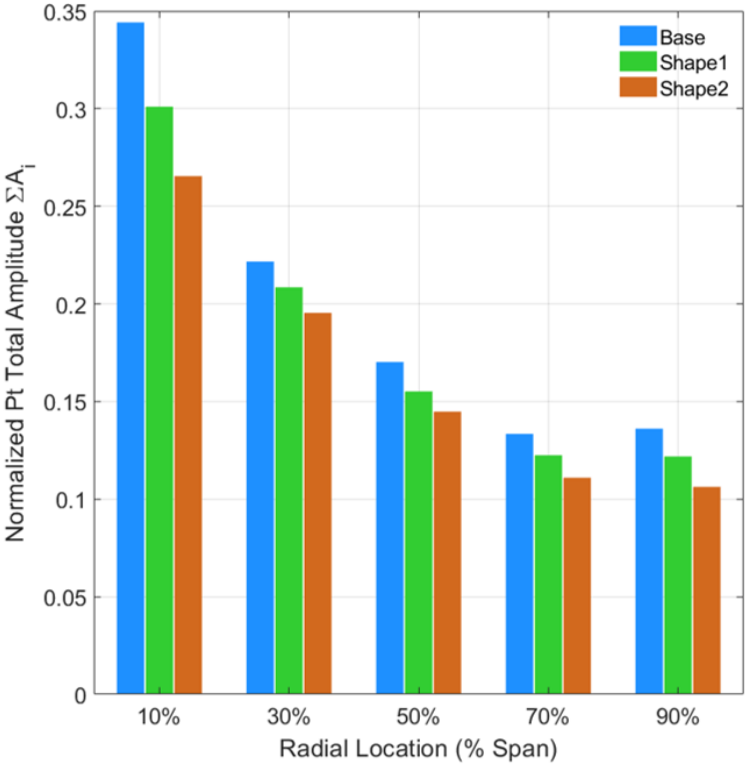

Figure 4.13: P_t Fourier total amplitudes at stator inlet for 135° sector.

For both sectors, P_t amplitude decreases between the base and shape 1, with an additional decrease between shape 1 and shape 2. This supports the conclusion that as inlet distortion transition abruptness becomes more gradual, resulting distortion transfer levels decrease. For the 90° sector at 10% span, the decrease in distortion amplitude between the base and shape 2 is approximately 21%. For the spans ranging from 30% to 70%, the decrease is relatively steady, at approximately 14%. This difference increases again near the casing, with a decrease of approximately 24%.

Similar behavior is observed in the 135° sector, with a 23% difference at 10% span, 15% difference for spans from 30% to 70%, and 22% at the 90% span. The largest decreases in P_t amplitude occur at the base and tip of the blades, suggesting that the greatest reductions in distortion transfer due to changes in inlet distortion transition abruptness occur at these radial locations.

The minimal differences in total amplitude between sectors and consistent differences between shapes within a sector lead to the conclusion that the distortion transition abruptness has a larger impact on distortion levels than extent of the distortion.

4.6 Total Temperature Distortion

Circumferential traverses of time-averaged T_t at the stator inlet for the five radial locations are shown in Figure 4.14 for the 90° sector and Figure 4.15 for the 135° sector. T_t distortion is generated as a result of the P_t distortion passing through the rotor. As with the pressure traverses, these traverses are reconstructions of the simulated pressure data using 12 modes of a Fourier transform.

The two sectors have similar traverse shapes and magnitudes for the base case, again with the 135° sector traverses having larger circumferential extent between the maximum and minimum T_t. However, the plateau observed near 180° in the P_t traverses at spans above 50% is observed to occur starting at 10% span in the 135° sector and continues through 70% span. This suggests that due to the larger extent of the 135° sector, a flow equilibrium is achieved within the distorted region.

In the 90° sector, variations are seen between the three profiles at approximately 150° and 225°. The largest variations occur at the 10% span between the base and shape 2 traverses, with an apparent decrease in magnitude moving toward larger percent spans. Variations are concentrated

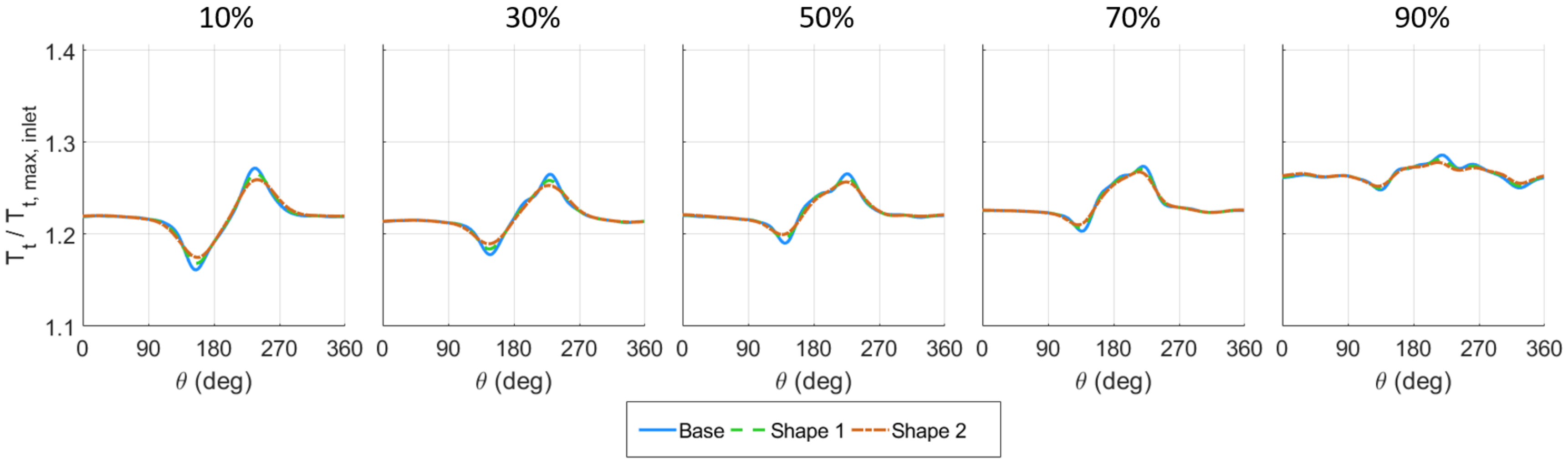

Figure 4.14: Fourier-reconstructed traverses for T_t at stator inlet for the 90° sector.

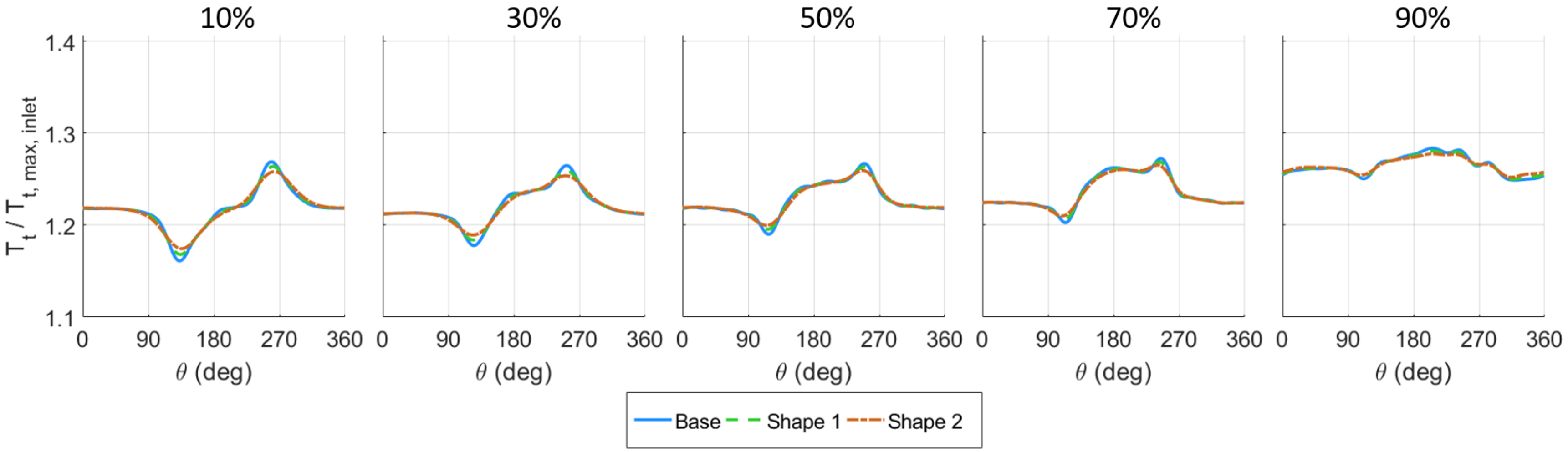

Figure 4.15: Fourier-reconstructed traverses for T_t at stator inlet for the 135° sector.

at the maximum and minimum values of the traverses, with a difference of approximately 1% at both locations for the 10% span. The difference remains at 1% to the 50% span, where it then decreases to approximately 0.3% at the 90% span. This holds true for both peaks and valleys.

As with the pressure traverses in Figures 4.10 and 4.11, at other circumferential locations the traverses match closely. The 90% span traverse differs from the others, and does not exhibit the same strong peak and valley behavior. Rather, it remains more uniform at a higher initial T_t. Similar behavior is seen for the 135° sector with a 1% difference from 10% span to 50% span, followed by a decrease to 0.3% at 90% span. For the 135° sector, traverse maximum values occur at 250° and minimum values occur at 130°. This is due to the tip clearance flow, which uniformly generates distortion as flow interacts with the tip of the blade passing the casing.

The circumferential locations of the peaks and valleys observed again correspond to the locations of the co- and counter-swirl identified in Figures 4.3 and 4.4. They also correspond to the locations where variations were made to distortion transition abruptness. As with P_t, a less abrupt inlet distortion transition corresponds to lower T_t variations at the rotor exit. Since this is the case, we conclude that altering the abruptness of the inlet distortion transition reduces the amount of distortion generated through the rotor.

To quantify the decrease in distortion generation as inlet distortion transition is made less abrupt, T_t total amplitudes were calculated at the stator inlet. Plots of these amplitudes compared for each of the inlet cases are included in Figure 4.16 for the 90° sector and Figure 4.17 for the 135° sector. Total amplitudes are an overall distortion metric which measures T_t distortion generated through the rotor as a result of the applied inlet distortion. Higher amplitudes represent high distortion levels and low amplitudes correspond to lower distortion levels. These amplitudes are normalized by the maximum T_t at the inlet.

The base total amplitudes for two distortion sectors are largely similar, with some minor differences. At 10% span, the 135% sector has a slightly decreased total amplitude, which would suggest less distortion generation. The total amplitude matches well for 30%, 70%, and 90% span. At 50% span, the 135° sector has a larger total amplitude, suggesting increased distortion generation.

For both sectors, T_t amplitude decreases between the base and shape 1, with additional decrease between shape 1 and shape 2. This indicates that by making the inlet distortion transition

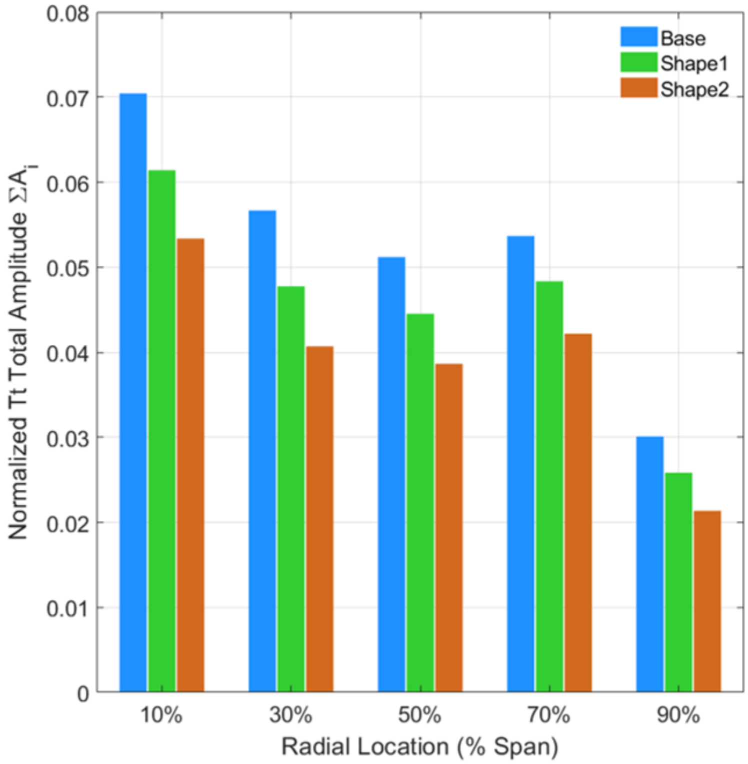

Figure 4.16: T_t Fourier total amplitudes at stator inlet for 90° sector.

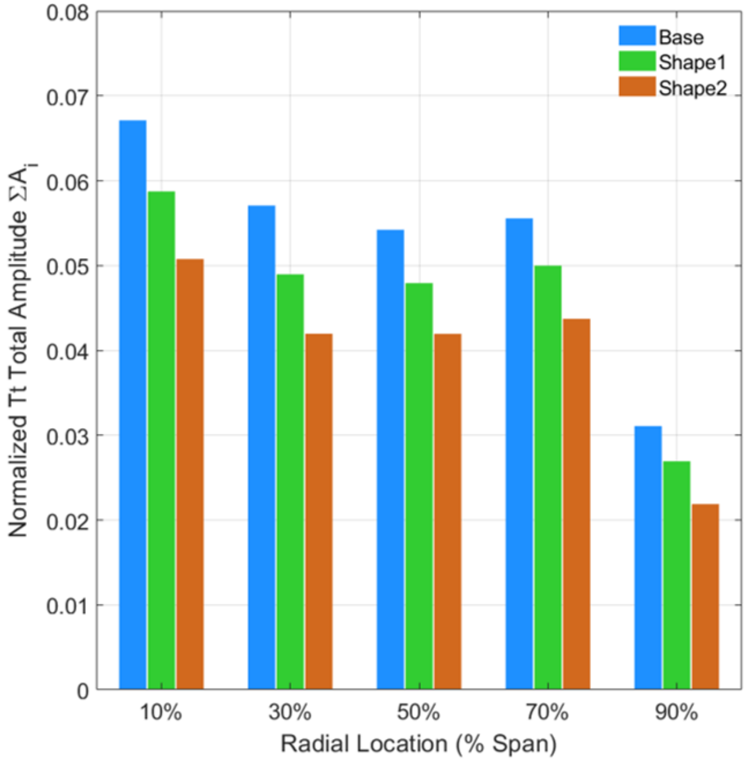

Figure 4.17: T_t Fourier total amplitudes at stator inlet for 135° sector.

less abrupt, there is a decrease in T_t distortion generated through the rotor. For the 90° sector, this decrease is approximately 24% at the 10% span. The decrease rises to 28% at the 30% span and then steadily decreases to 21% at the 70% span. It jumps to 29% at the 90% span. A similar trend is observed in the 135° sector with similar values for percent decrease at each span. A 24% decrease is observed at 10% span, 26% difference at 30% span with a decrease to 21% at 70% span, and 30% difference at 90% span. The highest percent decreases in T_t amplitude occur at the 90% span, which could be a result in decreased distortion generation or variations in tip clearance flow.

4.7 Local Power Variations

Using the blade loading methodology presented in Section 3.1.6, local power variations in the rotor were calculated for each simulation at an instant in time. Circumferential traverses of blade power are shown in Figure 4.18 for the 90° sector and Figure 4.19 for the 135° sector. The traverses are largely similar between the two sectors, with 135° traverses again having larger circumferential extent between the maximum and minimum.

As with the traverses of swirl, P_t, and T_t, the largest variations in power between inlet profile cases are observed at the local extrema of the curves for the base and shape 2 cases. For the 90° sector, the maximum power variation occurs at approximately 225° and the minimum occurs at approximately 150°. In the 90° sector, the maximum power difference between the base and shape 2 cases occurs at 10% span of approximately 11% (1kW). The difference between base and shape 2 drops to 5% for 30% span, additionally decreases to 4% for 50% span, and then climbs back to 5% at 90% span.

Similarly in the 135° sector, the largest variations between the base and shape 2 profiles are observed at the 10% span, with a difference of approximately 7%. This difference then decreases to 3% at 30% span, where it remains relatively level. Instead of a clear peak and valley, a plateau is observed in the 10% spans in the 135° sector. As mentioned, the power data is extracted from each blade surface at a single instant in time. At the instant of time when the 135° data was extracted, a blade was not in the region of maximum power, so the peak is not clearly captured in the discreet data set. Peak to peak variation for the 135° sector is less than the 90° sector by approximately 1kW.

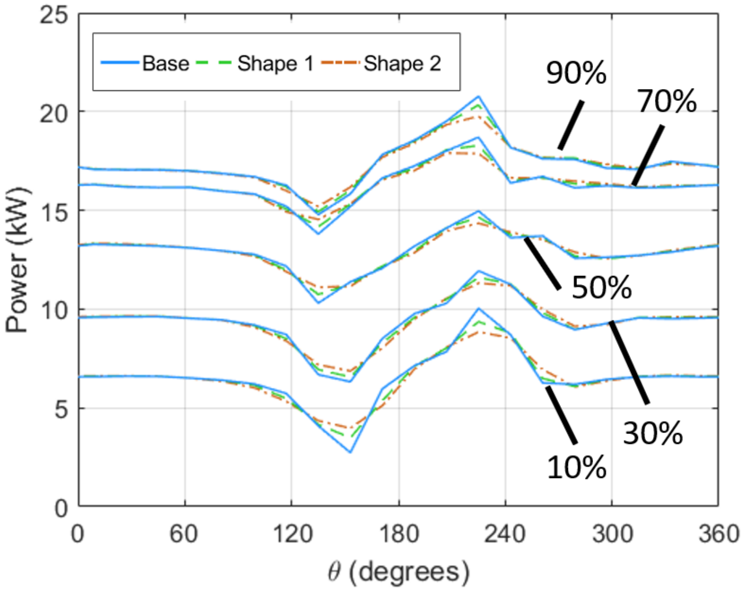

Figure 4.18: Local power variations across the rotor for the 90° sector.

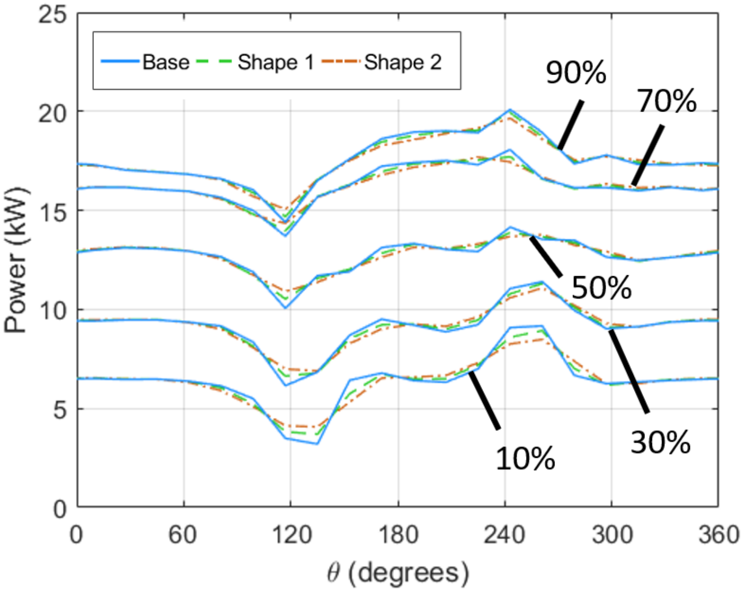

Figure 4.19: Local power variations across the rotor for the 135° sector.

Blade static pressure distributions provide insight into the effect of distortion on loading, shock strength, shock location, pressure rise, and incidence. To further investigate the power variations observed at 10% span where power variation due to shape was greatest, rotor blade loading diagrams were generated and are shown in Figure 4.20 for a single instance in time. In the figure, 3 blade loading profiles are plotted, each at a different blade in the rotor blade row. One profile is for the blade with the highest recorded power (red), which corresponds to the blade in the counter-swirl region. The second is for the blade with the lowest recorded power (blue), which occurs in the co-swirl region. The third is for a blade which experiences the average power in the rotor blade row (green), calculated by finding the blade loading profile with the calculated power value closest to the average power calculated for the rotor at a given instant in time. Figure 4.20 only compares the base case with shape 2 for simplicity. The trends discussed in this section were observed in both the 90° and 135° sectors, and thus only the 90° sector is shown. Blade loading diagrams for both sectors and all spans are included in Appendix A.2 for reference.

Figure 4.20 shows the results at 10% span. As expected, the profile representing the blade with minimum power (blue) has the lowest loading and the profile representing the blade with maximum power (red) has the highest loading. The pressure profile of the suction surface is generally similar for both the base and shape 2. However the pressure surface of the maximum power blade is lower (3% to 3.5%) than base and the pressure surface of the minimum power blade is higher (4% to 5%) than the base. For the 90° sector, shape 2 increased the minimum loading and decreased the maximum loading, thus decreasing the variation from the base. This supports Fig. 4.18 where it was observed that shape 2 resulted in a lower maximum power variation and an increase in power observed at the valleys.

The blade loading associated with maximum power which occurs where maximum counter-swirl is present shows evidence of a passage shock between 30% chord on the suction surface and 25% chord on the pressure surface. The presence of this shock was further explored by plotting the axial velocity in the blade passages at 10% span, which is included in Figure 4.22. In the region of maximum loading indicated in the figure, the flow has accelerated through 4 blade passages resulting in the formation of a shock wave. No shocks are observed in the indicated regions of minimum and average blade loading. The blade loading profiles of Fig. 4.20 also show that the incidence increases at max loading and the minimum power blades exist where co-swirl is present.

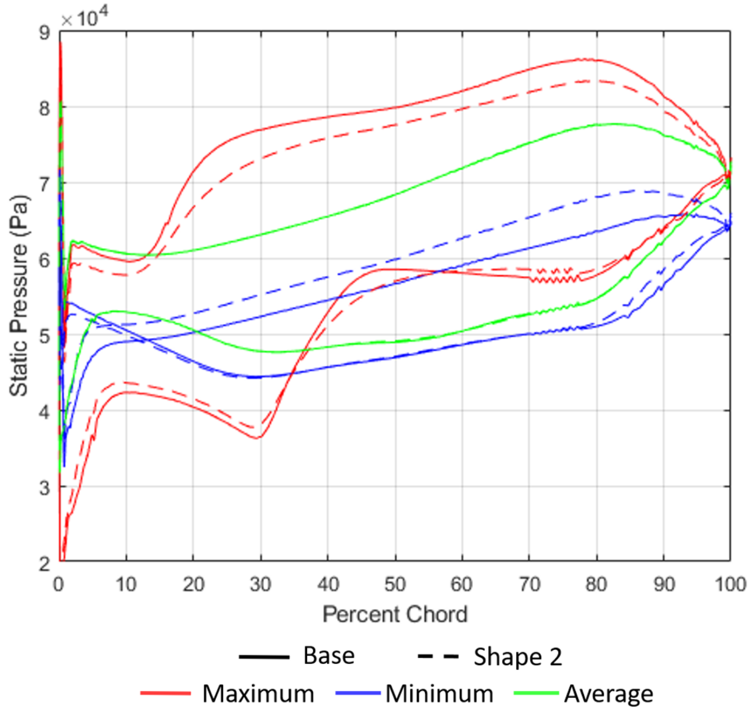

Figure 4.20: Blade loading diagram for 10% span with 90° distortion sector.

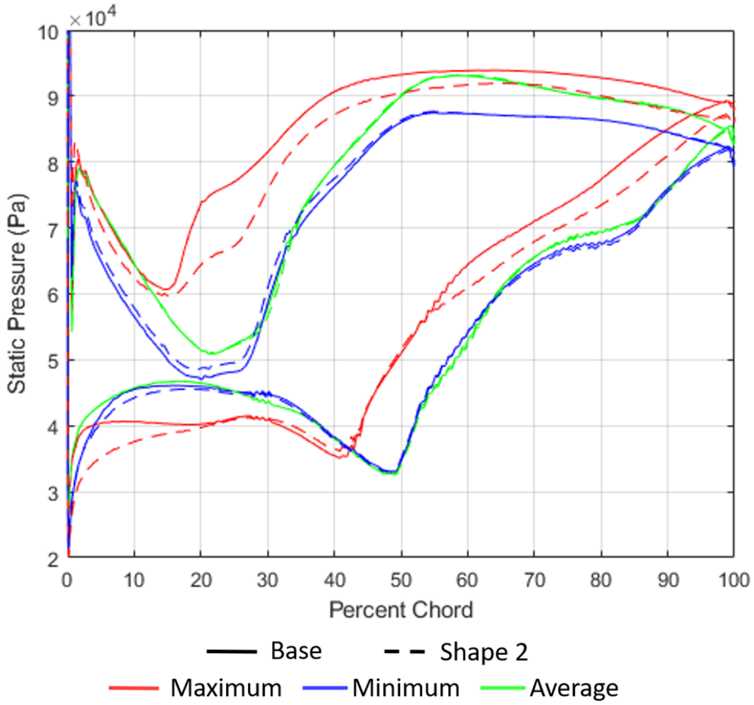

Figure 4.21: Blade loading diagram for 70% span with 90° distortion sector.

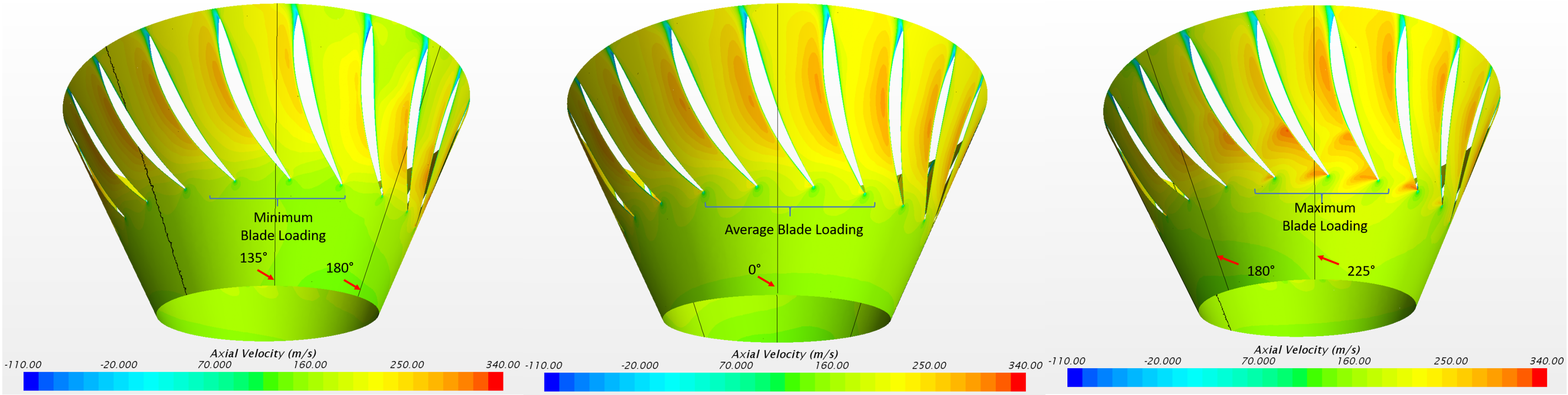

Figure 4.22: Axial velocity at 10% span in the 90° base simulation with regions of maximum, minimum, and average blade loading identified. Flow is from bottom to top.

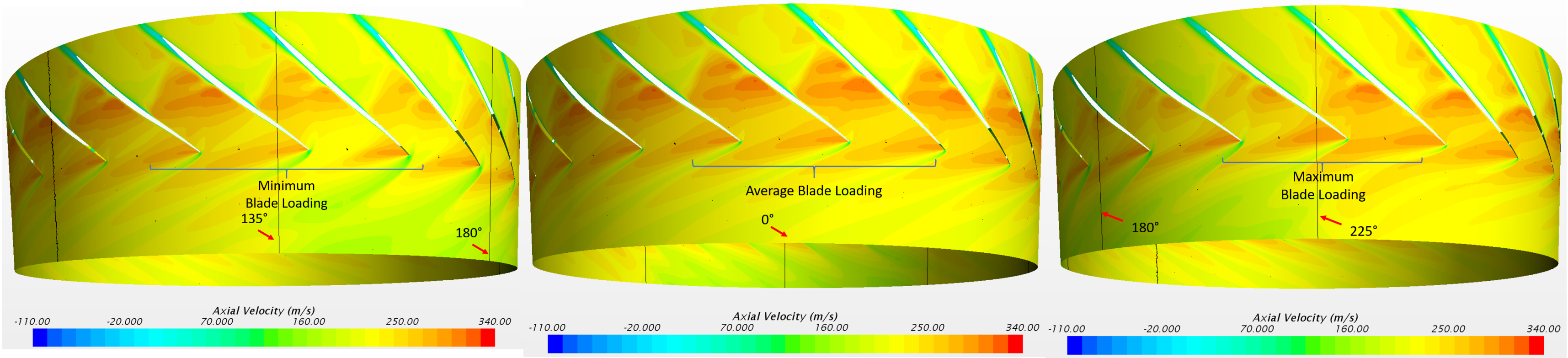

Figure 4.23: Axial velocity at 70% span in the 90° base simulation with regions of maximum, minimum, and average blade loading identified. Flow is from bottom to top.

Fig. 4.21 shows blade loading profiles for the 90° sector at 70% span. The blade loading associated with minimum power shows little difference between the base and shape 2. The passage shock does not move and is in the same location as the average power blade. The suction surface profile of the minimum power blade is nearly the same as the profile of the average power blade. However the pressure surface shows the minimum power pressure magnitude is 8% lower for the first 30% chord and 6% lower for the aft 50% chord compared to the average power blade.

Figure 4.21 also shows the blade loading associated with maximum power is very different at 70% span than the average and minimum power loading. The passage shock has moved upstream approximately 20% chord at the pressure surface and 10% chord at the suction surface and is subsequently more forward loaded than the other two profiles. There are also significant differences between base and shape 2 for this loading. At the suction surface leading edge the incidence increases, observed in Figure 4.21 as an decrease in static pressure at low spans. Over the last 40% chord the pressure profile decreased by 3%. On pressure surface shape 2 passage shock moves back 14% and the pressure magnitude 3% less than base.

Plots of axial velocity through the blade passages at 70% span illustrate some of the differences in passage shock observed in the blade loading profiles, and are provided in Figure 4.23. In the region of minimum blade loading, the flow through the passage is observed to be slightly slower compared to the average blade loading location, with a reduction in maximum velocity through the passage of approximately $30\frac{m}{s}$, which is a decrease of 9% relative to the maximum velocity in the average blade loading passages. This indicates a reduction in passage shock strength, which was observed in the blade loading plots in Figure 4.21. Additionally, comparing the maximum blade loading contour to the average and minimum contour reveals that the passage shock, indicated by a sharp drop in axial velocity through a blade passage, has moved upstream by approximately 7%. Weston observed a similar upstream migration of passage shock through a low pressure distortion region, with the upstream movement equaling approximately 8% with the shock staying between 18% and 40% chord [10].

4.8 Discussion on Radial Migration

The results presented showed a clear relationship between P_t inlet distortion, induced swirl, and distortion transfer and generation. Figures 4.3 through 4.17 show that as induced swirl was reduced as a consequence of a less abrupt inlet distortion transition, the distortion transfer and generation was reduced. However, Figures 4.3 and 4.4 show that there was very little change in swirl profile at 50%, 70%, and 90% span yet Figures 4.12, 4.13, 4.16 and 4.17 show significant change in distortion transfer and generation between the base and shapes 1 and 2 at all spans. The distortion transfer and generation present at the outer spans where no swirl was induced is of the same magnitude as that at the lower spans where induced swirl was affected by the transition abruptness.

As described by Weston [10] the static pressure gradient formed in response to inlet P_t distortion creates a force imbalance causing bulk fluid motion in circumferential and radial directions. Fidalgo [17] noted that in response to inlet P_t distortion the stagnation point on the spinner moves which also induces a radial mass redistribution. Based on this, distortion present at the hub can migrate radially outward and thus we see a change in distortion transfer and generation at all spans even though there was no change in induced swirl at 50% span and greater.

4.9 Summary of Results

This chapter focused investigated the impacts of changing the distortion transition abruptness at the edges of an inlet distortion pattern, particularly focusing on any resulting changes in distortion transfer and generation. It was observed that as distortion transition abruptness became more gradual, fan efficiency improved slightly. Though not immense, the recovery in efficiency suggests that distortion behavior is changing for the better as distortion transition becomes less abrupt.

Significant reductions in distortion transfer and generation were observed to occur as distortion transition abruptness became more gradual. This was revealed by comparing total amplitudes of total pressure and total temperature after passing through the rotor. The observed reductions in distortion transfer and generation suggest that reducing the distortion transition abruptness reduces distortion levels as the flow exits the rotor, which would subsequently reduce distortion through a multi-stage compressor. This would result in more significant improvements in efficiency than the small recovery observed in this study.

While changes to efficiency are important to consider, it is critical to predict downstream distortion behavior in order to reduce the impacts of distortion on turbomachinery. This predictive ability was improved through the study of the various inlet distortion variations by showing that the variations in distortion transition abruptness significantly reduced distortion levels after the rotor.

Several evaluations explored the flow physics behind the observed reductions in distortion transfer and generation. Reductions in local blade power variations were observed to correlate with reductions in distortion transfer and generation. As blade power variations decrease, the resulting work on the flow is more uniform and reduces the creation of total temperature distortion. Additionally, variations in flow elements such as bow shocks were observed. Particularly, as distortion transition abruptness becomes more gradual, bow shocks were observed to be reduced in strength. Passage shocks were also observed to move forward in the blade passage with the more gradual transition.

This study suggests that gradual transitions in distortion at the inlet will result in more favorable distortion behavior across the rotor compared to sharper transitions. In a practical application, efforts should be made during design to reduce the sharpness of any inlet distortions. This might be accomplished by implementing additional upstream geometry, altering inlet duct shaping, or flow control.

CHAPTER 5. RESULTS: NOZZLE STUDY

This study will present results which compare simulation parameters between simulations which use nozzle geometry to control operating condition and simulations which use a simplified exit boundary condition. Conventional exit boundary conditions are often used to reduce the complexity of a geometry during CFD simulation, but there is concern that these boundary conditions may have negative impacts on flow fields. Performance parameters for each of the nozzle simulations will be presented and discussed. Conclusions regarding whether the exit boundary condition is sufficient will be made.

At the time of writing this thesis, simulations were still in progress to complete this study. Preliminary results from the study will be presented here, and future work to continue the study will be outlined in Section 7.4.

5.1 Overall Performance Measures

To quantify overall performance measures of the fan with nozzle attached, P_t ratio and efficiency were calculated. P_t ratio was calculated between the spinner inlet and the stator outlet, referred to as stations 2 and 3 respectively using equation 5.1. $P_{t,3}$ and $P_{t,2}$ were calculated as a mass flow average at the given station and operating point. Efficiency for the fan was calculated using equation 5.2 with γ calculated at the average temperature across the stage. $T_{t,3}$ and $T_{t,2}$ were also calculated as a mass flow average at the given stations and operating point.

$$PR = P_{t,3}/P_{t,2} \tag{5.1}$$

$$\eta_f = \frac{\frac{p_{t,3}}{p_{t,2}}^{\frac{\gamma-1}{\gamma}} - 1}{\frac{T_{t,3}}{T_{t,2}} - 1} \tag{5.2}$$

Figure 5.1 compares the pressure ratio between clean inlet experimental data for rotor 4, distorted inlet simulation results without a nozzle, and distorted inlet simulations results with a nozzle. Figure 5.2 compares efficiency for the same three sets of data. The clean inlet experimental case has a peak efficiency of 89.6% at a mass flow of 27.6 $\frac{kg}{s}$. It stalls at a pressure ratio of 2.022 at mass flows below 26.1$\frac{kg}{s}$. Choke occurs at a mass flow of approximately 27.8$\frac{kg}{s}$. Experimental data is provided to provide a rough comparison to ensure simulated results are in the ballpark, and simulated results are not expected to match experimental data due to limitations of the simulation as well as the addition of the inlet distortion.

A visual inspection comparing the distorted inlet simulation performance parameters with the performance of the simulation with a nozzle suggests that they are largely the same. Pressure ratio, efficiency, and mass flow are slightly lower for the simulations with a nozzle, but the performance curves closely follow those from a simulation without a nozzle. A closer investigation of the specific values will confirm that the performance is similar.

The distorted simulations run without a nozzle had a peak efficiency of 85.2% at a mass flow of 28.0$\frac{kg}{s}$. With a nozzle, peak efficiency was recorded as 84.6% at a mass flow of 27.8$\frac{kg}{s}$. The simulation without a nozzle stalled at a pressure ratio of 1.96 and mass flow of 27.1$\frac{kg}{s}$, while the simulations with a nozzle stalled at a pressure ratio of 1.93 and mass flow of 27.2$\frac{kg}{s}$. The simulation without a nozzle choked at a mass flow of 28.1$\frac{kg}{s}$. The closest point to choke simulated for the nozzle was at a mass flow of 27.9$\frac{kg}{s}$. The difference between values for the simulation with a nozzle and those for the simulation without a nozzle are less than 1% in all cases.

With striking similarity in performance parameters, it can initially be concluded that the addition of a nozzle did not drastically alter the simulation. This in turn suggests that the simplified exit boundary assumption, which removes the need for a nozzle, does not negatively impact the simulation. This means that results, such as those presented in Chapter 4 on inlet distortion variation are not biased nor incorrect.

While these results are promising, to fully confirm this conclusion, flow fields between the two simulation types should be compared. This will ensure that there are not significant alterations to the flow field elements due to the nozzle.

Though not explicitly measured, simulation convergence times were not observed to be significantly longer for the simulations with a nozzle. While the addition of a nozzle does make

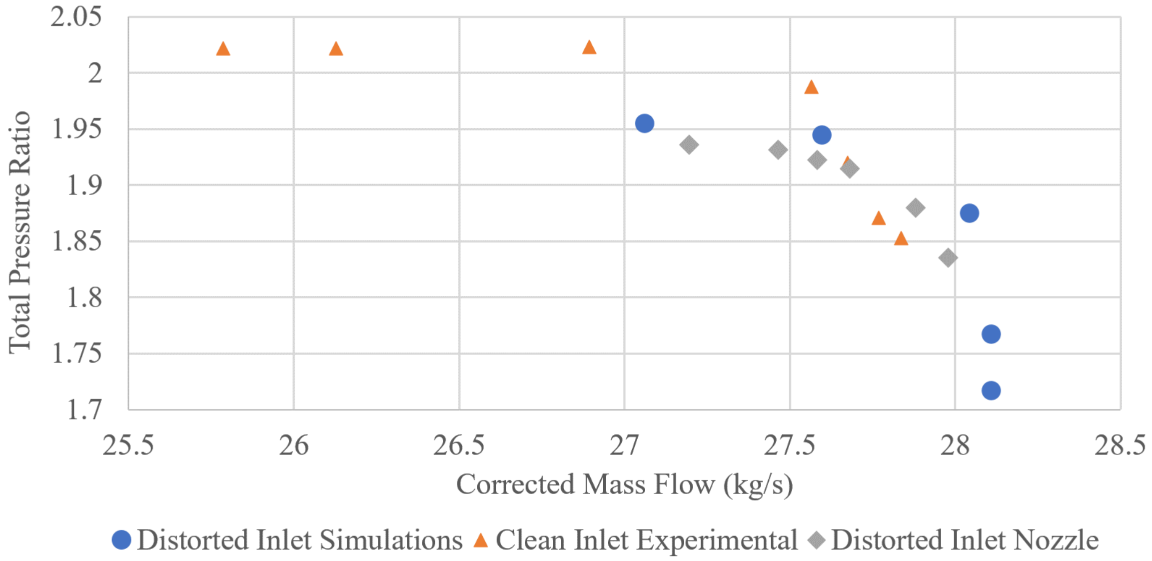

Figure 5.1: Stage pressure ratios.

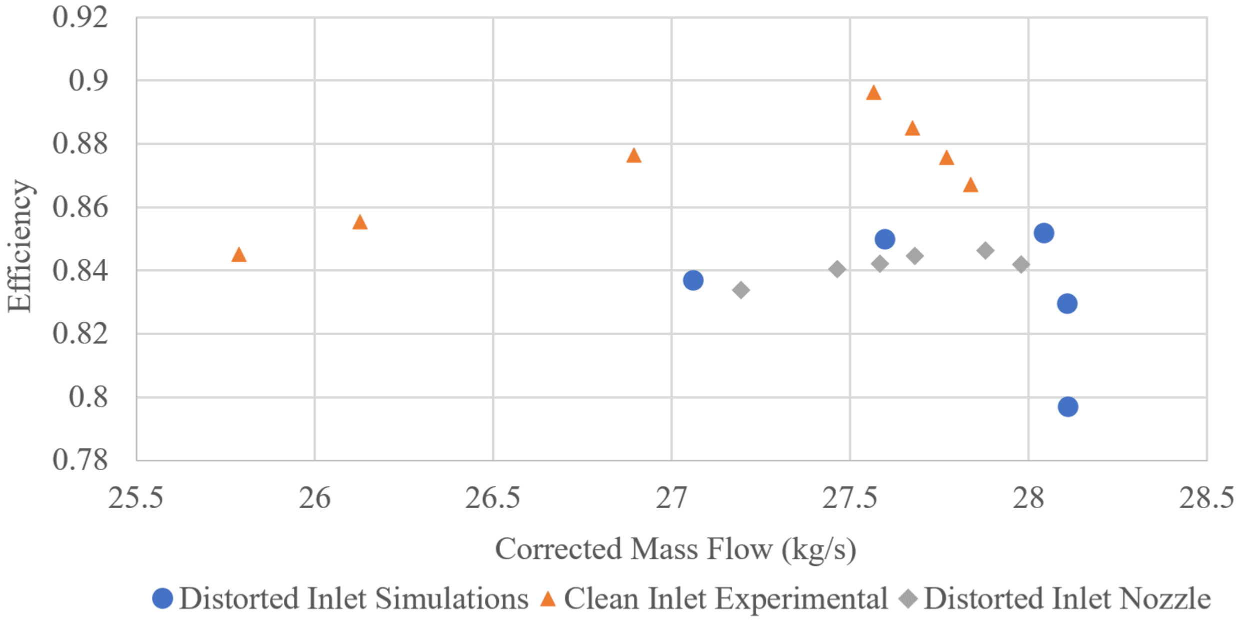

Figure 5.2: Stage efficiencies.

the simulation more complex and larger, it did not appear to have a significant impact on solution time.

5.2 Contour Comparisons

To compare flow fields, contours of flow properties were compared at several axial locations in the geometry. These contour plots were time-averaged over 18° of rotor rotation, or one blade passage, in 1° increments per time step. To provide a clear comparison between the two series of simulations, the contour from the simulation with a nozzle is presented as a difference from the simulation without a nozzle. At each location in the contour, the value shown was the result of subtracting the value observed in the nozzle simulation from the corresponding value in the simulation without a nozzle. In these contours, positive values indicate an increase in property relative to the simulation without a nozzle, while a negative value indicates a decrease relative to the simulation without a nozzle.

The most accurate comparison between series of simulations would occur at a point where operating condition matched exactly. However, as seen in Section 5.1, variations in operating condition are introduced by adding a nozzle. This means that selecting a perfect match in operating condition between simulation series was not feasible. The best agreement in operating point between the two series was observed to be at peak efficiency and the peak efficiency point in both series was used for flow field comparisons. The difference in performance parameters at the peak efficiency operating point was minimal, with the pressure ratio being 0.2% higher in the nozzle simulation, the efficiency being 0.6% higher in the simulation without a nozzle, and the mass flow being $0.16\frac{kg}{s}$ higher in the simulation without a nozzle. These differences are small on the scale of performance parameters, but do indicate we should observe some variation in flow fields due to operating point, in addition to any variations caused by the addition of a nozzle.

Figure 5.3 shows comparisons between the P_t fields at the stator inlet for peak efficiency for both series of simulations. The contour for the nozzle simulation shows a clear increase in P_t relative to the no-nozzle simulation. The average increase of the profile is 3.8% relative to the no-nozzle simulation with the greatest differences observed at approximately 70% span and higher. The uniform nature of this increase suggests that it is due primarily to a difference in

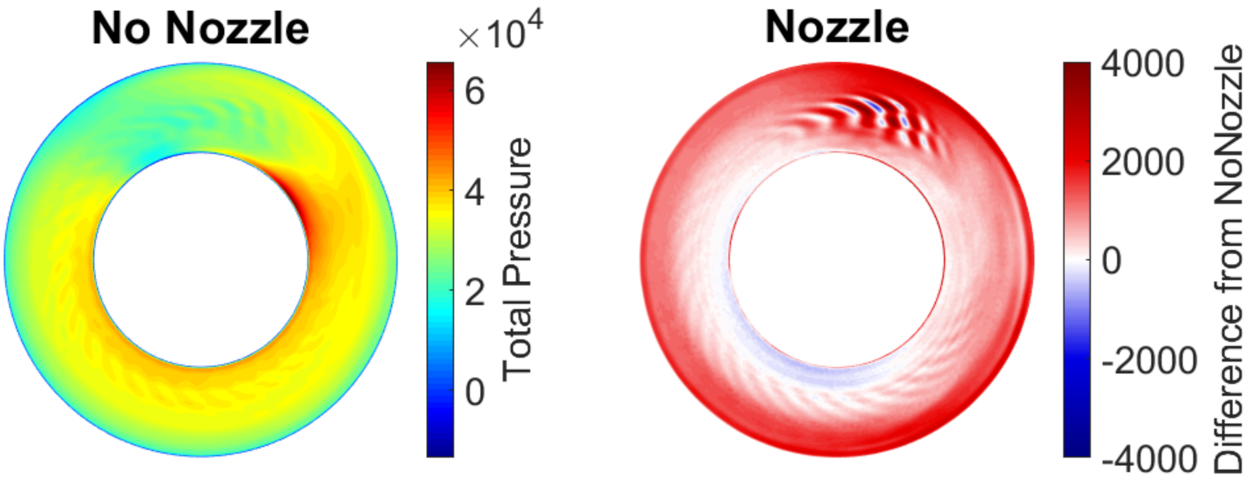

Figure 5.3: P_t at stator inlet (pa) at peak efficiency. Nozzle contour represents the difference from the no-nozzle. View is forward looking aft.

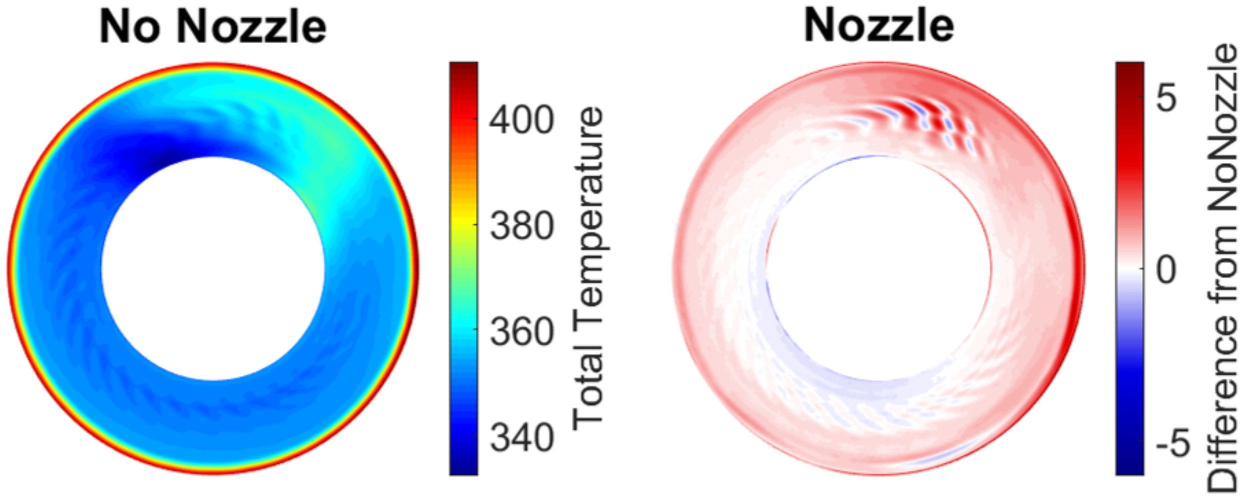

Figure 5.4: T_t at stator inlet (pa) at peak efficiency. Nozzle contour represents the difference from the no-nozzle. View is forward looking aft.

operation condition. No large variations in contour trends are observed, which suggests that the static boundary exit condition was not altering flow elements independently.

Figure 5.4 shows comparisons between the T_t fields at the stator inlet for peak efficiency. As with P_t, the nozzle contour shows a clear increase, with an average increase of 0.17% relative to the no-nozzle simulation. This difference was minimal and was concentrated at the outer 5% spans between 180° and 0°. This uniform variation is primarily attributed to the difference in operating condition as well, and is not considered to be due to the addition of the nozzle.

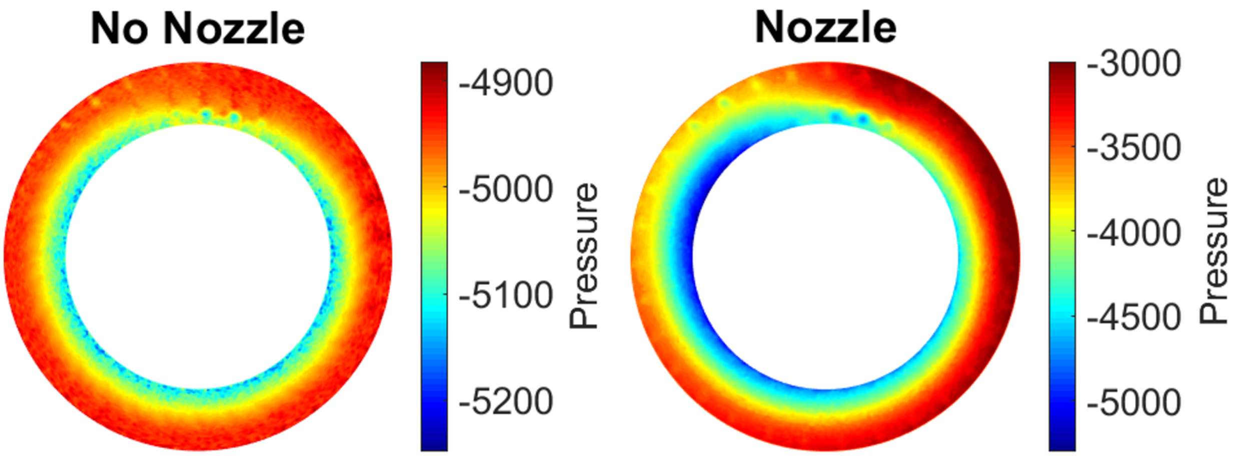

Figure 5.5: Static pressure (Pa) at the stator outlet for both series of simulations. View is forward looking aft. Static pressure is presented as a gauge value relative to 1 atmosphere of pressure.

To ensure that the use of the static pressure boundary condition was not negatively impacting the stator, time averaged static pressure contours were obtained at two locations for the stator. Figure 5.5 shows the static pressure at a plane immediately preceding the stator outlet plane, as identified in Figure 3.2. The no-nozzle contour represents the applied exit static pressure condition, which was a radial equilibrium starting from a specified hub pressure. It was observed here that the pressure distribution for both simulations were similar, with low static pressures at the hub and higher static pressures at the casing. There was an observable difference in static pressure magnitude, with the nozzle simulation having a higher overall static pressure. This is likely a result of the difference in operating point between the two simulations. The higher static pressure observed in the nozzle simulation corresponds with the decrease in mass flow and efficiency observed when comparing performance parameters.

Time accurate axial distributions of static pressure were also plotted through the stator and nozzle to ensure there were no negative static pressure effects which migrated upstream through the stator. Figure 5.6 shows the static pressure through the stator for the simulation without a nozzle and Figure 5.7 shows the static pressure through the stator and nozzle region. Both are top down views of the stator and show the distorted region centered around 180°. As with the circumferential contours shown in Figure 5.5, the simulation with a nozzle shows a higher static pressure, especially at the low end of the scale. No large variations in the static pressure distribution are observed. Notably, the static pressure contours on the stator vane suction and pressure surfaces are very similar between both simulations. This supports the conclusion that the use of a static pressure exit boundary condition close to the stator does not have any significant negative impacts on the back pressuring of the stator.

The performance parameters and flow fields evaluated between the two series of simulations present solid evidence that the use of a static pressure boundary close to the stator, as opposed to a nozzle, does not have drastic impacts on a simulation. Small variations in operating point were observed but since distortion research is primarily focused on characterizing flow trends rather than providing quantitative values, these operating point variations are not a large concern. The comparison of flow fields showed that there were no major variations in the distribution of total pressure nor temperature after passing through the rotor. Static pressure distributions were also observed to be similar through the stator. Together, these results suggest that the static pressure exit boundary condition is sufficient for controlling the mass flow through a simulated fan and does not negatively impact the flow field trends.

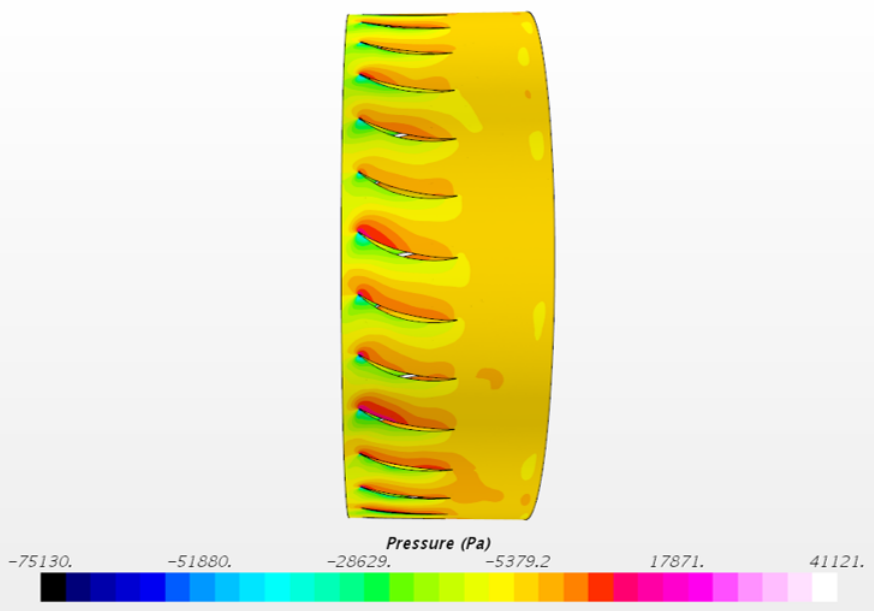

Figure 5.6: Static pressure (Pa) through the stator for the simulation without nozzle geometry. Flow is from left to right and view is from the top (180°) down. Static pressure is presented as a gauge value relative to 1 atmosphere of pressure.

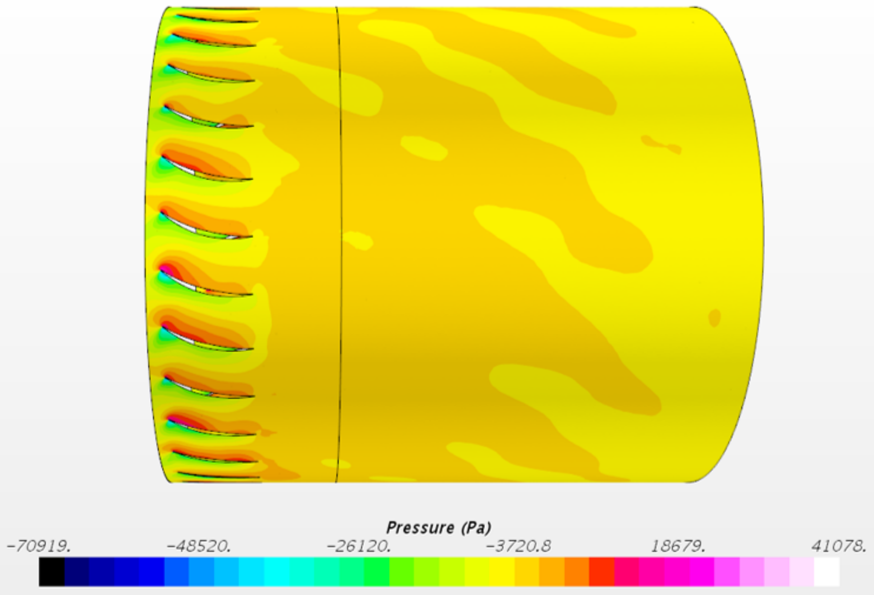

Figure 5.7: Static pressure (Pa) through the stator for the simulation with nozzle geometry. Flow is from left to right and view is from the top (180°) down. Static pressure is presented as a gauge value relative to 1 atmosphere of pressure.

CHAPTER 6. RESULTS: PHASE SHIFT STUDY

This chapter will present the results for the study on distortion descriptors used to quantify distortion phase shift, or circumferential migrations of distortion. These results will include an overview of the pressure induced swirl, exploration of P_t and T_t phase shifts, and a discussion on the merits of the various phase descriptors outlined in Section 3.3.2.

6.1 Pressure Induced Swirl

The applied distortion pattern shown in Figure 3.9 results in the pressure induced swirl shown in Figure 6.1 before it passes through the rotor for five spans at choke, design, and near-stall operating conditions. Regions of co- and counter-swirl are observed in the traverse at 135° and counter-swirl at 225°. These regions occur at approximately the same circumferential locations as the boundaries of the inlet P_t distortion. At the region where the rotor blades begin to enter the distorted sector, the swirl is in the same direction as the rotor movement and is referred to as co-swirl. Co-swirl decreases rotor incidence angle. As the blades leave the distorted region, they experience counter-swirl, or swirl in the direction opposite the rotor. This increases rotor incidence angle. The regions of co- and counter-swirl are identified in Figure 6.1.

Differences in induced swirl are largest between design and near-stall operating conditions, with near-stall having larger magnitudes of co- and counter-swirl. The largest magnitude difference between design and near-stall is observed at 10% span in the counter-swirl region with near-stall 3° (20%) more swirl relative to design and choke. The difference in magnitude decreases to approximately 1.5° at 90% span, which is almost two times the swirl at design and choke. As span increases, the magnitude of the difference between near-stall and design decreases, but the percent difference relative to design increases. In the region of co-swirl, less than 1° of difference between near-stall and design is observed for all spans; equivalent to an approximate 7% increase relative to design. Choke and design conditions contain near identical levels of swirl.

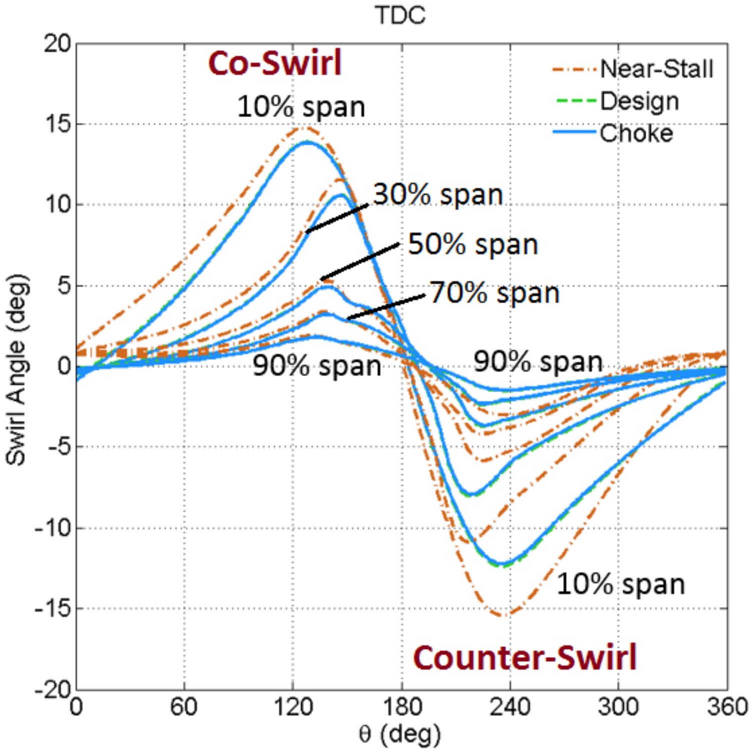

Figure 6.1: Circumferential traverses of induced swirl at rotor.

6.2 Total Pressure Phase Shift

P_t traverses at several radial locations were extracted from the simulation and are shown in Figure 6.2. The P_t traverses were extracted from a plane at the stator inlet. Three operating conditions are represented: choke, design, and near-stall. The presented data is a result of reconstructing the raw data using the first 12 modes of a Fourier series in order to remove high-frequency effects of the blades.

These traverses have clear peaks and valleys as seen in Figure 6.2, especially at the spans closest to the hub. These correspond to the circumferential locations of the co- and counter-swirl identified in Figure 6.1. At 10% span, the valley occurs at 135° and the peak occurs at 225°. As the spans increase and as operating point moves from choke to near-stall, the difference between peak magnitude and valley magnitude decreases. At 10% span, the P_t traverses closely match, with variations concentrated at the extrema of the traverse (5% difference in near-stall relative to design).

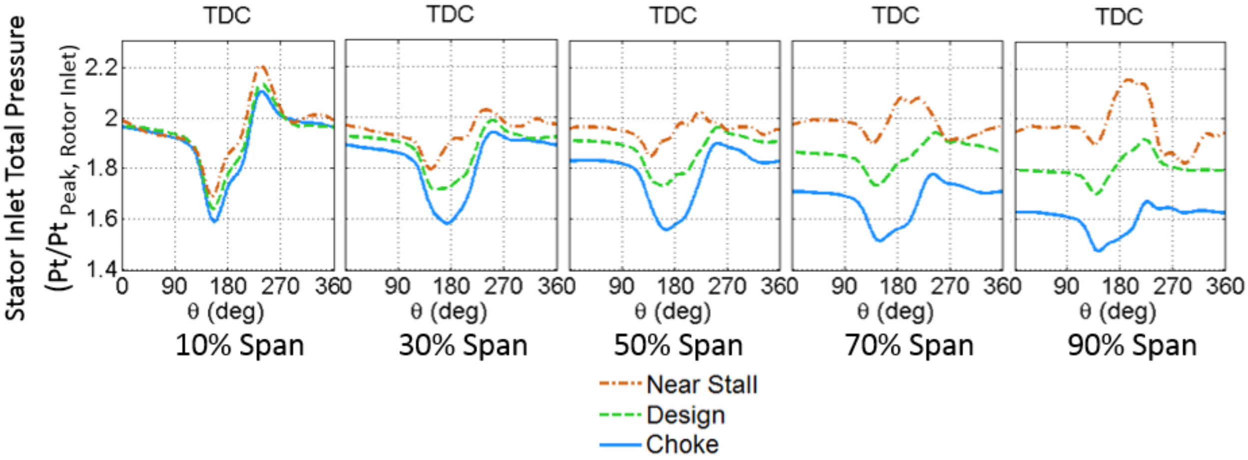

Figure 6.2: Circumferential traverses of P_t at stator inlet.

Moving towards the blade tip, the traverses exhibit greater differences, suggesting that differences in distortion are mainly observed at higher spans. At the 90% span, the near-stall traverse is approximately 20% greater than the choke traverse. Figure 6.2 also shows that from 10% to 70% span, moving from near-stall to choke reduces the amplitudes of the peaks relative to the undistorted flow and increases the amplitudes of the valleys. Additional results regarding these traverses can be found in the previous work by Soderquist et al [3].

6.2.1 Modal Fourier Phase Shift

The first five Modal Fourier P_t Phase Shifts, as defined in Section 3.3.2, across the rotor for five spans are shown in Figure 6.3. The large scale shaping of the Fourier series occurs in the early terms of the Fourier transform, thus only the first 5 modes are included in the modal analysis as opposed to evaluating all 12. As presented by Peterson, this modal analysis can give insight into shape changes and translation [9]. If all modal phase shifts have similar values, the distortion pattern has translated, and has not changed shape. In this case and if the modal phase shifts are negative, this would indicate a clockwise translation, or in the direction of rotor rotation. Conversely, if the phase shifts are positive, it would indicate a counter-clockwise translation.

If some modes have drastically different phase shifts, the distortion pattern has changed shape. Larger modal phase magnitudes correspond to larger changes in shape. Connecting the modal values to a physically significant value for translation or change in shape which would be observed in a flow field has not been accomplished. Rather, the modal phase shift values reveal trends. This is a current limitation of the Fourier-based description methods.

Comparing the modal phase at the different spans reveals where the distortion has translated versus where it has changed shape. Due to the minimal differences between modal phase shifts (less than 20°) at 30% span for design and choke, the distortion profile is assumed to have translated evenly and not experienced large changes in shape. Larger changes in modal phases for these operating conditions are observed for mode 4, which may indicate some change in shape. Similarly, the choke modal phase shifts at 70% and 90% spans are relatively constant around $-25°$ which suggests that the distortion profile translated clockwise and did not drastically change shape. In contrast, the large variations in modal phase shift observed at all spans for the near-stall case suggest that the distortion changes shape as opposed to uniformly translating.

In general, the stall phase shifts have larger magnitudes of modal phase shift. This signifies that distortion shape changes most across the rotor for the near-stall simulation. The differences in modal phase tend to be largest at spans above 50%, suggesting that the distortion pattern differences are greatest at larger spans. Choke tends to have smallest magnitude of modal phase shift.

At most spans, the modal phase tends to follow similar trends, at different magnitudes, for each operating condition. This suggests that distortion shape or translation is similar between operating conditions, but occur with different magnitudes. A notable exception occurs with mode 1 modal phase shift at 70% and 90% spans for near-stall. In both cases, the mode 1 phase shift is over 150, with the design and near-choke case being less than 0. These variations suggest that flow behavior at large spans results in distortion profile translation or shape change which is unique to the near-stall case.

Several limitations of this method become clear when attempting to analyze the trends in Figure 6.3. The first is that it is difficult to correlate the values observed directly with observable changes in shape. That is, beyond concluding that the shape has changed and to what magnitude, we cannot use these values to determine how the shape has changed. We cannot clearly identify whether the shape has shifted co- or counter-clockwise nor whether it has expanded or contracted. We can simply conclude that it has changed. Connected to this is the difficulty of dealing with information at each mode of the transform. Each mode shows different values for modal phase

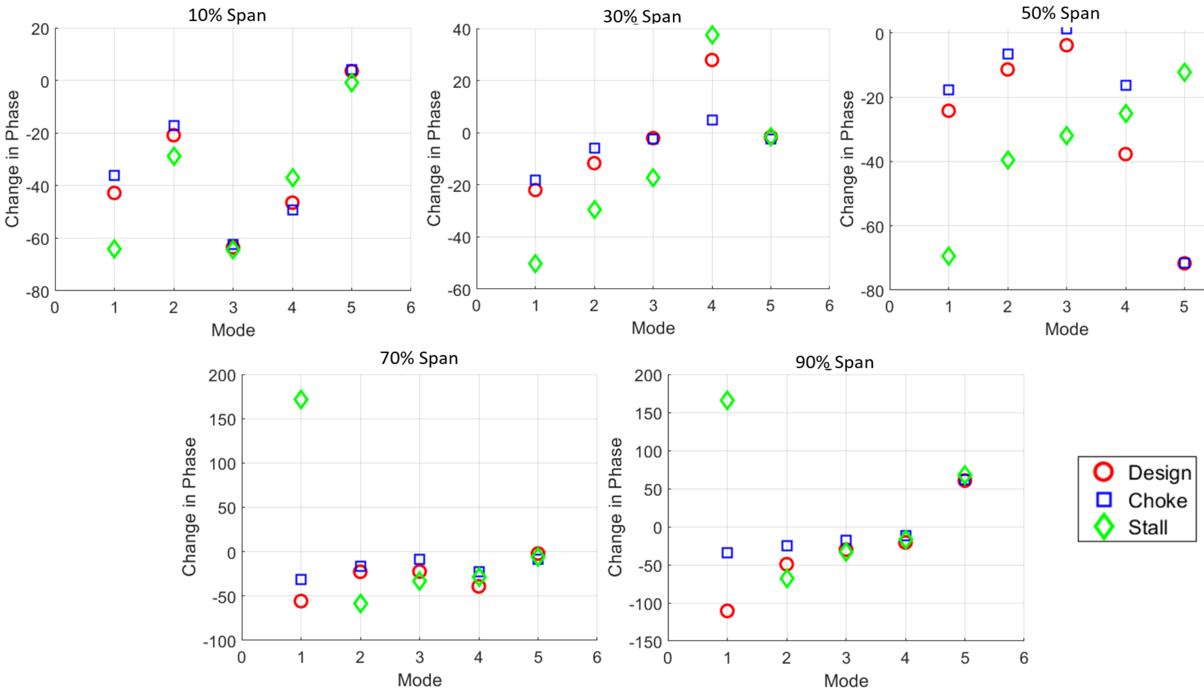

Figure 6.3: Modal Fourier Phase Shifts of P_t across the rotor.

shift, and connecting all the modal information in a meaningful way is challenging with the modal data in this form.

6.2.2 Total Fourier Phase Shift

Total Fourier P_t Phase Shifts, as defined in Section 3.3.2, across the rotor for 5 spans are shown in Figure 6.4. This descriptor attempts to combine the modal information at each span into a single value. In this process, the ability to determine if a profile has shifted or change shape has been removed. Instead, larger magnitudes of Total Fourier Phase Shift would suggest larger distortion profile changes, these changes either being translation or distortion.

Some interesting trends are observed. The near-stall operating condition consistently has the smallest magnitude of Total Fourier Phase shift, with choke and design alternating which has the largest magnitude. This does not seem to correspond well with the modal results observed in Figure 6.3, where it was concluded that near-stall frequently had the largest shape change of the three operating points. We would intuitively expect that the near-stall case would have larger levels of Total Phase shift due to the significant changes in shape suggested by the modal data. The

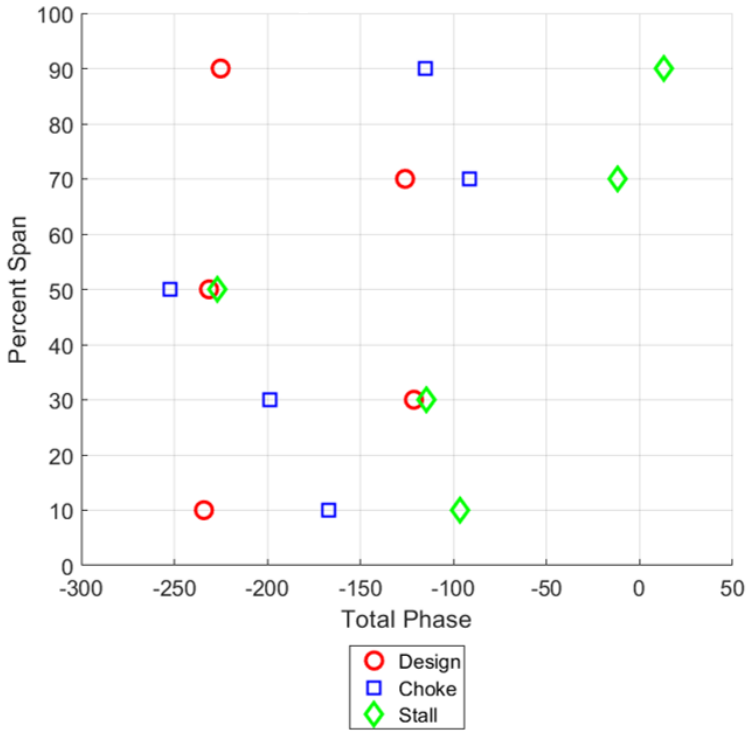

Figure 6.4: Total Fourier Phase Shifts of P_t across the rotor.

discrepancy is likely due to the simple summation of positive and negative modal phases utilized by the Total Phase methodology. To illustrate, the stall operating point experiences a unique and large shape change at large spans, which would effectively cancel out any negative phase information from lower spans. Such cancellation effects make it difficult to obtain meaningful results using this descriptor unless the modal phases are all of the same sign.

Between the design and choke operating points, design tends to have larger magnitudes of Total Phase. This would suggest that changes in profile position and shape are more pronounced at near design when compared to choke. This holds true at 10%, 70% and 90% span. Choke has larger magnitudes of Total Phase at 30% and 50% span, suggesting that profile changes at these spans are greater for the choke. The Total Phases at 50% span for each operating condition are within 10% of each other, which suggests that the distortion profile changes are of similar magnitudes.

6.2.3 RSS Modal Phase Shift

RSS Modal Phase shifts of P_t, as defined in Section 3.3.2, across the rotor for 5 spans are shown in Figure 6.5. This descriptor more intelligently combines the modal Fourier information

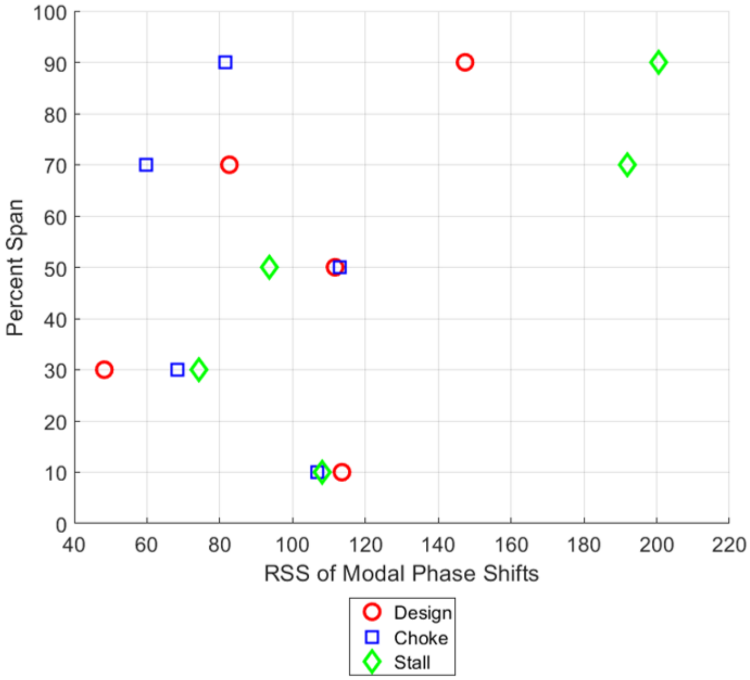

Figure 6.5: RSS Modal Phase Shifts of P_t across the rotor.

in a manner which does not allow for cancellation of phase, which was observed with the Total Fourier Phase. The resulting value is a mean modal phase shift value. This method also eliminates the ability to discern between translation and profile shape change. Larger values of RSS Modal Phase suggest a more drastic alteration (Change in shape and/or translation) of distortion profile compared to a lower RSS Modal Phase.

Figure 6.5 shows that at spans above 50%, there is a significant difference in phase between the three operating points, spanning over 140° of RSS modal phase shift. This correlates well to what was observed with the modal phase shift data, suggesting that large differences in distortion profiles occur at high spans, with a near-stall operating point producing the most pronounced changes. It is also worthwhile to note that there are minor differences between the operating conditions at 10% span. Differences remain small through 50% span. This supports the concept that since tip speeds are greater, small disturbances will be magnified.

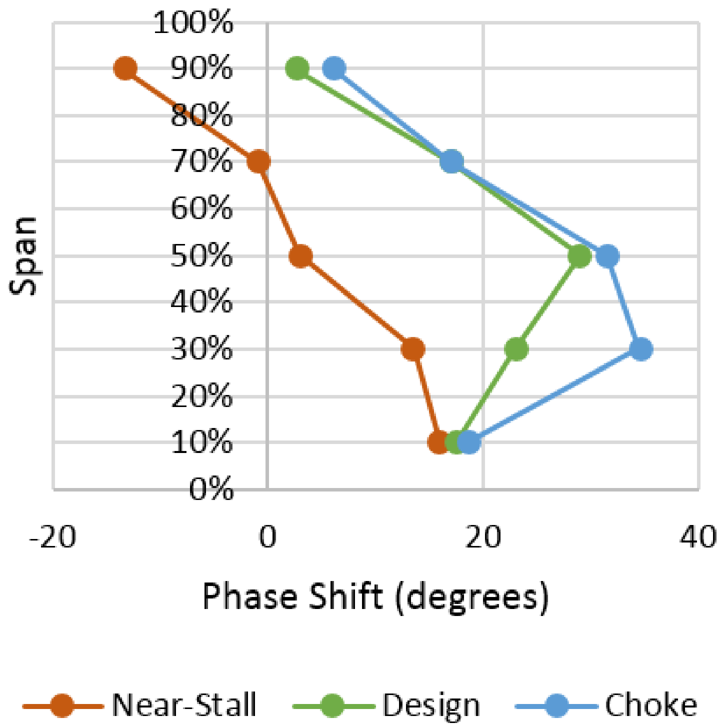

Figure 6.6: Simplified phase shift of P_t across the rotor.

6.2.4 Simplified Phase Shift

The simplified P_t phase shifts (as defined in Figure 3.10) across the rotor are presented in Figure 6.6 and represent the circumferential translation of the distorted region as it passes through the rotor. As shown in Figure 6.6, the near-stall operating point has the most negative, i.e. most counter-clockwise, values. The phase shift for the near-stall condition is about 15° from 10% to 30% span, near 0° from 50% to 70% span, and -14° at 90% span.

The design and choke simulations have very similar phase shift values, with the choke simulation having a more positive shift (35° vs 23°) at 30% span. The shifts for these two operating points become more positive from hub (about 18°) to the midspans (about 30°), and then they become more negative from midspan (about 30°) to tip (about 4°). The fact that design and choke phase shifts matched well but that the near-stall phase shifts differed suggests that there is similar distortion behavior between design and choke, but that distortion has markedly different behavior near stall. This was observed in [3], where it was concluded that large changes in distortion trans-

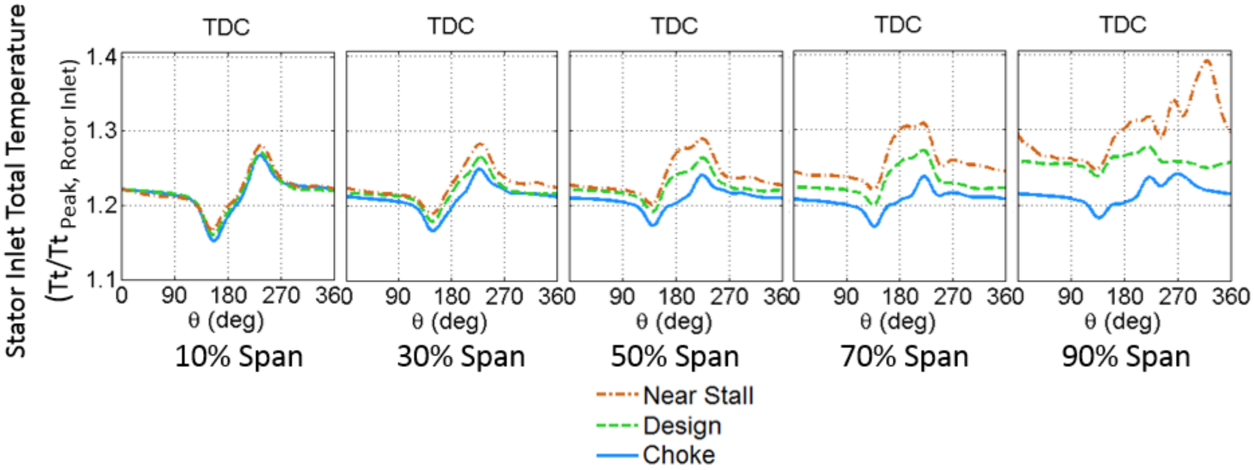

Figure 6.7: Circumferential traverses of T_t at the stator inlet.

fer and generation occur between design and near-stall operation points, while there are minimal differences between choke and design.

These results show that for design and choke cases, distortion phase tends to shift circumferentially in the direction of rotor motion. The magnitudes of these shifts increases near 30% span, and decrease near the blade tip. Different behavior is observed in the near-stall case, where the distortion shift is in the direction of rotor motion near the hub, but steadily decreases until it moves opposite the direction of rotor motion near the blade tip.

6.3 Total Temperature Phase Shift

Circumferential T_t traverses at the same five radial locations were extracted from the simulation and are shown in Figure 6.7. As with the the P_t traverses in Figure 6.2, peaks and valleys can be clearly seen. The locations of the peaks and valleys again correspond to the regions of co- and counter-swirl observed near 135° and 225°. The peaks and valleys are clearly defined near the hub, and become less defined near the rotor tips.

The traverses match closely in shape and magnitudes up to 30% span, where we begin to see a rise in the magnitude of the traverse at near-stall of approximately 3% relative to the choke condition. As span continues to increase, the peak in the near-stall and design conditions become less defined, and the difference between near-stall and choke increases to 6%, with design being 3% less than near-stall. It should be noted that the majority of the differences occur near the peak, which corresponds to the region of counter-swirl, while variations near the valleys are lesser in magnitude, climbing to a 4% difference between near-stall and choke at the 70% span. At the 90% span, the near-stall traverse varies significantly from the others, with a peak occurring approximately 315°.

For the purposes of this section, TDC or 180° was assumed to be the center of the T_t distortion at the rotor inlet. With no applied distortion profile, a center location must be identified to enable the calculations of phase shift.

6.3.1 Modal Fourier Phase Shift

The first five Modal Fourier T_t Phase Shifts, as defined in Section 3.3.2, across the rotor for five spans are shown in Figure 6.8. As a reminder, the modal phase shifts help describe if the distortion has translated or changed shape. If the modal phase shift for each mode are similar in value, the distortion has translated. If this value is negative, the distortion has translated clockwise, or in the direction of the rotor. If the modal phase shifts for each mode show significant variation, the distortion has changed shape.

The only case where pure translation can be identified is in the choked case at 30% span. The modal phase shift values are all near -25°, which would suggest the distortion has translated by approximately 25° in the direction of the rotor. For all other spans and operating conditions, the variations in Modal Phase between modes is large, which suggests that changes in shape dominate the profiles as they cross the rotor. This is to be expected, since the T_t field upstream of the rotor is constant. As the flow crosses the rotor, T_t distortion is generated, resulting in changes in the profile shape, which was initially constant. The majority of the modal phases are negative, which suggest reshaping or translation in a clockwise direction, or in the direction of the rotor.

Mode 1 shows consistently large spread between the phase shifts for each operating point, with stall tending to have larger magnitudes. This is not the case however at high spans, where stall has a much lower magnitude phase shift than design or choke. Mode 1 also reveals that choke tends to have a phase shift greater (more positive) than design. Such observations using mode 1 would suggest that T_t shape differs significantly between the three operating points. However, significant shape differences are not observed at low spans in the traverses shown in Figure 6.7.

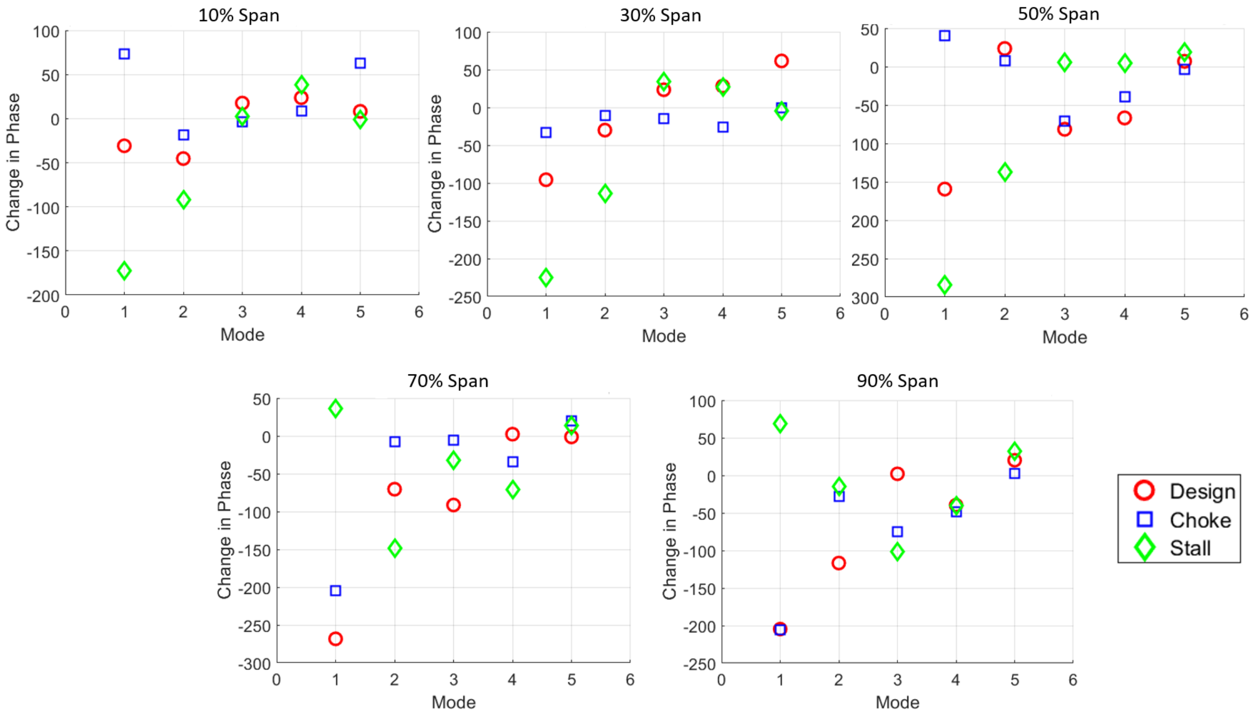

Figure 6.8: Modal Fourier Phase Shifts of T_t across the rotor.

This supports the idea that modal analysis is limited due to its inability to consider multiple modes simultaneously.

6.3.2 Total Fourier Phase Shift

Total Fourier T_t phase shift, as defined in Section 3.3.2, is shown in Figure 6.9. Each of the operating conditions follow a similar trend between 30% and 70% span, each increasing in magnitude by 100° of Total Phase, at a rate of 50° per20% span. This suggests that between 30% and 70% spans, changes in distortion profile are similar between operating conditions. Differences in this increasing trend are observed at 10% and 90% spans. Choke shows a decrease of 10° in total phase magnitude at 90% span instead of continuing to increase in magnitude, suggesting less alteration in the distortion profile. Stall drastically decreases by 200° at 90% span. This could be an indication of cancellation of positive and negative phase, as was observed with the P_t total phase shift.

Since T_t is uniform at the rotor inlet, the similarity in trends observed in Figure 6.9 suggest that similar phase is developed in each operating condition, with a few exceptions. This is sup-

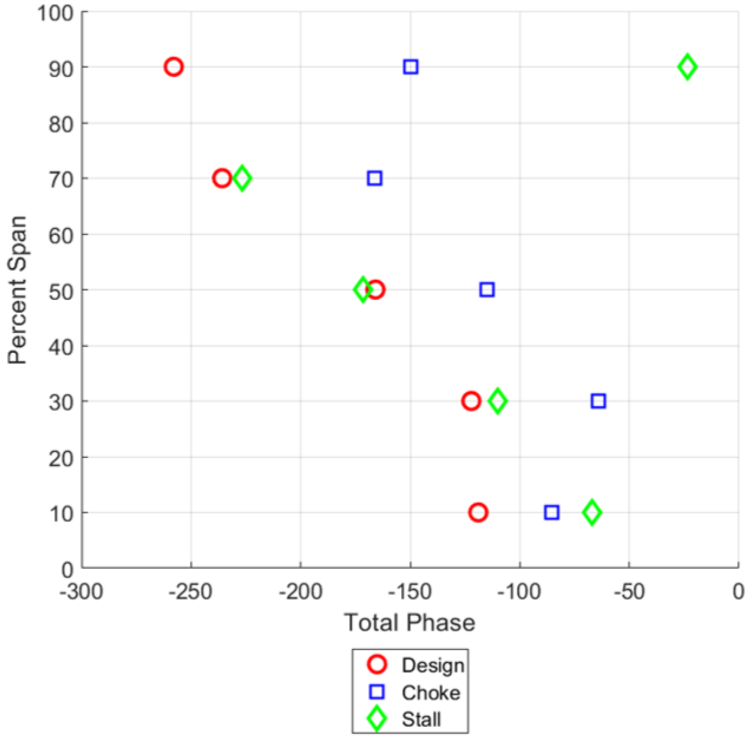

Figure 6.9: Total Fourier Phase Shift for T_t across the rotor.

ported by the traverses of T_t, where similar levels of T_t are generated in each operating condition, with a notable exception at 90% span, where near-stall differs in shape significantly.

The Total Fourier Phase Shift descriptor seems to have been more effective at capturing and representing flow characteristics for T_t than for P_t. By looking closer at the modal information provided in Figure 6.8, it is observed that for the majority of modes, the sign of the phase shift is the same and negative. This was generally the case for the P_t modal phase as well, with the exception of 70% and 90% spans. The lack of large positive sign modal phases in the T_t modal phase shifts minimized the cancellation effect which limited the total phase shift for P_t.

6.3.3 RSS Modal Phase Shift

RSS Modal Phase Shifts of T_t, as defined in Section 3.3.2, across the rotor are shown in Figure 6.10. Here, near stall and design show similar trends, increasing by 100° in phase from 10% span to 50% span. Between 30% and 50% span, choke follows a similar rate of increase in phase. Similar to what was observed with the Total Phase trends, the similarities between

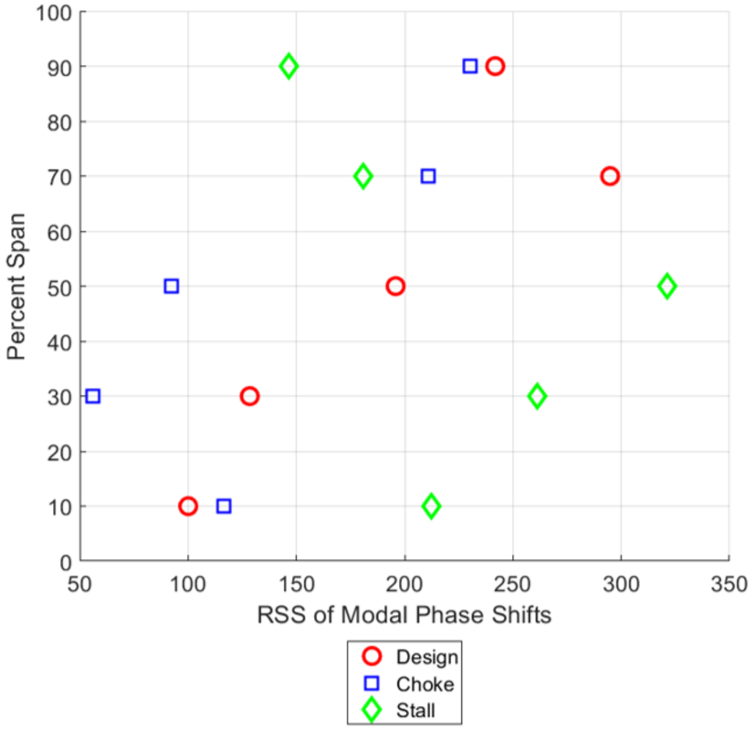

Figure 6.10: RSS Modal Phase Shift of T_t across the rotor.

the operating points mentioned suggest that the three operating conditions have similar distortion shaping between these spans. The differences in magnitude between the operating points would suggest that though the profiles have similar shaping, they have different magnitudes. Since stall consistently has the largest RSS phase value between these spans, the distortion shaping would be more pronounced while choke would have lower magnitude shaping as it has the smallest RSS values.

Stall shows the highest magnitude of phase relative to the other operating conditions until span crosses 70%, after which it has the least. The sharp decreases in T_t phase by almost 150° at high spans in near stall conditions are likely connected to the large levels of P_t RSS Phase observed in Figure 6.5 at similar spans and operating condition. Choke initially decreases in phase until the 50% span, where it begins to steadily increase. In all operating cases, RSS phase increases to the midspan, after which it tends to decrease.

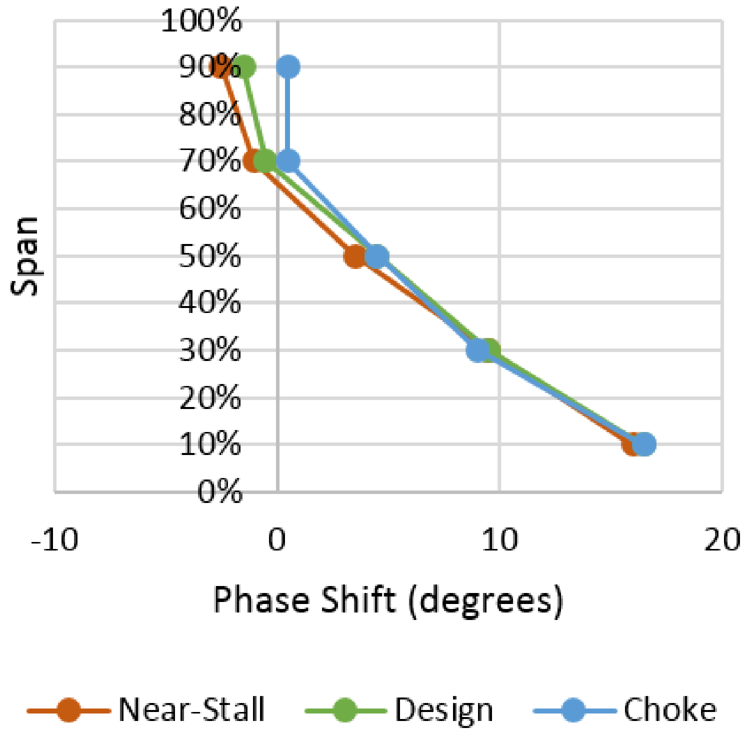

Figure 6.11: Simplified phase shift of T_t across rotor.

6.3.4 Simplified Phase Shift

The T_t simplified phase shifts across the rotor are shown in Figure 6.11. All three operating points have near identical values of phase shift from 10% through 70% span decreasing from 15° to 0°. At 90% span choke is 3° larger than near-stall. Phase shift is more positive (clockwise) near the hub (about 16°) than near the tip (about 0°). These phase shift values help quantify the shape of the T_t distortion region that is generated across the rotor, which would be a clockwise translation of distortion near the hub and no translation near the casing. They show that all three operating points shift clockwise near the hub, but do not shift significantly at the rotor tips.

Comparing Figure 6.11 to Figure 6.6 reveals the phase lag between the P_t distortion and the T_t distortion. Understanding and predicting phase lag between P_t and T_t distortion is important to fan and compressor designers. To determine phase lag the location of the P_t and T_t distortions must be identified. The design and choke operating points show that the T_t distortion lags behind the P_t distortion. The radial average of the lag is 12° for design and 15° for choke. Similar lag between T_t and P_t has been shown in other studies [15, 20]. The near-stall operating point has almost no lag because its P_t phase shifts are much different from those of design and choke. This highlights the unique distortion transfer behavior of this fan stage's operation at near-stall compared to that of design and choke. It also suggests that the lag between P_t and T_t distortion changes with operating condition.

6.4 Discussion

Several key observations were made during this study which will be further explored here. The first discussion will explore the negative phase shift observed in the simplified P_t phase shifts, as seen in Figure 6.6. An explanation for this shift will be presented. A second discussion will focus on the merits and limitations of the four phase shift description methods presented in this chapter.

6.4.1 Negative Phase Shift

The results in Figure 6.6, especially near the casing at near-stall operating conditions, are similar to the negative shift observed by Weston despite using a different inlet boundary condition and fan geometry [10]. Weston analyzed a three-stage transonic fan with a traditional 180° , 1/rev sinusoidal inlet P_t distortion profile at choke, peak efficiency, and near-stall operating conditions. Weston's definition of phase was the location of the maximum distortion and phase shift was calculated by subtracting the phase at a given axial location and the rotor inlet. The phase of the total pressure was observed to shift by -15° across the first rotor. This is illustrated in Figure 6.12, which shows traverses for total pressure at various locations in the 3-stage fan. The traverse of interest is the one located at the stator 1 inlet, labeled S1. The similarity between the results presented here and in Weston's work suggests that the negative phase shift observed at near stall is not a limited occurrence.

In an attempt to explain this phenomena, results for local power variations and P_t contours previously extracted from the simulations used to produce the phase shift results are further explored. They were originally published and analyzed as part of a separate study by Soderquist [3]. Local power traverses, included in Figure 6.13, show that for near-stall conditions in spans above 50%, the local power traverse plateaus instead of forming a distinct peak, which it does at design

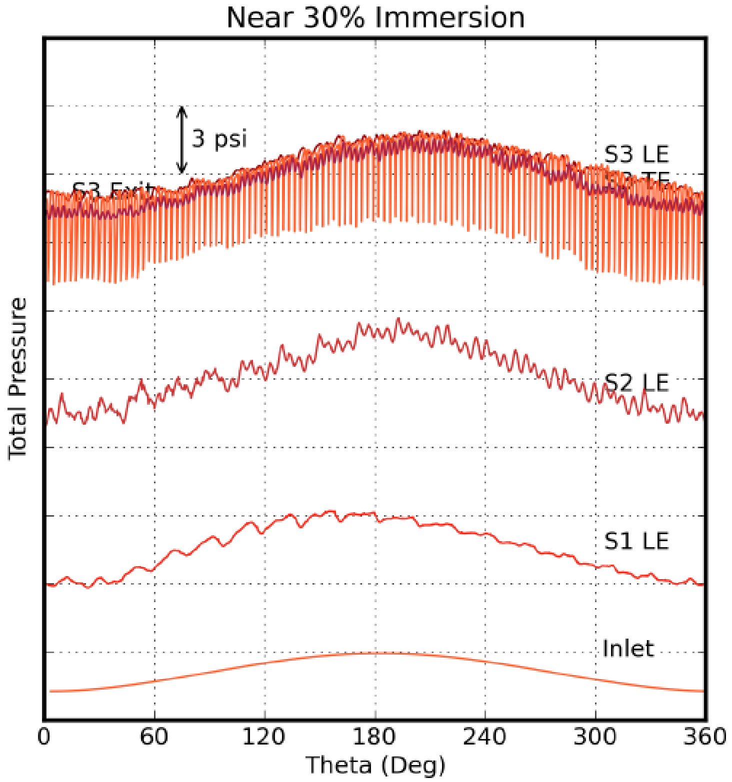

Figure 6.12: Circumferential plots of P_t at 30% span for a near stall operating point [10].

and choked conditions. This plateau spans from approximately 180° to 225° for spans above 50%. The circumferential location of this plateau corresponds with the region of counter-swirl observed at the edge of the inlet P_t distortion. This plateau represents a region where work performed by the blade was elevated and relatively constant and the resulting region of uniform high pressure is observed in Figure 6.2 at 70% and 90% span from approximately 180° to 225°. Similar plateaus are observed in the T_t traverses in Figure 6.7 in 50% and 70% spans for similar circumferential locations.

These plateaus are an indication of a localized region where the blade is unable to perform additional work on the flow, likely due to a combination of incident flow angle, mass flow, and blade geometry. Incident flow angle in this region is greatest due to the counter-swirl induced by the inlet distortion. As the fan further decreases in mass flow toward stall, this region could become a part span rotating stall cell, but further work is needed to confirm this is the case. Since blade power production is maximized at spans above 50% over a circumferential span, a uniform region of high pressure should form in this region. This is confirmed by comparing the traverses of

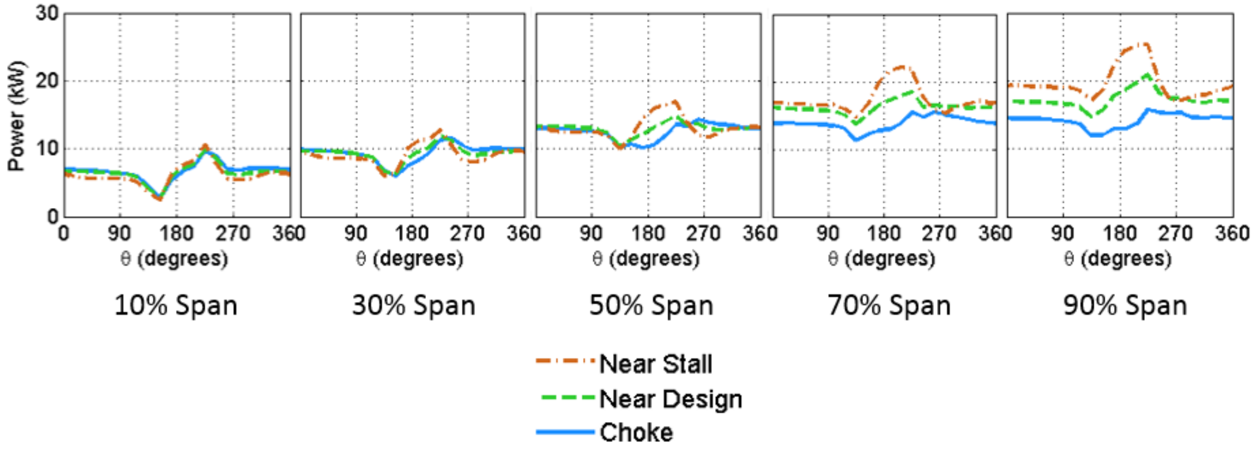

Figure 6.13: Traverses of Local Power [3].

local power with traverses of total pressure and total temperature, which are shown in Figure 6.14. Red lines are provided on the figure which show how the plateaus in local power at high spans correspond with plateaus in total pressure and total temperature at similar locations. This behavior is additionally illustrated by plotting contours of P_t at the stator inlet, which are included in Figure 6.15. The uniform region of high pressure is circled in red in the near-stall contour. These contours are normalized by the maximum P_t at the inlet plane.

In Figure 6.15, similar behavior is observed between the design and choke contours, with a region of high pressure forming at 225° and a region of reduced pressure forming at 170° which correspond with the regions of co- and counter-swirl. Both of these pressure regions occur near the hub. In the near-stall case however, an additional high pressure region is observed near the casing, which begins near 50% span and continues to the casing. This unique pressure region results in increased levels of distortion in the near-stall case, which was confirmed by Soderquist [3]. As observed by Soderquist, the largest variations in distortion were near the casing at near-stall conditions, which is where we observed that blade work is maximized.

The pressure region observed in the near-stall case in Figure 6.15 near the casing spans from approximately 170° to 230° , rather than remaining relatively concentrated, like the distortion peaks observed near the hub. This region is seen in Fig. 6.2 at 90% span, where the peak plateau starts at approximately 180° and spans to approximately 225°. Since the peak occurs at 180° , this means the distortion center as defined in Fig. 3.10 must be less than 180° , resulting in the negative phase shift observed. The larger circumferential extent of the pressure distortion at the casing in

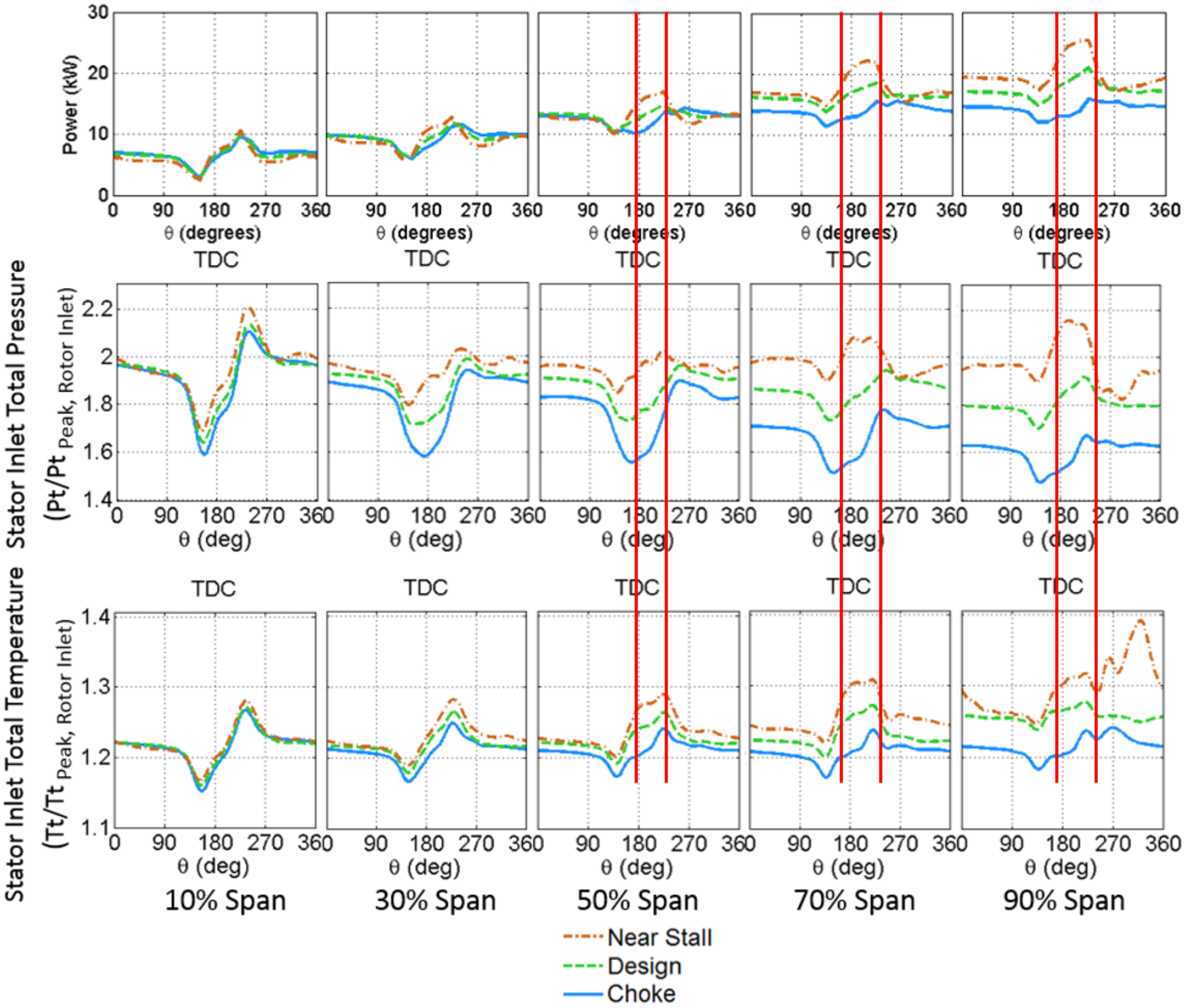

Figure 6.14: Traverses of local power, total pressure, and total temperature at the stator inlet. Red lines highlight the location of the plateau in local power and how it corresponds with similar plateaus in total pressure and total temperature.

near-stall results in the distortion center being pushed below 180° , which is reflected as a negative phase shift. This is illustrated in Figure 6.16 which shows how the plateau shifts the distortion center location (indicated by the purple lines in the figure) to a location below 180°.

The conclusion that the negative shift is due to a unique change in P_t profile at the casing is further supported by the Fourier based phase shift results. Figure 6.5 shows that the Fourier phase shift is much larger at 70% and 90% spans for stall that for choke or design. The larger value suggests that a significant shape change has occurred across the rotor at these spans, which supports the discussions regarding the high pressure region observed in the P_t contours 6.15. The high

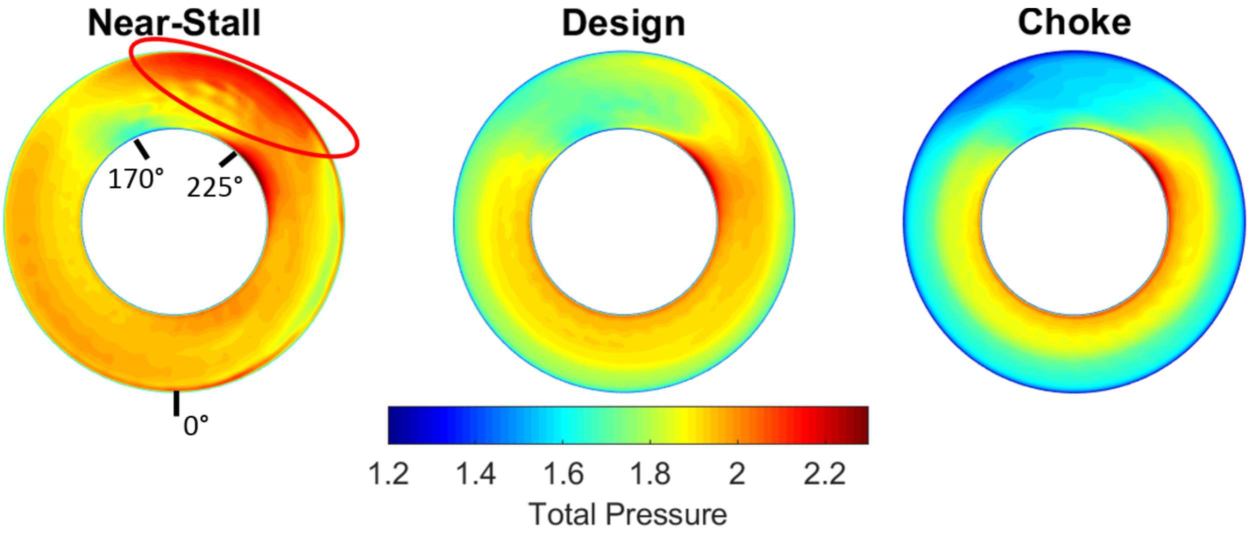

Figure 6.15: Normalized P_t contours at stator inlet with region of high pressure identified near the casing for the near-stall case.

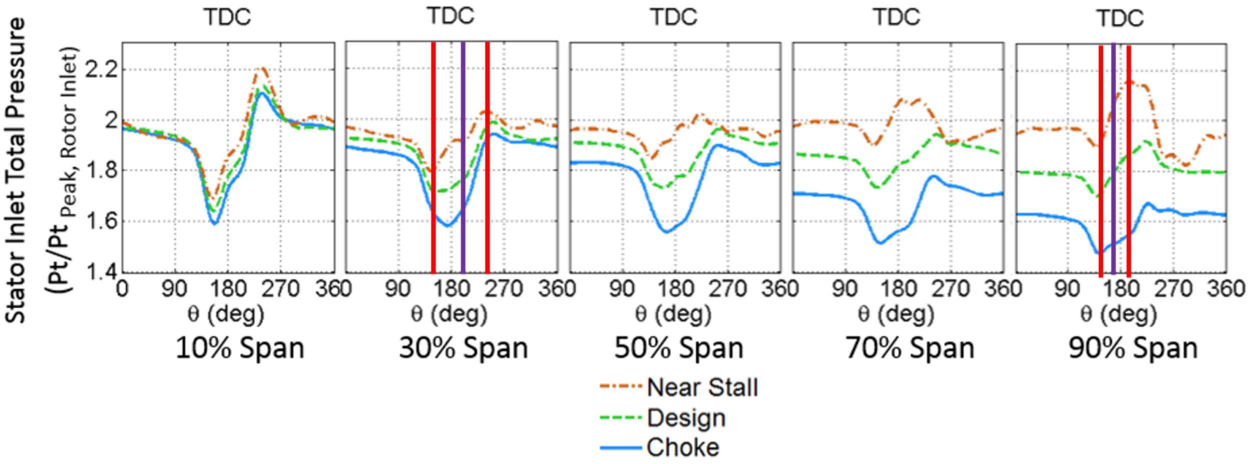

Figure 6.16: Illustration of the calculation of simplified phase in a location without a plateau and a location with a plateau. Red lines indicate the locations of maximum and minimum, the purple line represents the calculated location for the center of the distortion

pressure region observed in Figure 6.15 at the casing of the near stall operating case is manifest in the Modal Fourier Phase Shift data in Figure 6.3 as large positive phase shift values.

6.4.2 Phase Shift Descriptor Discussion

In his work introducing alternate distortion descriptors, Peterson named four key aspects that must be quantified using distortion descriptors in order to completely describe a distortion [9].

One of these was the shape of the distortion. Shape alterations through a rotor or stator must be quantified, as shape can have direct impacts on performance. Additionally, the phase shift, which quantifies rotational translation of distortion profile must also be quantified. This helps identify phase lag and predict further rotational motion of distortion.

The Fourier based descriptors outlined here, particularly the RSS Modal Phase descriptor help describe shape alterations the distortion experiences through the rotor. RSS Modal Phase is singled out due it its ability to combine modal phase shift information in a manner which does not cancel out data. Larger RSS Modal Phase shift suggests a more significant shape alteration has occurred. RSS Modal Phase does not, however, provide a clear way to quantify the circumferential location of the distortion, which is required for describing phase shift. Rather, it serves better as a good descriptor for quantifying distortion shape.

On the other hand, the simplified distortion descriptor captures translational motion of a distortion pattern, so long as the distortion shape does not drastically change. Large changes in distortion shape can cause results such as the negative phase shift observed at the casing in near-stall conditions, which may not accurately represent the phase shift of the distortion. An ideal phase shift descriptor would not be dependent on distortion shape.

Despite their individual limitations, the RSS Modal Phase and simplified phase shift parameters appear to work well in describing the shape and phase of a distortion. The RSS Modal Phase can give insight into locations where shape change may be severe enough to limit the simplified phase shift parameter. In locations where RSS Modal Phase is smaller, the simplified phase shift descriptor provides a good estimate of translational motion of distortion, without being coupled to shape changes. Used together, these descriptors could help quantify distortion shape and phase shift accurately, and in a way that offers insight into distortion transfer and generation behavior.

CHAPTER 7. CONCLUSIONS

This chapter contains the major conclusions made for each study conducted for this research. Section 7.1 contains the conclusions of the inlet variation study, which aimed to explore the impacts on distortion transfer and generation caused by small variations in the inlet distortion shape. Section 7.2 reviews the conclusions from the study into the impacts of the addition of a nozzle to a simulation geometry. This study aimed to explore if the addition of the nozzle geometry drastically impacted simulation results, compared to simulation which used a static exit boundary condition located close to the stator exit. Section 7.3 overviews the conclusions from the investigation into distortion phase shift description. The goal of this study was to compare several methods for quantifying distortion phase and investigate any trends revealed by these descriptors. Finally, future work to expand these results will be proposed.

Several key contributions to the methodology used to study inlet distortion were developed for this thesis. A new method of comparing flow fields via the comparison of similar flow fields using difference based contours, such as those shown in Figure 4.1 was developed. These contours improved the ability to clearly identify regions where flow properties are altered.

To investigate the flow physics behind changes in flow, methods for evaluating entropy in a distorted inlet simulation of Rotor 4, as presented in Section 4.4, were developed. The figures revealed important concepts about flow, such as the potential impacts of entropy redistribution, which help explain flow behavior.

Finally, the ability to describe distortion phase was improved through the creation of two new phase shift parameters, namely the Total Phase Shift and RSS Modal Phase Shift. While the Total Phase Shift parameter was shown to not be useful for describing distortion phase, the RSS Modal Phase Shift parameter helped capture information regarding the magnitude of distortion reshaping.

7.1 Inlet Distortion Variation Study Conclusions

The impact of inlet P_t distortion profiles on induced swirl, distortion transfer, power variation, and distortion generation were explored using full annulus URANS simulations of PBS rotor 4. A base 90° sector and 135° sector of P_t inlet distortion with two variations in abruptness (circumferential distance it takes to transition from clean (high) P_t to distorted (low) P_t) were simulated. Results were presented and analyzed for 10%, 30%, 50%, 70%, and 90% span.

Results showed a reduction in transition abruptness lead to a reduction in induced swirl at the edges of the distortion profile. The reductions in induced swirl caused the regions of co- and counter-swirl to drop in magnitude. This reduction in co- and counter-swirl relative to the base case yielded smaller power variations at similar circumferential locations as the flow passed through the rotor.

The maximum and minimum variations in T_t and P_t traverses decreased the inlet distortion transition gradient was less abrupt. This was a result of reductions in local power in these regions. This confirms that as inlet distortion transition becomes less abrupt, the P_t distortion transferred and the T_t distortion generated across the rotor was reduced. Trends were the same for both the 90° and 135° sectors.

There were clearly observable reductions in distortion transfer and generation through the rotor as a consequence of changing distortion sector transition abruptness. However, significant changes in overall mass flow rate, pressure ratio, and efficiency were not observed. The research is still significant as predicting distortion transfer and generation is necessary to match stages in a multistage fan or compressor.

The circumferential extent of the inlet distortion was not observed to have significant impacts on the levels of distortion transfer or generation. Induced swirl was slightly elevated for the larger 135° extent pattern, but did not result in significant difference in distortion levels at the stator inlet.

Regions of co- and counter-swirl in the induced swirl at 10% span were observed to be reduced using the variant with the least abrupt distortion transition at the inlet. This corresponded to a reduction in transferred P_t distortion and generated T_t distortion at the 10% span at the stator inlet. In addition, decreases in distortion levels were observed at all radial locations, despite these having similar levels of induced swirl.

Local power was calculated for each case, and reductions in power variations were observed at all spans as the inlet distortion transition became less abrupt. The largest reductions were observed at 10% span. Analysis of blade loading showed that a less abrupt transition increased the minimum loading and decreased the maximum loading in a blade row, thus decreasing the variation from the base. A passage shock formed in the blade row region associated with maximum power. No shocks were observed in the blade row regions of minimum and average blade loading.

At 70% span the blade loading associated with maximum power was very different than the average and minimum power loading profiles. The passage shock moved upstream and was subsequently more forward loaded. The maximum power loading was also sensitive to transition abruptness. A less abrupt transition resulted in lower pressure magnitude on both the pressure and suction surfaces.

7.2 Nozzle Study Conclusions

Total pressure ratio and efficiency were compared for a series of simulations with a nozzle to those from previous simulations conducted with a similar geometry without a nozzle. When plotted, the performance curves were very similar and close to overlapping. The performance curves for the nozzle simulation were slightly lower in pressure ratio, efficiency, and mass flow. A closer comparison of specific operating points showed that the two simulation methods differed by less than 1%. A comparison of total pressure and temperature flow fields at the rotor inlet at peak efficiency showed variations due to operating point, but did not exhibit large variation in flow field physics. Static pressure differences were explored across the stator as well, and supported the idea that using a static pressure boundary close to the stator does not have negative impacts.

These results make a compelling case for the validity of using a simplified exit boundary domain by showing that the addition of a nozzle does not drastically alter the performance of the fan stage. This means that future simulations can use the simplified boundary domain which excludes the need for a nozzle with confidence.

7.3 Phase Shift Study Conclusions

Analysis of distortion phase shift was presented and applied to simulations of a highly loaded fan stage. Phase shift is a measure of the rotational translation of a distortion profile and is valuable for understanding the translational motion of the distortion as it passes through fan and compressor blade rows. Phase shift parameters can also give insight into changes in distortion shape through a rotor. Full annulus URANS simulation results were presented for a single stage transonic fan operating at choke, design, and near stall conditions. Data was presented at 10%, 30%, 50%, 70%, and 90% span.

Several methods for quantifying phase shift were presented. Three descriptors relied on a Fourier series reconstruction of flow data, and the fourth was a simplified descriptor which leveraged the distortion shape to define phase. Each descriptor was used to define a phase shift in P_t and T_t across the rotor.

The Fourier based distortion descriptors were observed to have several limitations, especially when providing an intuitive quantitative value for rotational translation of distortion. Due to their Fourier based definition, it was determined that Fourier based descriptors, namely the RSS Modal Phase shift best describe changes in distortion shape. On the other hand, the simplified descriptor provides a more intuitive quantification of the rotational translation of distortion, as long as shape changes are not too drastic. It was suggested that RSS Modal Phase and the simplified phase shift can be used together to provide a clearer picture of radial migration of distortion.

The simplified phase shift descriptor showed that in near-stall conditions, distortion phase shift for P_t distortion ranged from 15° near the hub and -14° near the casing. Phase shift for P_t was observed to be larger and consistently positive for both the design and choked operating conditions. T_t phase shift was essentially uniform for all operating conditions, with the maximum shift at the hub, and near zero shift near the casing. Phase lag between P_t and T_t distortion was observed to change with operating condition.

The negative P_t simplified phase shift observed near the casing in near-stall was observed previously by Weston [10] in a three stage fan, suggesting the negative phase shift is not an isolated occurrence. To explain this trend, local power variations and contours of P_t were explored. It was observed that near the casing in near-stall, local power reached a maximum value, resulting in the generation of a uniform pressure region unique to the near-stall case. This region causes increases in distortion content in the near-stall case over a wide circumferential extent, relative to design and choke. The circumferential location and extent of this additional pressure distortion results in the negative phase shift observed.

7.4 Future Work

The results presented in this thesis could be expanded and explored further by pursuing the future work outlined as follows:

1. The simulations for the inlet variation study were all conducted at a near-design operating point. As seen in previous works [3], distortion transfer and generation are dependent on operating condition. Modifying the simulation to produce near-stall and near-choke results would be beneficial in further understanding the impacts that distortion transition abruptness has on levels of distortion transfer and generation.
2. The comparisons made in this thesis were made using distorted inlet cases only. In order to better understand the impacts that distortion has on rotor 4, it would be helpful to produce clean-inlet simulations using StarCCM+. Clean inlet data for rotor 4 is currently only available from experiments and as such is not suitable for close comparison with the URANS simulated data. Comparisons between clean inlet simulations and distorted inlet simulations would provide new insights which better isolate the impacts distortion has on fan performance.
3. The phase distortion descriptors explored in this work were applied to a limited set of simulations. The application of these descriptors to a wider set of simulations would provide additional insights into their utility and potentially reveal important information regarding the circumferential movements of distortion. A future study would dive deeper into how the distortion shape has changed and would seek to better define the translation of the distortion. One potential avenue for exploring such results would be the entropy contours presented in Figures 4.5 and 4.6, which effectively illustrate distortion shape after passing through the rotor. The data these contours represent could be used in some form to further describe distortion shape and translational motion.

4. The entropy investigation in Section 4.4 revealed some interesting insights into how variations in inlet distortion transition altered shock wave strength at the edges of the inlet distortion pattern. A deeper investigation into the shock behavior in these regions could provide more insights into how the changes in distortion levels observed in this thesis are caused. Ideally, a method to directly compare flow fields at these points similar to the difference contours presented in this thesis, would be produced to identify and quantify shock movements and strengths.

REFERENCES

[1] Zechmeister, C., 2011. L-1011 flight manual - project wiki Webpage. vii, 9

[2] Cousins, W., 2004. History, Philosophy, Physics, and Future Directions of Aircraft Propulsion System/Inlet Integration ASME Paper GT-2004-54210. vii, 6, 10, 18

[3] Soderquist, D. R., Orme, A. D., Gorrell, S. E., and List, M. G., 2019. "Radial Variation in Distortion Transfer and Generation in a Highly Loaded Fan Stage from Near-Stall to Choke." ASME Paper GT2019-91753. vii, ix, 3, 4, 11, 14, 15, 22, 26, 30, 35, 36, 37, 44, 48, 85, 90, 97, 99, 107

[4] Law, C. H., and Puterbaugh, S. L., 1988. Parametric Blade Study Test Report Rotor Configuration Number 4 Air Force Wright Aeronautical Labs, Nov AFWAL-TR-88-2110. vii, 11, 27, 43

[5] Cargill, P., 2011. Introduction to compressor aero design and performance PowerPoint Presentation. vii, 14

[6] Spencer, R. A., Gorrell, S. E., Jones, M. R., and Duque, E. P., 2015. "Analysis and comparison of clean vs inlet distortion flow physics at design operating condition using proper orthogonal decomposition." In *ASME Turbo Expo 2015: Turbine Technical Conference and Exposition*, no. 2015-42720, American Society of Mechanical Engineers Digital Collection. vii, 15, 16

[7] Nessler, C. A., Copenhaver, W. W., and List, M. G., 2013. "Serpentine Diffuser Performance with Emphasis on Future Introduction to a Transonic Fan." AIAA Paper 2013-0219. vii, 8, 16, 17, 29

[8] SAE, 2017. *Inlet Total-Pressure-Distortion Considerations for Gas-Turbine Engines, AIR 1420C*. The American Society of Automotive Engineers, Warrendale, PA. vii, 23, 24

[9] Peterson, M. W., Gorrell, S. E., and List, M. G., 2017. "Fourier Descriptors for Improved Analysis of Distortion Transfer and Generation." ASME Paper GT2017-65031. vii, 25, 26, 30, 31, 40, 59, 85, 101

[10] Weston, D. B., Gorrell, S. E., Marshall, M. L., and Wallis, C. V., 2015. "Analysis of Turbofan Performance Under Total Pressure Distortion at Various Operating Points." ASME Paper GT2015-42879. ix, 12, 22, 25, 59, 72, 73, 97, 98, 106

[11] Soderquist, D. R., Gorrell, S. E., and List, M. G., 2018. "Radial Variation in Distortion Transfer and Generation through a Highly Loaded Fan Stage." ASME Paper GT2018-77221. 3, 12, 14, 22, 26, 30

[12] Shaw, M., Hield, P., and Tucker, P., 2014. "The effect of inlet guide vanes on inlet flow distortion transfer and transonic fan stability." *Journal of Turbomachinery,* **136**(2). 11, 16

[13] Page, J. H., Hield, P., and Tucker, P. G., 2018. “Effect of inlet distortion features on transonic fan rotor stall.” *Journal of Turbomachinery*. 11

[14] Day, I., 2016. “Stall, surge, and 75 years of research.” *Journal of Turbomachinery,* **138**(1). 11

[15] Yao, J., Gorrell, S. E., and Wadia, A. R., 2010. “High-Fidelity Numerical Analysis of Per-Rev-Type Inlet Distortion Transfer in Multistage Fans–Part II: Entire Component Simulation and Investigation.” *Journal of Turbomachinery,* **132**(041014), pp. 1–17. 12, 22, 25, 96

[16] Gorrell, S. E., Yao, J., and Wadia, A. R., 2008. “High Fidelity URANS Analysis of Swirl Generation and Fan Response to Inlet Distortion.” AIAA Paper 2008-4985. 12

[17] Fidalgo, V. J., Hall, C. A., and Colin, Y., 2012. “A Study of Fan-Distortion Interaction Within the NASA Rotor 67 Transonic Stage.” *ASME Journal of Turbomachinery,* **134**(051011), September. 12, 22, 73

[18] Spencer, R. A., Gorrell, S. E., Jones, M., and Duque, E., 2016. “Analysis and comparison of inlet distortion flow physics at design and near stall operating condition using proper orthogonal decomposition.” In *52nd AIAA/SAE/ASEE Joint Propulsion Conference*, no. 2016-5058, p. 5058. 15

[19] Jiang, H., Lu, Y., Yuan, W., and Li, Q., 2009. “Experimental investigation of the influence of inlet distortion on the stall inception in a low speed axial compressor.” In *ASME turbo expo 2009: Power for land, sea, and air*, no. 2009-59139, American Society of Mechanical Engineers Digital Collection, pp. 1533–1542. 16

[20] Yao, J., Gorrell, S. E., and Wadia, A. R., 2010. “High-Fidelity Numerical Analysis of Per-Rev-Type Inlet Distortion Transfer in Multistage Fans–Part I: Simulations With Selected Blade Rows.” *Journal of Turbomachinery,* **132**(041014), pp. 1–10. 22, 25, 96

[21] Sheoran, Y., Bouldin, B., and Krishnan, P. M., 2012. “Compressor Performance and Operability in Swirl Distortion.” *ASME Journal of Turbomachinery,* **134**(041008), July. 22

[22] Zhang, W., and Vahdati, M., 2019. “A parametric study of the effects of inlet distortion on fan aerodynamic stability.” *Journal of Turbomachinery*. 22

[23] SAE, 2002. *Aerospace Recommended Practice, Rev. B*. The American Society of Automotive Engineers, Warrendale, PA. 23, 31

[24] Peterson, M., 2016. “Implementations of Fourier Methods in CFD to Analyze Distortion Transfer and Generation Through a Transonic Fan.” Masters Thesis, Brigham Young University. 29

[25] Sanders, D. D., and List, M. G., 2013. “CFD Performance Predictions of a Serpentine Diffuser Configuration in an Annular Cascade Facility.” AIAA Paper 2013-0220. 29

[26] Rademakers, R. P. M., Bindl, S., and Niehaus, R., 2016. “Effects of Flow Distortions as They Occur in S-Duct Inlets on the Performance and Stability of a Jet Engine.” ASME Journal of Engineering for Gas Turbines and Power, **138**(022605), February. 31

[27] Calogeras, J. E., Mehalic, C. M., and Burstadt, P. L., 1971. Experimental Investigation of the Effect of Screen-Induced-Total-Pressure Distortion on Turbojet Stall Margin Technical Memorandum NASA TM X-2239, NASA Lewis Research Center, Cleveland, OH. 31

[28] Peterson, M. W., Gorrell, S. E., List, M. G., and Custer, C., 2016. “Implementation of Fourier Methods in CFD to Analyze Distortion Transfer and Generation Through a Transonic Fan.” AIAA Paper 2016-4746. 31

[29] Vahdati, M., Sayma, A., Freeman, C., and Imregun, M., 2005. “On the use of atmospheric boundary conditions for axial-flow compressor stall simulations.”. 39

[30] Soderquist, D., 2019. “Analysis of Distortion Transfer and Generation through a Fan and a Compressor Using Full-annulus Unsteady RANS and Harmonic Balance Approaches.” Masters Thesis, Brigham Young University. 39, 41

APPENDIX A. SUPPLEMENTARY RESULTS

A.1 Additional Contours

Supplements the results found in Chapter 4. Contours of P_t, swirl, and static pressure are provided at the rotor inlet for both sectors. Contours of swirl and static pressure are provided at the stator inlet for both sectors.

To provide a clear comparison between the two variations of the inlet profile and the base profile, the contours for shape 1 and shape 2 profiles are presented as a difference from the base profile. At each location in the contour, the value shown is the result of subtracting the shape 1 or 2 profile from the base profile. In these contours, positive values indicate an increase in value relative to the base profile, while a negative value indicates a decrease relative to the base profile.

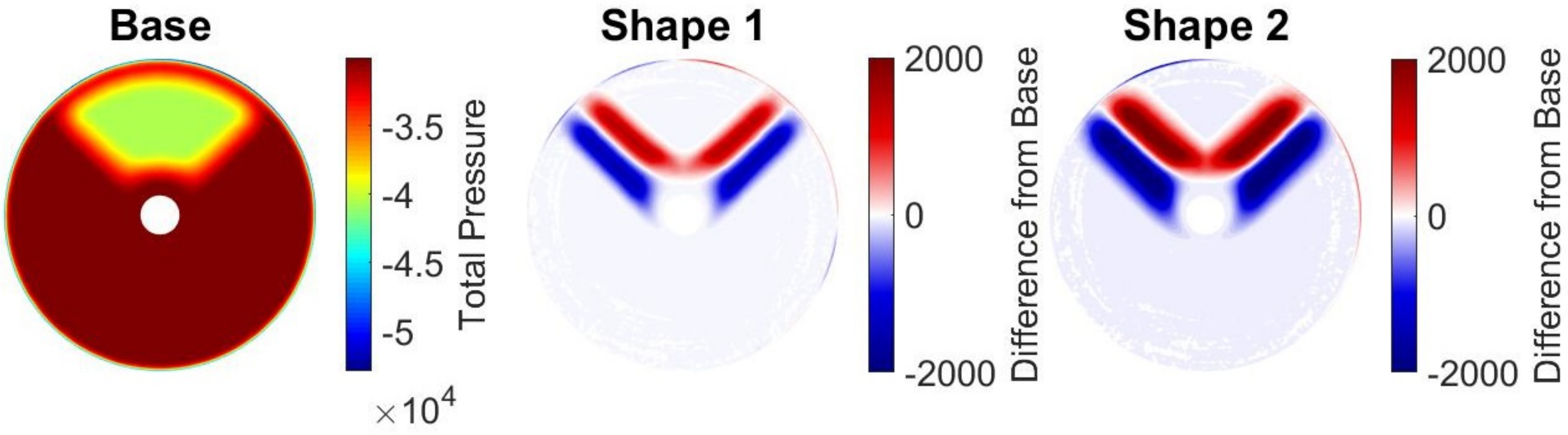

Figure A.1: P_t at the rotor inlet for the 90° sector. View is forward looking aft.

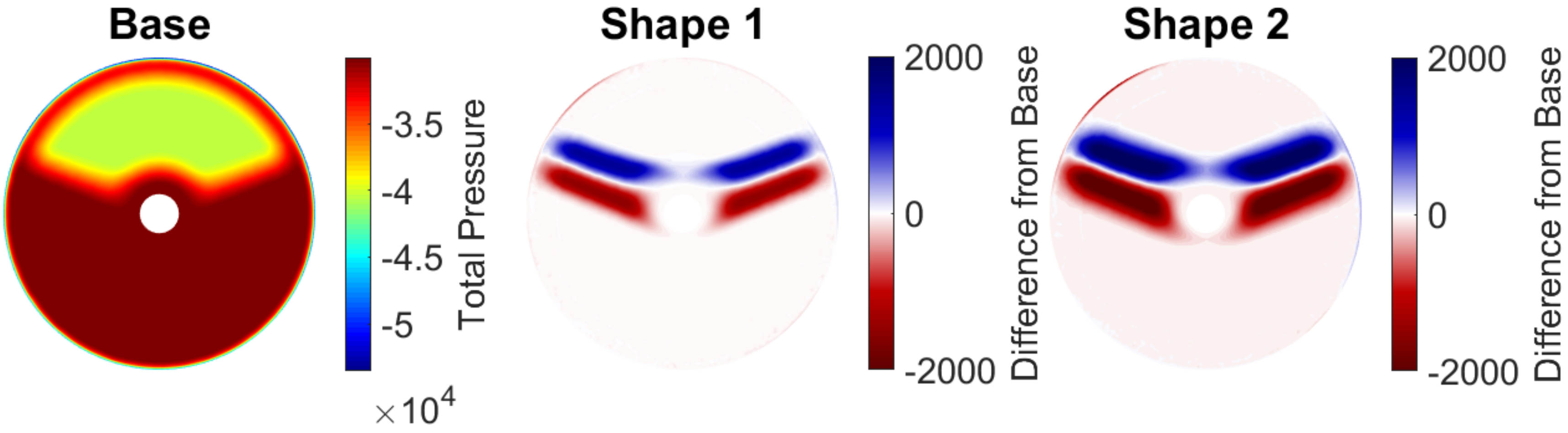

Figure A.2: P_t at the rotor inlet for the 135° sector. View is forward looking aft.

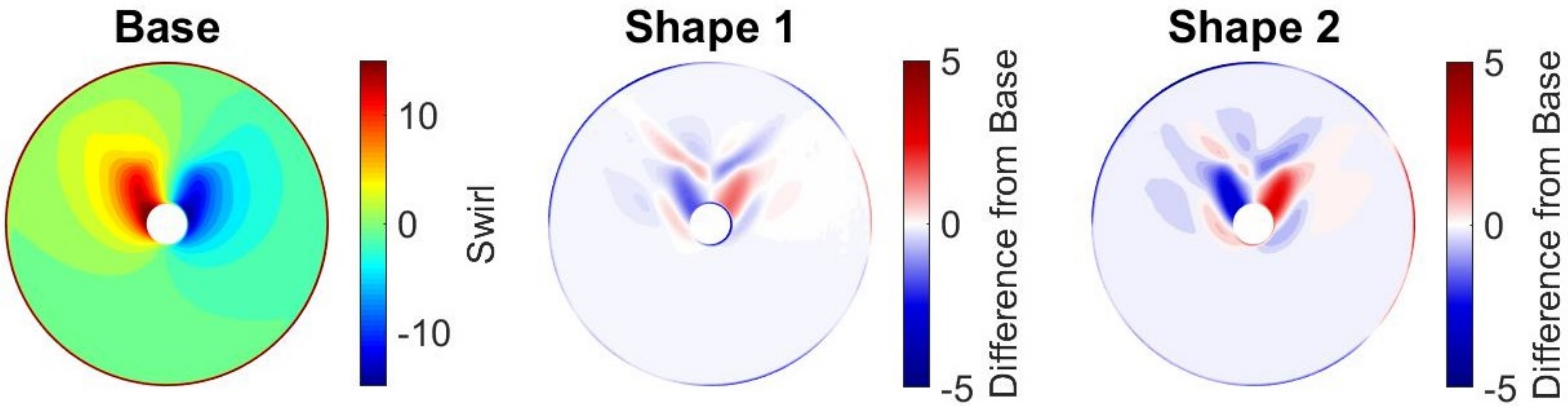

Figure A.3: Swirl at the rotor inlet for the 90° sector. View is forward looking aft.

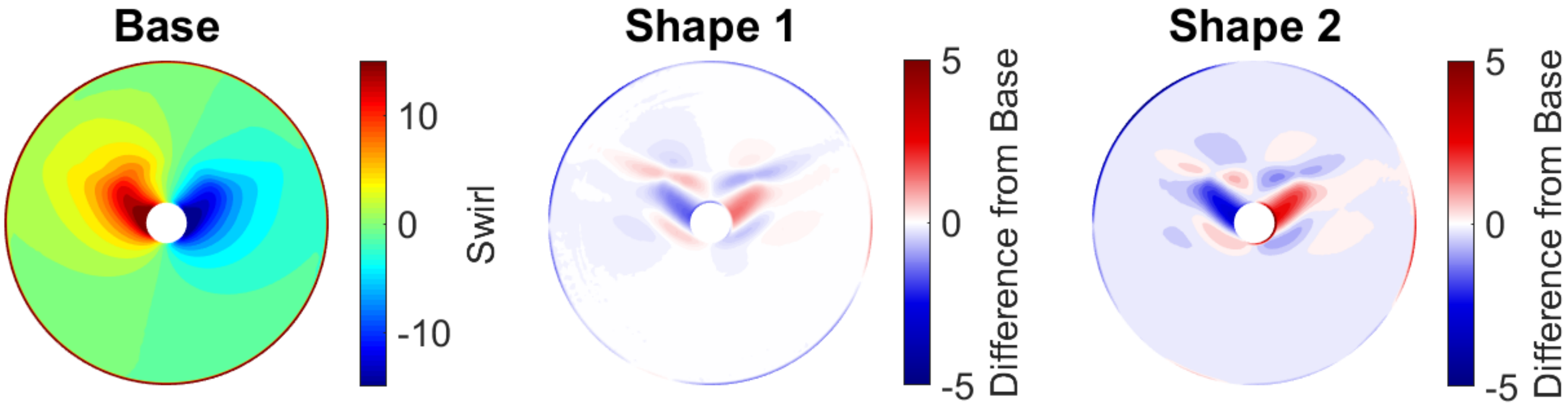

Figure A.4: Swirl at the rotor inlet for the 135° sector. View is forward looking aft.

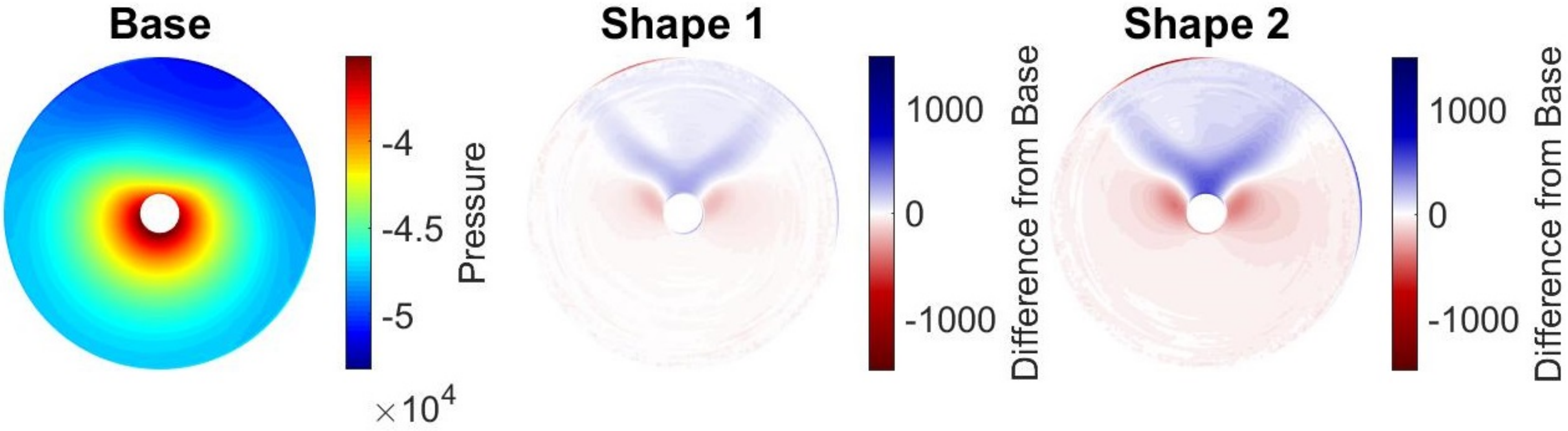

Figure A.5: Static pressure at the rotor inlet for the 90° sector. View is forward looking aft.

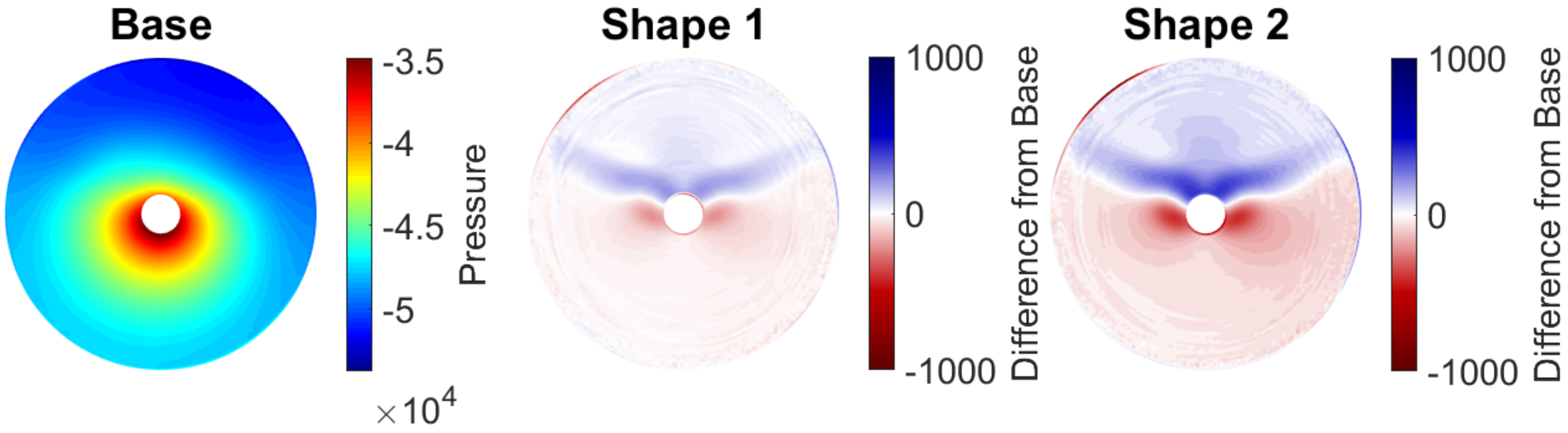

Figure A.6: Static pressure at the rotor inlet for the 135° sector. View is forward looking aft.

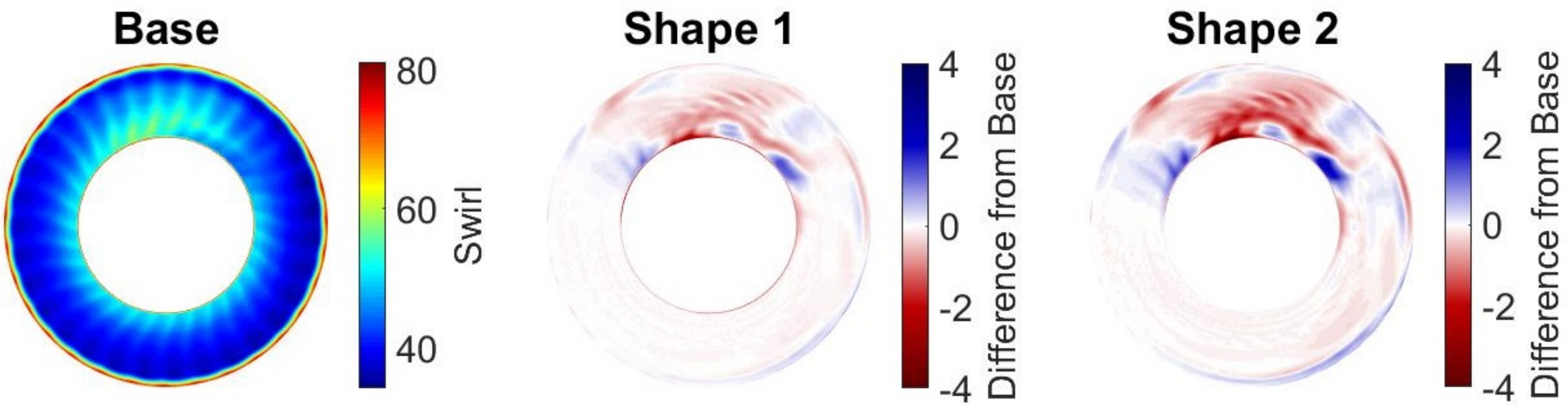

Figure A.7: Swirl at the stator inlet for the 90° sector. View is forward looking aft.

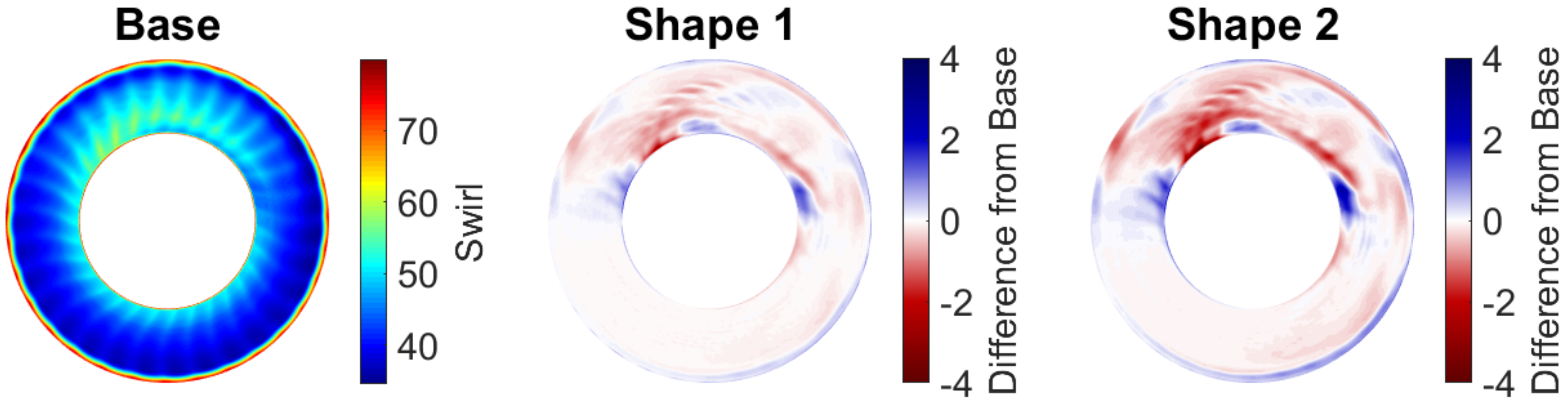

Figure A.8: Swirl at the stator inlet for the 135° sector. View is forward looking aft.

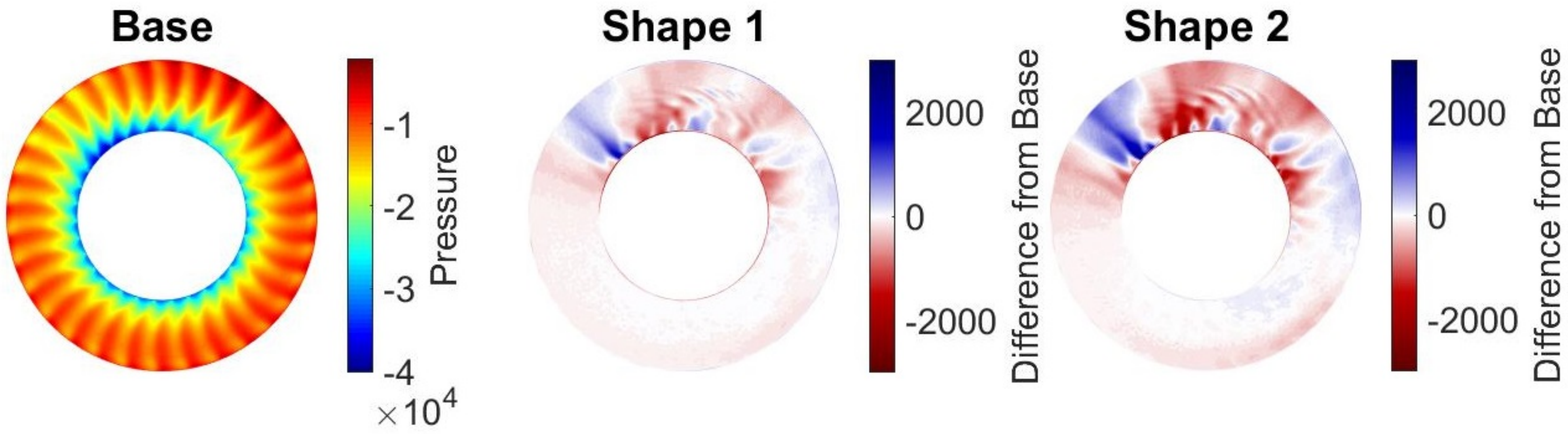

Figure A.9: Static pressure at the stator inlet for the 90° sector. View is forward looking aft.

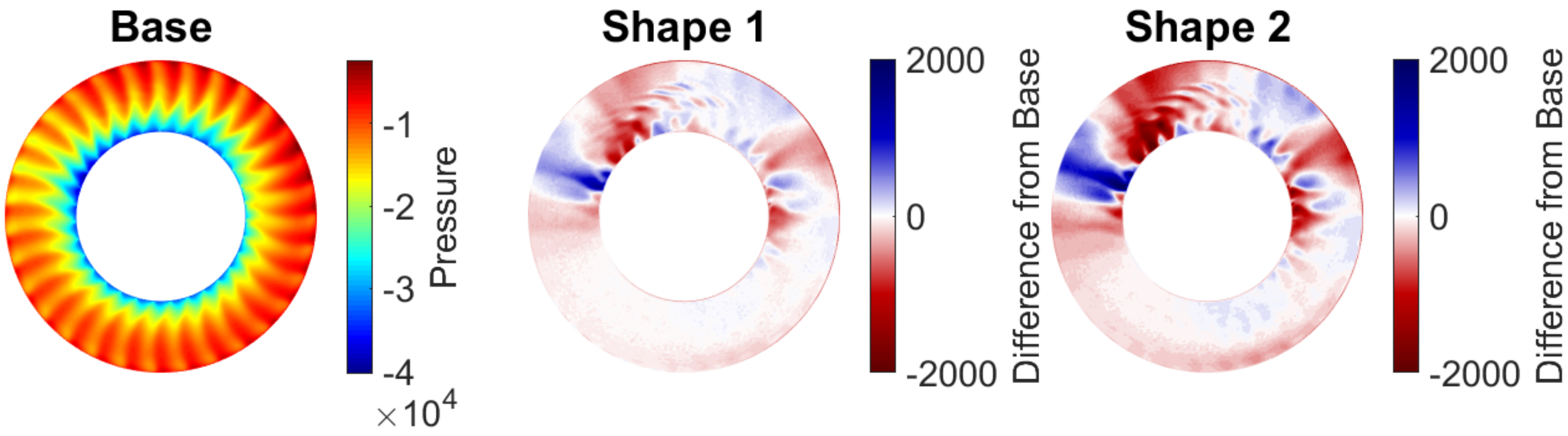

Figure A.10: Static pressure at the stator inlet for the 135° sector. View is forward looking aft.

A.2 Blade Loading Diagrams

Supplements the results found in Chapter 4. Blade loading diagrams for all spans and sectors are presented in the following figures. The maximum (red lines), minimum (blue lines), and average (green lines) blade loading are plotted for each span.

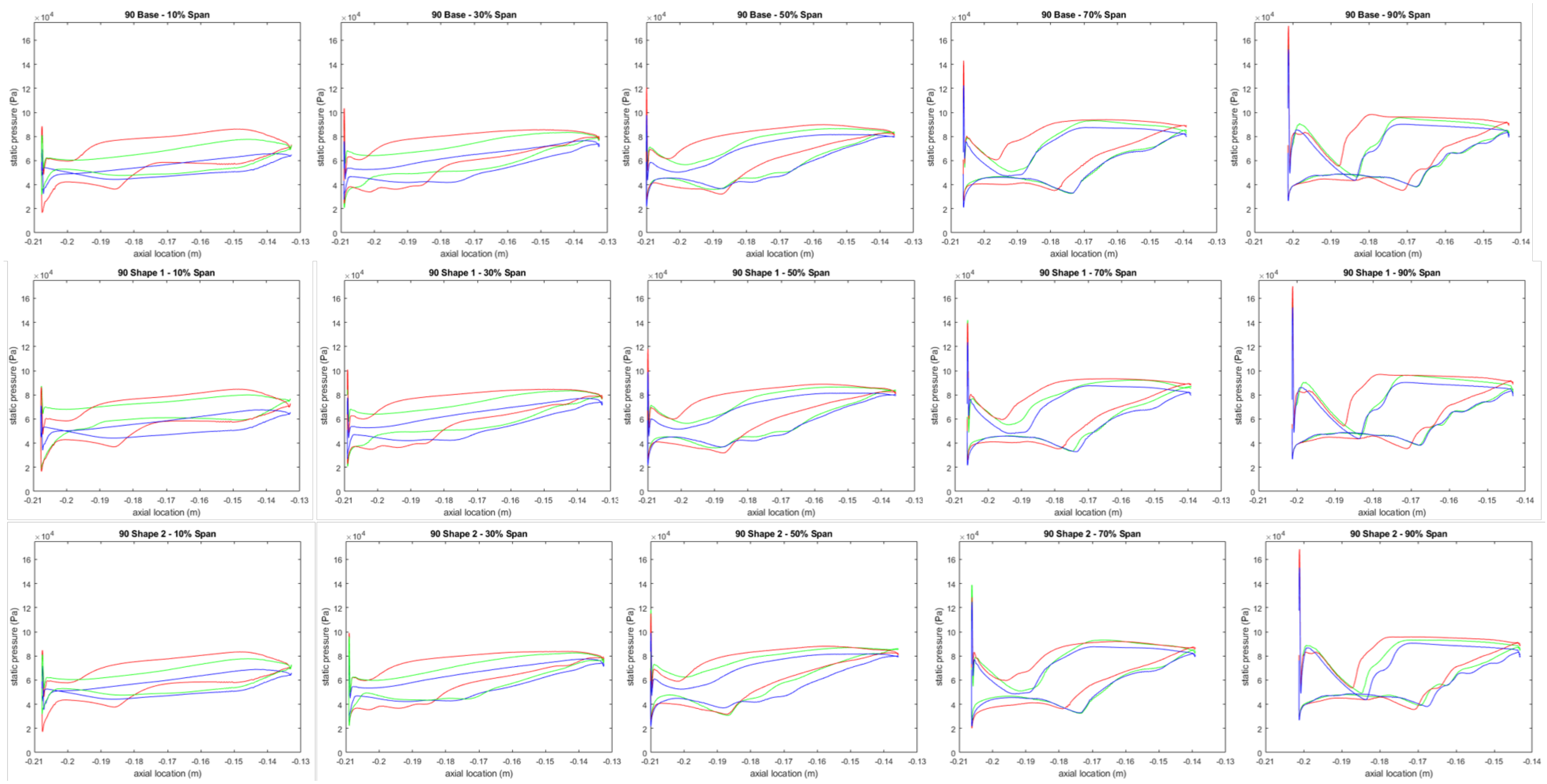

Figure A.11: Blade loading plots for 90° sector. Red lines - maximum, blue lines - minimum, green lines - average.

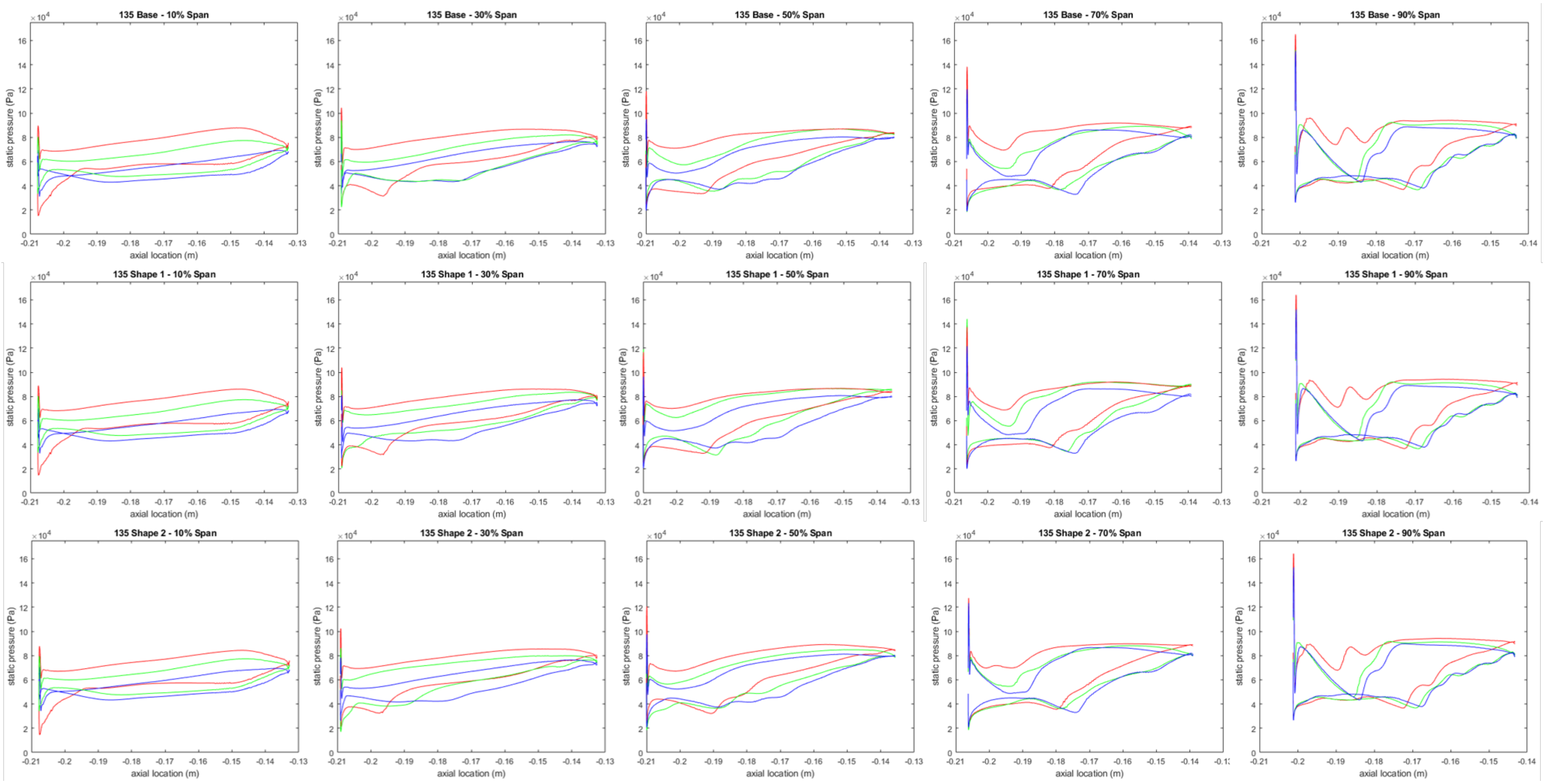

Figure A.12: Blade loading plots for 135° sector. Red lines - maximum, blue lines - minimum, green lines - average.